

UNIVERSITÉ PARIS XIII – SORBONNE PARIS NORD

École doctorale Sciences, Technologies, Santé Galilée

**A comprehensive study on structure, mechanical properties and
biodegradability of Zn-based thin films for biodegradable implants:
from binary to ternary alloys**

THÈSE DE DOCTORAT

présentée par

Cristiano POLTRONIERI

Laboratoire des Sciences des Procédés et des Matériaux

pour l'obtention du grade de

DOCTEUR EN SCIENCES DES MATERIAUX

Soutenue le 31/01/2024 devant le jury d'examen constitué de :

| | | |
|--------------------------------|--|------------------------|
| M. MARTIN Nicolas | Professeur, Université Bourgogne Franche-Comté | Rapporteur |
| M. ESTEVEZ Rafael | Professeur Université de Grenoble Alpes | Rapporteur |
| Mme BESLAND Marie-Paule | Directrice de recherche CNRS, Université de Nantes | Examinatrice |
| M. CHAUBET Frédéric | Professeur, Université Sorbonne Paris Nord | Examineur |
| M. BEST James | Docteur, Max Planck Institut Für Eisenforschung, Allemagne | Examineur |
| M. BUREAU Christophe | Docteur, alchiMedics S.A.S. | Examineur |
| M. GHIDELLI Matteo | CR-HDR, CNRS, Université Sorbonne Paris Nord | Invité |
| Mme CHALLALI Fatiha | MCF-HDR, Université Sorbonne Paris Nord | Co-directrice de thèse |
| M. DJEMIA Philippe | Professeur, Université Sorbonne Paris Nord | Directeur de thèse |

To my mentors, past and present, whose guidance and wisdom have shaped my intellectual growth and fueled my passion for science.

LIST OF PUBLICATIONS AND PARTECIPATION TO CONFERENCES

Publications in peer review journals

D.V. Sidelev, **C. Poltronieri**, M. Bestetti, M.G. Krinitcyn, V.A. Grudin, E.B. Kashkarov, "A comparative study on high-temperature air oxidation of Cr-coated E110 zirconium alloy deposited by magnetron sputtering and electroplating", Surface and Coatings Technology (2022). DOI: <https://doi.org/10.1016/j.surfcoat.2022.128134>

C. Poltronieri, A. Brognara, F. Bignoli, S. Evertz, P. Djemia, D. Faurie, F. Challali, C.H. Li, L. Belliard, G. Dehm, J.P. Best, M. Ghidelli, "Mechanical properties and thermal stability of ZrCuAl_x thin film metallic glasses: experiments and first-principles calculations", Acta Materialia (2023). DOI: <https://doi.org/10.1016/j.actamat.2023.119226>

C.H. Li, **C. Poltronieri**, G. Abadias, P. Djemia, "Computational approach to identify structural and elastic relationship in metastable crystalline and amorphous alloy thin films: Mo_{1-x}Ni_x and Mo_{1-x}Si_x case studies", accepted to Surface and Coatings Technology (2023). DOI: <https://doi.org/10.1016/j.surfcoat.2023.130168>

C. Poltronieri, F. Challali, C.H. Li, F. Tétard, V. Bockelée, F. Chaubet, P. Djemia, "Comprehensive analysis of atomic structure - mechanical properties relationships of ZnZr and ZnMg thin film alloys across the entire compositional range", submitted to Acta Materialia.

C. Poltronieri, F. Challali, C.H. Li, F. Tétard, V. Bockelée, F. Chaubet, P. Djemia, "Exploring the potential of immiscible nanocrystalline Mg-Zr films as biodegradable coatings: Structural, mechanical, and biodegradability insights", in progress, target journal: Journal of Magnesium and Alloys.

Participation to national/international conferences

C. Poltronieri, F. Challali, F. Tétard, V. Bockelée, P. Djemia, “*Mechanical Properties of Zn-Zr Thin Film Metallic Glasses*”, International conference on Advanced Materials, Mechanics and Manufacturing A3M, Sfax – Tunisia (online), March 2021, (**Oral presentation**).

C. Poltronieri, F. Challali, F. Tétard, V. Bockelée, F. Chaubet, P. Djemia, “*Mechanical properties and corrosion behavior of sputtered Zn-based thin films for vascular degradable stents*”, 13th Symposium on Biodegradable Metals, Alicante – Spain (online), August 2021 (**Oral presentation**).

C. Poltronieri, F. Challali, F. Tétard, V. Bockelée, F. Chaubet, P. Djemia, «*Propriétés mécaniques et biodégradabilité des films minces à base de Zn pour applications aux implants biodégradables*», Congrès national de la recherche des IUT CNRIUT2022, Roanne – France, June 2022 (**Oral presentation**).

C. Poltronieri, F. Challali, F. Tétard, M. Ghidelli, V. Bockelée, F. Chaubet, P. Djemia, “*Mechanical properties and biodegradability of ZnZr and ZnMg thin films for biodegradable stent applications*”, 11th European Solid Mechanics Conference ESMC2022, Galway – Ireland, July 2022 (**Oral presentation**).

C. Poltronieri, F. Challali, F. Tétard, V. Bockelée, F. Chaubet, P. Djemia, “*Structural and mechanical characterization of Zn-based binary alloys deposited by magnetron sputtering*”, Reactive Sputter Deposition RSD2022, Ghent – Belgium (online), December 2022 (**Oral presentation**).

C. Poltronieri, A. Brognara, F. Bignoli, S. Evertz, P. Djemia, D. Faurie, F. Challali, C.H. Li, L. Belliard, G. Dehm, J.P. Best, M. Ghidelli, “*Effect of composition and nanostructure on mechanical properties and thermal stability of ZrCuAl_x thin film metallic glasses*”, 1st general MecaNano meeting, Madrid, Spain, April 2023 (**Poster**).

C. Poltronieri, F. Challali, F. Tétard, V. Bockelée, F. Chaubet, P. Djemia, “*Mechanical properties and corrosion behavior of sputtered amorphous ZnMgZr thin films for biodegradable devices*”, Biometals2023, Cosenza – Italy (online), August 2023 (**Short oral presentation**).

ACKNOWLEDGEMENTS

Before we jump to discuss about science, I wish to express my sincere gratitude to the people who contributed to the progression of my academic journey. In particular:

- First and foremost, I extend my deepest appreciation to my esteemed academic advisor, Philippe, whose exceptional professional and personal mentorship has profoundly influenced the trajectory of this research and contributed significantly to my intellectual development. Equally deserving of recognition are my additional mentors, Fatiha, Matteo, James, and Gerhard, whose guidance has been pivotal to both my research and personal growth.
- Secondly, I dedicate a “thank you” also to my office-mates, Hatem and Francesco, with whom I shared all the positive (and less positive) experiences that enriched this journey. I am equally thankful for the collaboration with the "new" PhD students, Davide and Arjun, with the hope that my final weeks of my PhD were not too demotivating. I must also express appreciation to my colleagues at MPIE, particularly Andrea, Reza, Kamran, Nant, and Changwon, for their support and friendship during my stay in Düsseldorf.
- Special recognition is reserved for my friends Umberto, Luca, and Jacopo, as well as my family, whose encouragement, understanding, and patience provided essential sustenance during the demanding phases of this academic pursuit.
- In conclusion, I extend my gratitude to the numerous participants and volunteers whose names may not find mention here but who generously contributed their time and expertise to this academic endeavor. Your collective support has been indispensable.

I offer my sincere thanks to each of you.

TABLE OF CONTENTS

| | |
|--|----|
| Introduction | 1 |
| 1 Chapter 1: State-of-the-art..... | 7 |
| 1.1 The need of biodegradable implants | 7 |
| 1.1.1 Permanent biomaterials | 9 |
| 1.1.2 Biodegradable biomaterials..... | 13 |
| 1.2 Nanocrystalline materials | 17 |
| 1.3 Metallic glasses | 21 |
| 1.4 Biomedical TFMGs and research challenges..... | 29 |
| 1.5 References..... | 32 |
| 2 Chapter 2: Materials and Methods | 44 |
| 2.1 GFA evaluation and first-principles calculations..... | 44 |
| 2.1.1 Thermodynamic evaluation of GFA | 44 |
| 2.1.2 Special quasi-random structures for single crystalline random alloys | 48 |
| 2.1.3 Ab initio molecular dynamics to design amorphous materials | 49 |
| 2.2 Thin films elaboration by magnetron sputtering | 52 |
| 2.3 Structural characterization (SEM/EDX and XRD) | 56 |
| 2.4 Mechanical characterization..... | 57 |
| 2.4.1 Nanoindentation | 57 |
| 2.4.2 Brillouin light scattering..... | 59 |
| 2.4.3 Tensile test on Kapton® substrate | 60 |
| 2.5 Static immersion test | 61 |

| | | |
|-------|--|-----|
| 2.6 | References..... | 62 |
| 3 | Chapter 3: Nanocrystalline and amorphous binary alloys..... | 65 |
| 3.1 | Nanocrystalline MgZr..... | 67 |
| 3.1.1 | Deposition process | 67 |
| 3.1.2 | Structure | 68 |
| 3.1.3 | Mechanical properties | 73 |
| 3.1.4 | Degradation in SBF..... | 76 |
| 3.1.5 | Summary and conclusions | 78 |
| 3.2 | Zn-based binary alloys: ZnMg and ZnZr..... | 79 |
| 3.2.1 | Thin film synthesis and composition tailoring..... | 79 |
| 3.2.2 | Glass-forming ability and average interatomic distance..... | 80 |
| 3.2.3 | Hardness, yield strength and mismatch entropy | 88 |
| 3.2.4 | Elastic moduli | 90 |
| 3.2.5 | Voronoi tessellation and clusters analysis..... | 96 |
| 3.2.6 | Tensile tests on Kapton® | 97 |
| 3.3 | Discussion..... | 101 |
| 3.3.1 | Glass forming ability, atomic distances and bonds fractions | 101 |
| 3.3.2 | Mechanical properties: hardness, yield strength and elastic strain | 107 |
| 3.3.3 | Elastic moduli | 109 |
| 3.3.4 | Static immersion test of ZnMg and ZnZr alloys | 112 |
| 3.3.5 | Summary and conclusion..... | 115 |
| 3.4 | References..... | 117 |
| 4 | Chapter 4: From binary to ternary ZnMgZr alloys..... | 123 |
| 4.1 | Glass-forming ability and deposition | 123 |
| 4.2 | Amorphous structure | 125 |

| | | |
|-----|--|-----|
| 4.3 | Mechanical properties | 127 |
| 4.4 | Tensile test on Kapton® | 129 |
| 4.5 | Biodegradability ternary ZnMgZr thin film alloys | 130 |
| 4.6 | Corrosion investigation..... | 131 |
| 4.7 | Cytotoxicity and viability study | 134 |
| 4.8 | Conclusions | 135 |
| 4.9 | References..... | 137 |
| 5 | Conclusions and perspectives | 139 |
| 6 | Annex | 147 |

LIST OF ACRONYMS/ABBREVIATIONS

| | |
|------------|------------------------------------|
| ν | Poisson's Ratio |
| σ_y | Yield Strength |
| AIMD | Ab Initio Molecular Dynamics |
| BLS | Brillouin Light Scattering |
| BMG | Bulk Metallic Glasses |
| d_{av} | Average interatomic distances |
| E | Young's Modulus |
| EDX | Energy Dispersive X-Ray |
| G | Shear Modulus |
| GFA | Glass Forming Ability |
| H | Hardness |
| LRO | Long Range Order |
| MD | Molecular Dynamics |
| MG | Metallic Glass |
| MRO | Medium Range Order |
| PDF | Pair Distribution Function |
| PDP | Principal Diffraction Peak |
| PLA | Polylactic acid |
| PPDF | Partial Pair Distribution Function |
| PVD | Physical Vapor Deposition |
| R_c | Critical Cooling Rate |
| SBF | Simulated Body Fluid Solution |
| SEM | Scanning Electron Microscopy |
| SQS | Special Quasi-random Structure |
| SRO | Short Range Order |
| TFMG | Thin Film Metallic Glasses |
| XRD | X-Ray Diffraction |

INTRODUCTION

Over the past five decades, the field of biomedicine has undergone significant evolution, leading to the development of glasses, metals, and polymers, along with composite biomaterials and advancing in the frontier of medical device technology. Traditionally, the majority of these biomaterials were designed to provide permanent support for damaged bodily apparatus, becoming indispensable devices in modern society, serving various critical applications. These applications span from essential life-saving devices like cardiac pacemakers and orthopedic implants to innovative solutions like neural stimulators and cochlear implants. The success and reliability of these devices can be attributed to the meticulous selection and utilization of biomaterials: the first and most important step for tailoring their performance, biocompatibility, and long-term durability. The development and application of biomaterials represent a dynamic and continuously evolving discipline marked by the ongoing challenge to create materials capable of withstanding the demanding physiological environments, mechanical stresses and biocompatibility requirements. However, while permanent devices have undoubtedly revolutionized the field of medical device technology, they possess some limitations. One significant drawback lies in the potential for long-term complications, like wear, corrosion, and mechanical failures, which necessitate costly and invasive revision surgeries. Additionally, any extraneous material in the body can provoke immune responses or increase the risk of inflammations and infections, leading to discomfort and health issues for patients. Furthermore, the permanence of these devices can also need long-term medical treatments, making it challenging to adapt to the specific patient needs. Hence, it is crucial to recognize that the application of permanent biomedical devices necessitates a balanced consideration of their drawbacks and alternative solutions, such as biodegradable devices, to address these limitations effectively. For the aforementioned reasons, the development of

biodegradable implants, designed to serve temporary medical purposes before naturally dissolving within the body, represent a groundbreaking transition in the field of medical device technology and have garnered significant attention from researchers, clinicians, and healthcare industries. However, the successful implementation of biodegradable implants is not without their own set of challenges. The development of biomaterials that possess the required mechanical properties and tailored degradation rate based on the specific application presents a multifaceted challenge. The balance between structural integrity, subjected to a homogenous degradation and the predictable degradation kinetics must be meticulously tailored to align with the intended clinical purpose of the implant. Furthermore, ensuring the biocompatibility of these materials and their degradation byproducts, as well as understanding their interactions within the intricate physiological environment, requires rigorous scientific investigations.

The utilization of metallic glasses (MGs) may present a promising avenue in the domain of biomedicine because of the unique physical properties attributed to their disordered structure, making them valuable candidates for the development of novel biodegradable implants. In particular, MGs offer tailored mechanical properties as function of the chemical composition and structure, reaching extraordinary values of elastic limit ($\sim 2\%$) and yield strength (~ 2 GPa) close to the theoretical limit. This flexibility in mechanical properties is critical for designing implants capable of withstanding the specific mechanical requirements for various applications. In addition, unlike conventional crystalline metals, the absence of second phases, grain boundaries or segregations and the isotropic structure of MGs lead to a more uniform and predictable degradation process, minimizing the risk of generating macroscopic debris. Selecting the appropriate MG composition is crucial and challenging, as it necessitates a careful balance between, mechanical strength, degradation kinetics, and biocompatibility for mitigating inflammation and potential complications following implantation, each of which may vary according to specific clinical requirements. For example in orthopedics, MGs could find application as biodegradable bone fixation devices, providing temporary support during the healing process and gradually

dissolving as the bone regenerates, at the same time MGs could also be used in cardiology as biodegradable stents, offering temporary vascular support and reducing the risk of restenosis.

However, bulk metallic glasses (BMGs) are known for exhibiting a macroscopically brittle behavior at room temperature due to their intrinsic lack of defects, such as dislocations, which could otherwise facilitate plastic deformation. Moreover, size effects in MGs showed a role on the mechanical behavior at the sub-micrometer scale, inhibiting the shear band propagation and leading to larger plastic deformation and toughness in the case of thin film metallic glasses (TFMGs). Furthermore, the manufacturability of MGs implants with intricate shapes and features can be complex and developing scalable manufacturing processes for these materials is a critical consideration. The fabrication techniques of TFMGs, like physical vapor deposition (PVD), is a scalable industrial process and enable several advantages as the precise control over the chemical composition, thickness and its uniformity, offering a wide flexibility in terms of customizable film properties to meet specific application requirements. In addition, PVD techniques are used to deposit thin films onto ceramic, metal or even polymeric substrates with larger cooling rates compared to BMGs fabrication methods, increasing the glass forming ability of the films.

In this context, this PhD thesis aims to shed light on the potential of Zn-based TFMGs as coating for biodegradable implants. The films were synthesized by RF-magnetron co-sputtering and then, a delicate campaign of experiments and calculations was carried out to investigate the structural and mechanical properties of the films. Furthermore, the corrosion and degradation behavior were as well investigated as the biocompatibility through cytotoxicity tests. Among the involved characterization techniques, X-ray diffraction (XRD) and scanning electron microscopy (SEM) were used to investigate the structure of the deposited films. The mechanical properties of the materials were investigated through non-conventional Brillouin light scattering technique, nanoindentation and tensile tests on Kapton®. The film behavior in physiological environment was assessed by electrochemical and static immersion tests in simulated body fluid solution at 37 °C. In addition, *ab initio* molecular dynamic

calculations were used to simulate the structure of the materials and density functional theory was used to investigate the elastic properties of the materials in collaboration with State Key Laboratory of Superlattices and Microstructures in Beijing. The electrochemical investigations have been carried out in collaboration with Laboratory for Biomaterials and Bioengineering in Quebec, while the cytotoxicity was assessed in collaboration with the Laboratory of Vascular Transitional Science (LVTS) in Paris.

Within this experimental and calculation campaign lasted three years at LSPM (November 2020 – October 2023), a parallel research has been carried out during an overall period of 6 months at Max-Planck-Institut für Eisenforschung (MPIE) in Düsseldorf (DE) in the framework of several international projects. Specifically, in 2021 and 2022 an overall period of 2 months in the framework of Partenariats Hubert Curien (PHC) Procope project “New-Glasses” (P.I.s: Dr. M. Ghidelli, Dr. J. P. Best) was dedicated to investigation of the effect of composition and nano-architecture (multilayers) on mechanical properties and thermal stability of $ZrCuAl_x$ TFMGs. A dedicated synchrotron run has also been carried out in DESY (Hamburg, DE) to investigate the structural evolution of $ZrCuAl$ TFMGs during devitrification. These experiences lead to a first publication and to the possibility to carry out a further research at MPIE for an overall period of 4 months in the framework of SALTO project investigating the effect of devitrification on $ZnMgZr$ TFMGs on the structural and mechanical response. Furthermore, a synchrotron beam time at SOLEIL (Saclay, FR) on Diffabs line (Dominique Thiaudière) in Nov. 2023 was employed to investigate in detail (by XRD and EXAFS) the devitrification phenomena occurring in $ZnZr$ TFMGs as preliminary study before exploring ternary $ZnMgZr$ TFMGs.

In the light of these clarifications, the following manuscript is organized in the following four chapters:

Chapter 1 – State-of-the-art provides a literature review of Zn, Mg and Zr-containing TFMGs, including the concept of amorphous material and its peculiar physical properties, its glass-forming ability followed by a focus on the mail literature about the

specific application of TFMGs for biodegradable implants. This chapter will provide the essential elements for the discussion and comprehensive understanding of the results presented in the other chapters, highlighting their novelty with respect to the existing literature studies.

Chapter 2 – Materials and methods describes the experimental techniques and calculation methods involved in the synthesis, characterization and simulation of the material of interest. The fundamental experimental facilities used to fabricate and investigate the chemical, structural and physical properties of the studied sample will be recalled. The calculation methods used to mimic the disordered atomic structure of metallic glasses will be introduced, discussing density functional theory and *ab initio* molecular dynamics approaches.

Chapter 3 – Nanocrystalline and amorphous binary alloys illustrates in the first part, the experimental and simulation results concerning nanocrystalline MgZr then, in the second part, the results and discussion of structural and mechanical properties of binary ZnMg and ZnZr films with particular emphasis to the relationships between structure-mechanical properties of amorphous compositions.

Chapter 4 – From binary to ZnMgZr ternary alloys, based on the knowledge acquired in Chapter 3 on binary alloys, this chapter gives a comprehensive understanding of the development and of ZnMgZr TFMGs and the related physical properties, exploring the entire range of compositions. A dedicated study on biodegradability, biocompatibility and corrosion behavior of these alloys will be addressed.

Conclusions and perspectives summarizes the key results and findings of this work. The perspectives include the mechanical investigation of advanced nano-architected films such as fully-amorphous multilayer and thermal-annealed nanocomposites to enhance the limited plasticity of TFMGs.

CHAPTER 1: STATE-OF-THE-ART

In recent years, significant focus has been directed towards Mg-, Zn- and Fe-based biomedical devices capable of dissolving within the human body, avoiding the complications related to a second surgery, in contrast to the traditional permanent Ta- and Ti-based, Co-Cr or stainless steel devices [1-3]. The choice of Mg, Zn and Fe derive from the active role of their ions in regular cellular metabolism, making them non-toxic and biocompatible [4-6]. Among these promising biomaterials, Mg is widely investigated for biodegradable orthopedic applications due to its low elastic modulus, which closely resembles that of cortical bone, thus preventing stress shield phenomena [1]. However, it is recognized for its susceptibility to high corrosion rates and hydrogen evolution within the human body. To mitigate the drawbacks of Mg-based alloys, some strategies include alloying with other elements, such as Zn and Ca, and the development of single-crystal, poly(nano)crystalline and metallic glassy materials [7].

This chapter offers an overview of the biomaterials currently employed in both permanent and temporary devices, providing valuable insights into their advantages and drawbacks. Simultaneously, it presents the strategies for developing novel biomaterials and explores promising perspectives for future research. This state-of-the-art discussion serves as the foundational knowledge for a comprehensive understanding of the rationale behind our alloy selection (Zn-Mg-Zr), the associated results and the scientific discussion.

1.1 The need of biodegradable implants

The field of biomaterials science incorporates a multidisciplinary approach involving materials science, biology, chemistry, and engineering. The analysis of the physical,

chemical, and mechanical properties of biomaterials is crucial for understanding their behavior within the biological environment. Properties such as biocompatibility, strength, flexibility, and surface characteristics are meticulously examined to ensure that the biomaterials function effectively without triggering immune responses or toxic effects. Moreover, the various biomaterials may delve into the diverse applications in the medical fields, including orthopedics, cardiology, dentistry, and tissue. This various ranges of applications often require biomaterials with tailored physical and chemical properties to efficiently suit the specific medical needs. For example, for orthopedic implants, e.g., screws, bone plates, and prosthesis, the biomaterial must be osseointegrated to avoid the stress shielding caused by the difference in Young's moduli between the implant device and the cortical bone (~10-30 GPa) [8]. The desirable requirements of biodegradable orthopedic implants are given in **Table 1.1** [7].

Table 1.1 Desirable mechanical requirements for orthopedic biodegradable implants [7].

| <i>Property</i> | <i>Value</i> |
|---------------------------|--|
| Density | 1.8-2 g/cm ³ |
| Ultimate tensile strength | ≥ 300 MPa |
| Tensile yield strength | ≥ 200 MPa |
| Young's modulus | 17-22 GPa |
| Compressive strength | ≥ 230 MPa |
| Compressive yield stress | ≥ 182 MPa |
| Elongation | ≥ 10% |
| Fracture toughness | ≥ 12 MPa m ^{1/2} |
| Mechanical integrity | ≥ 24 weeks based on longest healing time of neck femur. Fixation screw must maintain 95% of original load-bearing capability for at least 6 weeks after implantation |

Moreover, these requirements could be different depending on the part to be replaced. Nevertheless, in the case of other biomedical devices such as cardiovascular stents, the requirements are different and they are listed in **Table 1.2** [9].

Table 1.2 Criteria for biodegradable vascular stents [9].

| <i>Property</i> | <i>Value</i> |
|--|---------------------|
| Yield strength | ≥ 200 MPa |
| Ultimate tensile strength | ≥ 300 MPa |
| Elongation | $\geq 15-18\%$ |
| Ratio of yield strength to elastic modulus | $\geq 0.16\%$ |
| Elastic recoil on expansion | $\leq 4\%$ |
| Degradation period (full-absorption) | 12-24 months |
| Degradation rate (penetration rate) | ≤ 0.02 mm/year |

All of these mechanical requirements must be satisfied to insure the radial strength, recoil and deliverability of the device [9]. To satisfy these requirements, nowadays, the majority of permanent biomedical implants are made of corrosion-resistant metals such as Ta, Ti, Co-Cr alloys and stainless steel [10, 11] because of their superior mechanical properties compared to polymers and ceramics [12].

1.1.1 Permanent biomaterials

Among the traditional permanent biomaterials, Ta represents a prominent biometal used in medical implants because of its exceptional chemical stability, biological inert and anti-corrosion properties [13], making it well-suited for various applications. Historically, Ta was utilized for surgical sutures [14] due to its strength (138 MPa), ductility and not irritating behavior [15]. Successively, the long-term benefits and advantageous properties of Ta extended its application in more complex scenarios, including mesh for hernia surgery, foil for peripheral nerve reconstruction, and tubes for frontal sinus reconstruction, remarking its large biocompatibility and flexibility [11, 16]. However, despite these advantages, the significant manufacturing costs, high Young's modulus (186 GPa) and density (16.6 g/cm³) of Ta make it incompatible with

bone tissues and for load-bearing applications posing further challenges and limiting its widespread use [11]. To address these limitations, ongoing research efforts are exploring solutions to decrease the elastic modulus of Ta. One solution is the elaboration of porous Ta with open cellular structure and trabecular geometry, which has revolutionized the orthopedic field thanks to its capacity to closely mimic osseous tissue and facilitating significant bone ingrowth through the presence of interconnecting pores [17]. For instance, mechanical testing on 3D manufactured porous Ta alloy with fully interconnected open pores (illustrated in **Fig. 1.1**) was developed to allow bone ingrowth while maintaining a ductile deformation mechanism [18]. Furthermore, it has shown Young's modulus and yield strength values ($E = 1.22$ GPa, $\sigma_y = 12.7$ MPa) close to those of human cancellous bone [19].

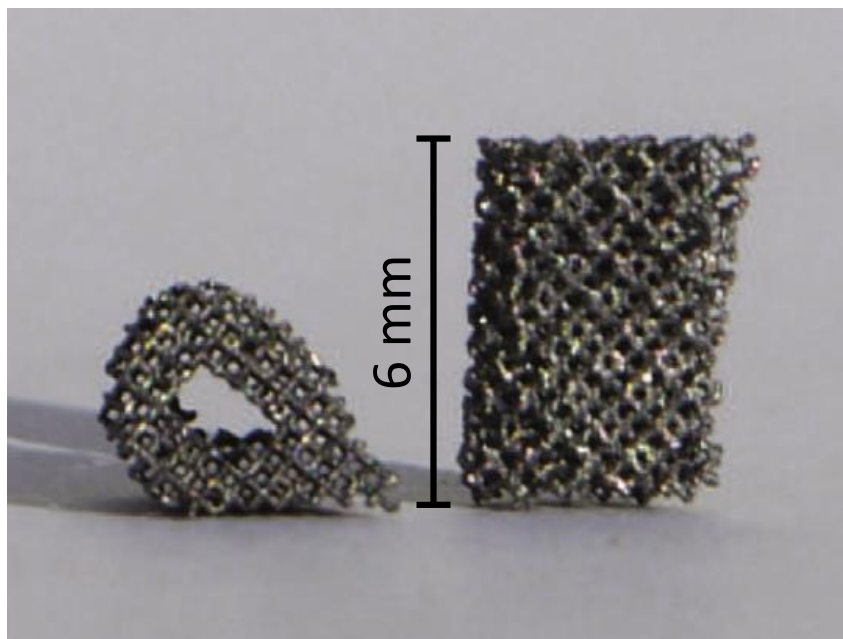


Fig. 1.1 Top and side view of the shaped porous Ta implant [18].

Another biomaterial currently employed in permanent devices is pure Ti and its alloys, which are widely used for orthopedic and dental implants due to their exceptional tensile strength, corrosion resistance, high specific strength, rigidity, fracture toughness and biocompatibility, rendering them ideal for various medical implant applications [20]. Another advantage of Ti and its alloys for orthopedic purposes is that the Young's modulus of Ti (about 102 GPa [21]) is closer to the one of human bone

when compared to other biomaterials such as stainless-steel (about 210 GPa [22]) and Co-Cr alloys (about 240 GPa [22]). However, the susceptibility of pure Ti to abrasive and adhesive wear limits its use in implantable devices, where the wear debris between implant surfaces negatively affects the long-term stability of the implant [11, 23]. Ongoing research explores methods to enhance titanium's wear resistance, including alloying with other metals (often alloyed with Al, V, Nb, Ta and Zr) and utilizing surface modification techniques [22]. Moreover, Co-Cr alloys, which are characterized by their high wear resistance and surface hardness [24], find application in joint replacement prostheses like the total knee and femoral-head hip replacements [11]. Although Co-Cr are also used in other various medical devices such as dental [25] and cardiovascular implants [26], ongoing research is devoted to enhance the biocompatibility and bone integration, limiting their high manufacturing costs and toxicity (associated with nickel content). Despite Co-Cr alloys having relatively lower osteointegration compared to other alloys, they are also used as screws in trauma plating systems due to the weak integration with bone tissues, as they can be easily removed after healing the bone fracture. Notably, the exploration of Ta-, Ti- or Zr-based coatings to augment osteointegration of Co-Cr alloys represents a key area of focus for future researchers [23]. Another category of “traditional” biomaterials comprises stainless steels, primarily composed of Fe, Cr, and Ni. The addition of Cr and Ni promotes the formation of a passive Cr_2O_3 layer on the surface, providing excellent corrosion resistance to the material [11]. Despite notable advantages such as low-cost and superior mechanical properties, including high tensile and elastic strength, stainless steel has limited applications in medical implants due to its susceptibility to corrosion in chloride-rich environments. This corrosion can lead to the release of toxic heavy metal ions, such as Ni and Cr, harmful to the human body [27]. In literature, there have been attempts to develop Ni-free austenitic stainless steels. For instance, Salahinejad *et al.* [28] substituted Ni with N, enhancing the strength, corrosion resistance, wear resistance, and biocompatibility in comparison with Ni-containing steel.

A representative scheme of the advantages and disadvantages of the abovementioned corrosion-resistant metals are illustrated in **Fig. 1.2**.

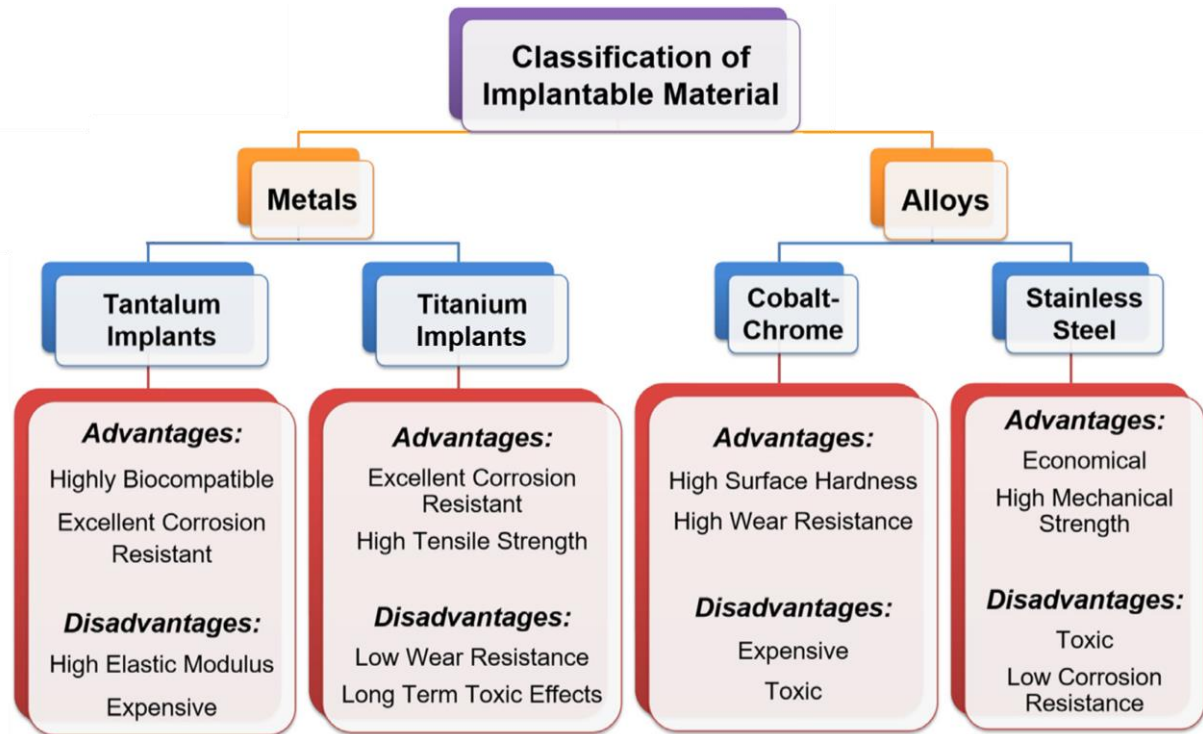


Fig. 1.2 Scheme illustrating the advantages and disadvantages of some corrosion-resistant biomedical materials. Adapted from [11].

However, generally the mechanical properties of the traditional orthopedic implant do not match the mechanical properties of the human bone and usually the permanent metallic devices need to be removed after one or two years from the implantation, requiring a second invasive intervention [29]. Furthermore, regarding the specific case of cardiovascular applications, Ta, Co-Cr and stainless steel are currently employed in stents [26] and the use of permanent devices might lead to drawbacks associated to inflammation, thrombosis and in-stent restenosis [30, 31].

To overcome the problematics raised by permanent devices, while maintaining their advantages to efficiently support the damaged apparatus during the healing period, intensive research has been carried out on biomaterials that undergo gradual controlled degradation in the human body after the required healing period.

1.1.2 Biodegradable biomaterials

Recently, metal, polymers, ceramic or composites are widely studied as promising biodegradable materials. Polymeric materials have been used in various medical application since the 60's [32] and during the decades, numerous studies were aimed to develop biodegradable polymers modifying the chemical-physical properties of the material such as monomers, molecular weight, polydispersity and crystallinity to match the physical and biological requirements depending on the specific application needs [33]. One of most commonly used biodegradable polymer for tissue engineering is the polylactic acid (PLA) because of its biocompatibility and degradation period about 12 months [34]. In addition, as for other synthetic polymers, it is possible to tune the desired chiral composition (of L- and D-lactide) during the synthesis to better tune its properties including tailored-made porosity, degradation time and mechanical characteristics [34]. In the specific case of cardiovascular applications, for example, polymeric stents have been widely studied due to remarkable biosorption capabilities despite their main weakness in insufficient mechanical properties [35]. Generally, polymers such as PLLA have a lower tensile strength and stiffness than traditional metals, thus the PLLA stent wire must be thicker (about 240%) in order to provide the same strength [36]. The increased stent strut thickness may inhibit the vascular healing, it will reduce the axial flexibility limiting the deliverability of the device and restenosis and thrombosis issues may rise [35, 37]. In addition, another family of biodegradable material concern composites and hybrid systems such as metal (Fe or Ti) particles were incorporated in polymeric (PLA) scaffolds are intensively investigated because of their ability to improve both mechanical properties and biocompatibility of polymeric materials, granting a better integration of the prosthesis and a more efficient tissue or bone healing [38, 39]. Recently, stents consisting of PLA matrix with embedded Mg particles were manufactured varying the volume quantities of Mg. The comparison between the as-fabricated struts and those tested after immersion test in simulated body fluid solution for 7 days are illustrated in **Fig. 1.3**. The authors demonstrated that the degradation rate of this composite material, along with the loss of mechanical properties, can be tuned through tailoring of the Mg content [40].

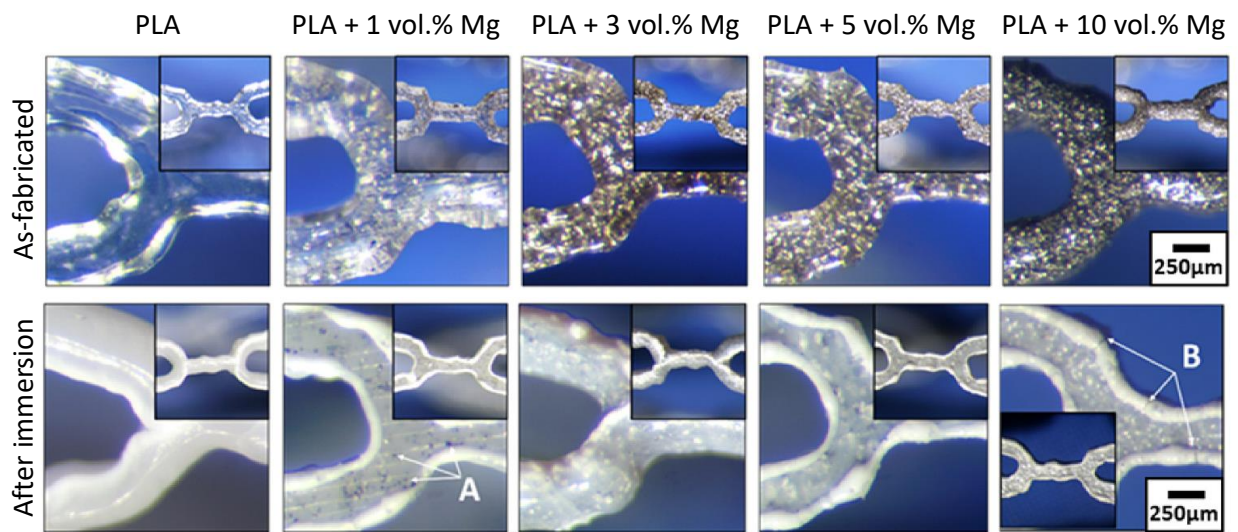


Fig. 1.3 Overview of as-fabricated stent struts and after 7 days of immersion in simulated body fluid solution. Label A highlights the intact interfaces of the PLA/Mg, while B depicts the strut's expansion resulting from progressive degradation. Adapted from [40].

On the other hand, in case of biodegradable metals, the most studied materials are Mg-, Zn- and Fe-based polycrystalline alloys [29, 41-43] and they constitute a novel class of bioabsorbable materials thanks to the improved mechanical properties and biocompatibility compared to synthetic polymers [38]. In particular, Mg and its alloys are currently considered as new generation biodegradable metal materials because of their low density (1.74 g/cm^3), yield strength to compression (65-100 MPa) and elastic modulus (43 GPa) comparable with those of human bone (103-222 MPa and 7.7-21.8 GPa, respectively), making these material of extreme interest for biodegradable orthopedic applications [1, 44]. These similarities between the elasticity of Mg and human bone limit the negative effects of stress-shielding phenomenon [1]. However, Mg cannot be used in its pure form because of the very high corrosion rates and its corrosion causes hydrogen development [45]. For this reason it is often alloyed with other elements, such as Zn, Ca, Sr and Zr to reduce the grain size, improving the yield strength and corrosion properties, efficiently reducing the H_2 gas evolution [7]. Similar to Mg, Zn stands out as one of the most essential elements for the human body, actively participating in enzymatic reactions, protein synthesis and arterial blood

pressure regulation [5]. Additionally, a study by Bown *et al.* [46] indicated that the application of pure Zn wire implanted into the blood vessel exhibits ideal physiological behavior for biodegradable stent applications. Similarly, Yang *et al.* [47] investigated the degradation of pure Zn stent in a rabbit abdominal aorta showing the excellent biocompatibility with no severe inflammation, thrombosis or other diseases, verifying the feasibility of Zn as biodegradable stent material. However, the strength and ductility of zinc do not meet the criteria proposed by Werkhoven *et al.* for biodegradable Mg-based stent materials ($\sigma_{UTS} > 300$ MPa and elongation $> 20\%$) [48]. Furthermore, Zn alloys are known to exhibit low resistance to creep, relatively limited cyclic fatigue strength and high susceptibility to aging and static recrystallization. Considering these investigations, Zn has emerged as a promising candidate for biodegradable metals and recent studies, both *in vitro* and *in vivo*, have been dedicated to optimizing its physical properties through alloying with Mg, Al, Ag, Cu, Mn, Fe and Zr [5]. On the contrary, Fe alloys are another promising candidate for biodegradable applications because of their superior static strength and ductility, cyclic fatigue strength, creep resistance and immunity to aging and static recrystallization, which surpass those of Zn alloys [5]. Moreover, Fe is actively involved in numerous critical roles within the human body, contributing to hemoglobin production and being stored in the liver as ferritin [6]. The combination of non-toxicity and superior mechanical properties positions Fe as a promising material for load-bearing applications. However, the utilization of Fe and Fe-based alloys poses certain challenges, particularly due to their extremely low corrosion rate, high elastic modulus leading to stress shielding, and non-compatibility with magnetic resonance imaging for ferromagnetic alloys [49]. Nevertheless, researchers have documented various manufacturing and processing techniques for the development of Fe-based biomaterials, including powder metallurgy [50], casting [51], electrodeposition [52] and additive manufacturing [53] aimed at accelerating its degradation rate and improving the overall biological response. Alongside fabrication processes, alloying stands out as a prominent method for enhancing the degradation characteristics of Fe. For instance, among the alloying elements, Mn is commonly combined with Fe (up to

30 wt.%) to reduce its corrosion resistance due to the formation of a less noble Fe-Mn solid solution that degrades much faster than pure Fe [54]. Similarly, the addition of less-conventional elements such as Ag, Pt, Pd and Au reported increasing the degradation rate of Fe-based alloys through galvanic coupling [55-57]. Furthermore, several studies have focused on investigating surface modifications of porous Fe-alloys with polymeric coatings to enhance both biocompatibility and biodegradability [58-60]. **Fig. 1.4** represents a schematic draw of the evolution of mechanical integrity and degradation as function of implantation time of an ideal biodegradable material compared with currently investigated Mg-, Zn-, and Fe-based alloys. **Table 1.3** resumes the main advantages and disadvantages of these biomaterials.

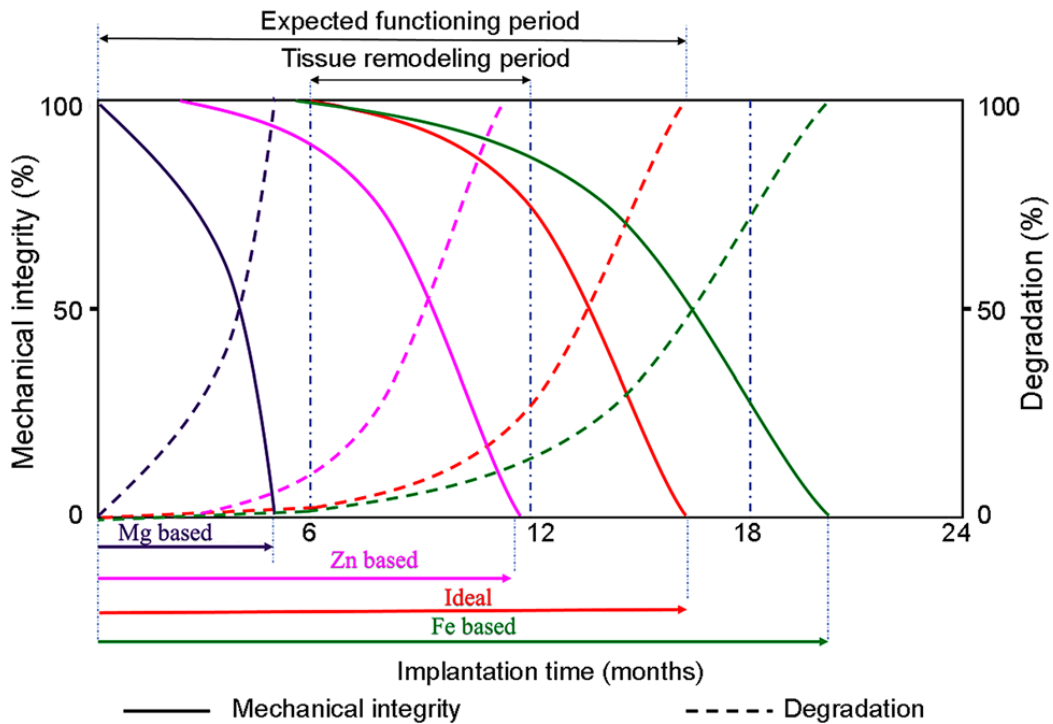


Fig. 1.4 Schematic representation of the evolution of mechanical integrity and degradation of most used biodegradable materials. Adapted from [49].

Table 1.3 Main advantages and disadvantages of Mg-, Zn-, and Fe-based alloys [49].

| <i>Material</i> | <i>Advantages</i> | <i>Disadvantages</i> |
|-----------------|---|---|
| Mg-based | Biodegradable Biocompatible Promote biomineralisation and osseointegration Density and elastic modulus close to that of human bone and thereby reduce the chances of stress shielding MRI compatible An essential element for the human body | Extremely high degradation rate H ₂ gas evolution by degradation Local rise of pH near the implant site Poor mechanical strength for load-bearing application Premature loss of mechanical integrity |
| Zn-based | Biodegradable Acceptable biocompatibility Good processability No H ₂ gas evolution by degradation Non-toxic degradation products | Poor mechanical strength Proneness to creep Age hardening |
| Fe-based | Biodegradable High tensile strength and formability Acceptable biocompatibility MRI compatible (in austenitic phase) No H ₂ gas evolution by degradation | Very low degradation rate High elastic modulus leads to stress shielding Non-MRI compatible for ferromagnetic Fe and its alloys |

Apart from alloying, another approach to enhancing the corrosion and mechanical properties of these biomedical Mg-, Zn-, or Fe-alloys involves grain refinement to achieve materials with nano-sized crystalline structures.

1.2 Nanocrystalline materials

Nanocrystalline materials, with grain size smaller than 100 nanometers, have consistently demonstrated enhanced and novel properties compared to their traditional coarse-grain counterparts, attributed to the distinct microstructural features characterized by a significantly larger fraction of grain boundaries [61-65]. In

the 1950s, Hall and Petch [66, 67] showed the inverse relationship between the yield stress σ_y (related to the hardness) and the square root of grain size, d , in polycrystalline materials through the equation:

$$\sigma_y = \sigma_0 + kd^{-\frac{1}{2}} \quad (1)$$

Where σ_0 is the resistance to dislocation motion within the grains, k is a constant related to the material and the specific grain boundaries, d is the average grain size. This relationship between σ_y and grain size is explained by the fact that dislocation pile-ups are formed at grain boundaries, rising the yielding stress needed for a slip to propagate among two different grains [66, 67]. Also, dislocations interact with each other, inhibiting their movement in high dislocation density regions, like near or at grain boundaries, increasing the yielding stress necessary for plastic flow [68]. However, several studies suggested that Hall-Petch effect is not universally valid for nanocrystalline materials [69] and in particular, Pande *et al.* [70] debated the validity of Eq. (1) when only few dislocations are present in a pile-up. This motivated the development of other models which take into account the dislocation density [71] or considering the grain as composite (core-mantle) material [64, 69]. At the same time, the inverse Hall-Petch phenomenon is a less common but still important observation in some nanocrystalline materials [72]. Several studies reported that as grain sizes become extremely small (typically less than 30 nm [64]), the relationship between grain size and hardness can become counterintuitive. Instead of hardness increasing with decreasing grain size (as predicted by the Hall-Petch equation), it is observed that in some cases, the hardness decreases as grain size decreases [64, 69]. This inverse Hall-Petch effect could be explained by a transition from dislocation-based plasticity to a grain boundary sliding mechanism [69, 73-75]. Moreover, a recent simulation study conducted by H. Zhang *et al.*, [73] showed three distinct regimes of the flow stress depending on the grain size (**Fig. 1.5**). As the grain diameter decreases, a classical Hall-Petch behavior is evident until the grain size reaches 15 nm. Within the range of grain sizes spanning from 15 to 3 nm, the material's strength decreases with reducing the grain size, indicating an inverse Hall-Petch effect. Lastly, for grain sizes smaller than 3

nm (~12 particles), the simulated material undergoes amorphization, and the authors observe a power-law strengthening phenomenon due to the blocking of shear bands by crystalline grains [73].

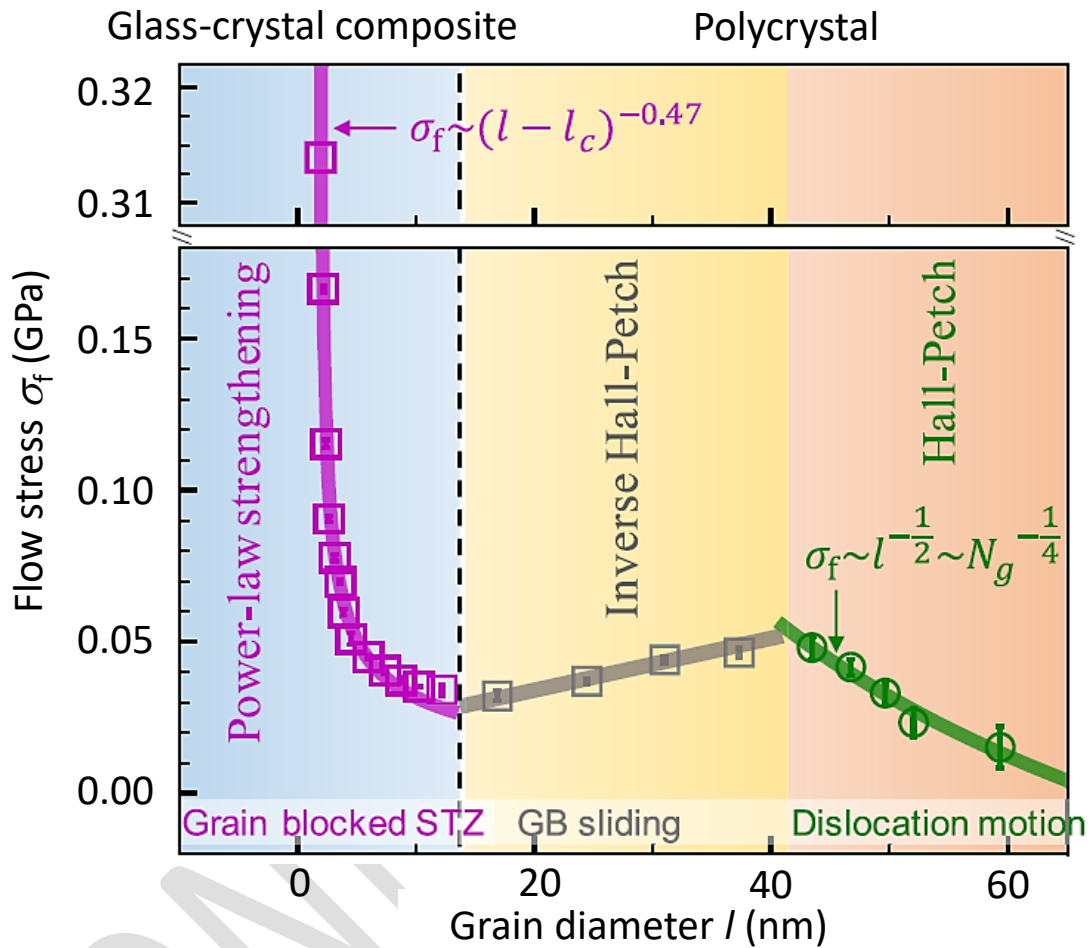


Fig. 1.5 Three regimes of flow stress σ_f depending on the grain diameter l . N_g represents the grain size. Adapted from [73].

However, several researchers have debated the existence of the inverse Hall-Petch based because of the lack of available experimental evidence, and this effect could also results from processing artifacts or induced grain growth during mechanical testing [64, 69]. In particular, the challenging processes of fabrication of nanocrystalline material can introduce defects and impurities that weaken the material [64, 76].

All these effects occurring at the nanoscale enhance mechanical, electrical, thermal, and optical properties, granting nanocrystalline materials significant attention in

various fields due to their potential. For example, in the field of electronics, nanocrystalline silicon thin films have emerged as promising candidates for solar cells due to their enhanced charge carrier mobility and reduced parasitic absorption compared to amorphous silicon [77]. Another example regards nanocrystalline ceramics, which exhibit exceptional dielectric properties, making them valuable for capacitors and electronic devices [78]. Furthermore, nanocrystalline materials have also demonstrated their high potential in biomedical applications, highlighting their improved biocompatibility and mechanical strength compared to conventional coarse-grains materials. Indeed, the reduction in grain size from 25 μm to 150 nm in pure Ti, designed for permanent dental implants, reported an increase in both σ_y and ultimate tensile strength (σ_{UTS}) from 530 and 700 MPa up to 1267 and 1330 MPa, respectively [79]. In addition, TiCu alloy proved to be a valid candidate as new permanent orthopedic material because of its excellent mechanical properties (microhardness of 10 GPa and toughness of 8.14 MPa $\text{m}^{1/2}$), improved biocompatibility and antibacterial activity [80]. Nevertheless, other nanocrystalline materials were developed for biomedical purposes as well [1-4, 7]. Especially for Mg-based alloys, which are of high interest for biodegradable implant applications, the most common grain refinement method employed is the addition of Zr [81], used in Mg-Ca-Zr [82], Mg-Zr-Sr [83] and Mg-Zr-Al [84] alloys, fabricating a grain-refined structure with enhanced mechanical properties [85]. Nanocrystalline Mg-based materials (with crystal sizes in the range of 45-70 nm) are well-documented for their substantially improved mechanical properties, biocompatibility and corrosion behavior compared to conventional coarse-grained metallic materials [86, 87]. In addition, an increase in ultimate tensile strength has been documented, with values rising from 65-100 MPa for pure Mg [88] to 200-290 MPa for grain-refined Mg-Zr-Sr alloys [83, 89, 90]. In addition, Mg-Nd-Zn-Zr alloy with a refined grain structure ($\sim 1 \mu\text{m}$ grain size), achieved through cyclic extrusion and compression methods, showed a remarkable improvement of 71% in yield strength, 28% in ultimate tensile strength, and a substantial 154% increase in elongation compared to their coarse-grain counterparts [91].

The fabrication of bulk nanocrystalline materials might be challenging and generally involves severe plastic deformation methods or high energetic processes. The study by Suryanarayana [92] provides a comprehensive overview of mechanical alloying, especially high-energy milling, as a powerful method for producing nanocrystalline materials with controlled grain sizes and compositions. Alternatively, the addition of grain-refinement elements is often employed to produce nanocrystalline materials. Another possibility for the traditional fabrication methods of bulk nanocrystalline materials are the PVD techniques. These offer several advantages, such as the fabrication of nanocrystalline coatings without the need for severe plastic deformation techniques. Also, it allows for easy screening of the effects of chemical content across a wide range of compositions.

However, crystalline coarse-grain alloys and composite materials might be susceptible to localized corrosion and pitting phenomena, making the development of alloys with uniform and controlled corrosion rates still an open challenge [93]. In this context, a promising solution could be the use of metallic glasses (MGs) which are receiving more and more attention due to their disordered atomic structure turning into a source of unique physical properties. In particular, the homogeneous and isotropic atomic structure of metallic glasses could lead to generalized corrosion with tunable corrosion rates as a function of the alloy composition [93]. Furthermore, this class of material is characterized by a disordered atomic structure that leads to high elastic deformations (>2%) and yield strength (~2 GPa) in combination with good corrosion and wear resistance, above those of most of the traditional crystalline materials [94, 95].

1.3 Metallic glasses

Bulk metallic glasses (BMGs) represent a category of amorphous materials characterized by a disordered atomic structure lacking long-range periodicity. However, the term 'amorphous' is somewhat inaccurate as the arrangement of their atoms is not entirely random. Their atomic structure exhibits short-range order (< 5 Å) and even medium-range order (< 30 Å), owing to constraints associated with atomic coordination and cluster packing [96]. The short-range order (SRO) is experimentally

examined through diffraction experiments, revealing a primary diffuse halo followed by less intense ones, as represented in **Fig. 1.6**.

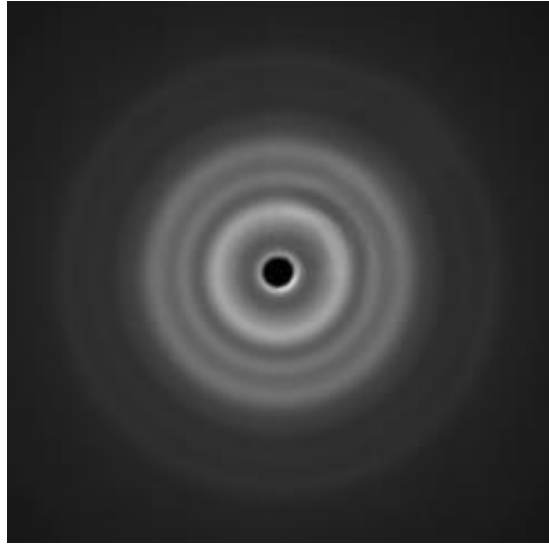


Fig. 1.6 Typical diffraction halos of amorphous material.

Subsequently, Fourier inversion of the diffraction data allows the derivation of the pair distribution function (PDF) $G(r) = 4\pi r(\rho(r) - \rho_0)$, illustrating the average evolution of atomic density $\rho(r)$ at a distance r from the reference atom and ρ_0 represent the macroscopic material density. The typical PDF of a metallic glass is represented in **Fig. 1.7**. At small distances $\rho(r)$ fluctuates assuming positive values when $\rho(r) > \rho_0$ (shell) and negative values when $\rho(r) < \rho_0$ (anti-shell). The first peak, corresponding to the maximum in atomic density, enables the calculation of the average coordination number within the first coordination shell of a reference atom. The second peak reflects the atomic density in the second coordination shell, appearing noticeably broader than the first due to the gradually less defined atomic structure and giving insights on the medium-range-order (MRO). At greater distances, the PDF is subject to damping, approaching 0, indicating a lack of long-range-order (LRO) when $\rho(r)$ reaches values equal to ρ_0 . However, while the PDF provides an averaged understanding of local atomic density, it does not determine a unique set of atomic positions. In such cases, reverse Monte Carlo and *ab initio* methods are frequently utilized to simulate the PDF, providing comprehensive insights into various models of atomic packing through the comparison with the experimental PDF [97].

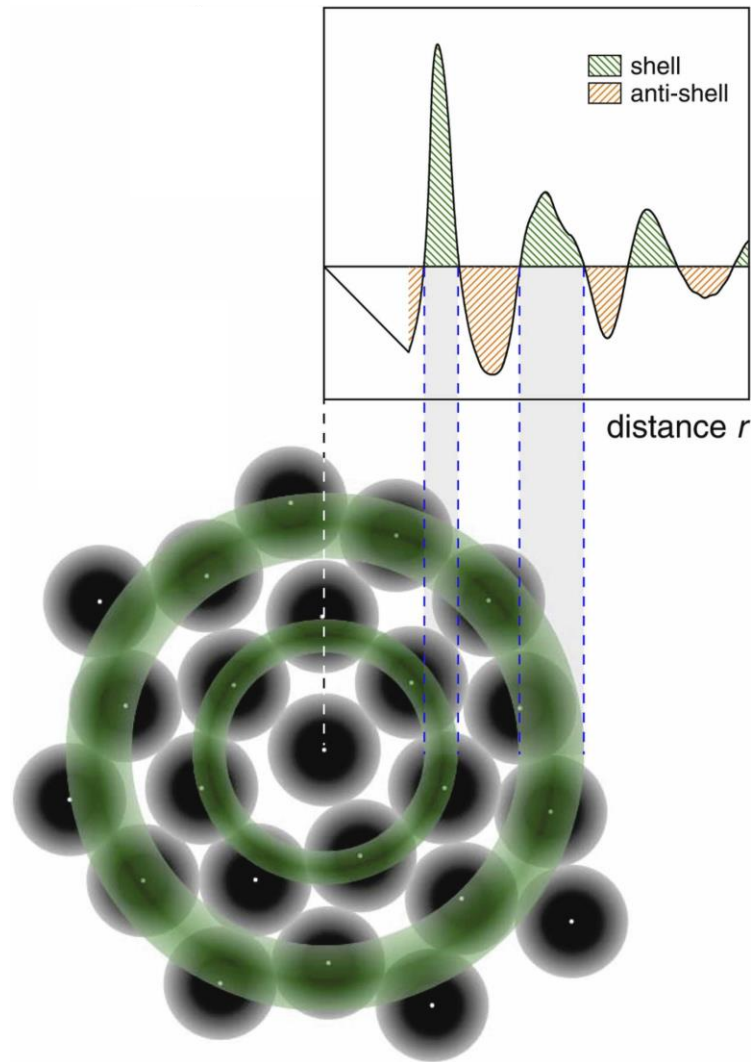


Fig. 1.7 Scheme of $G(r)$ of a monoatomic amorphous material, showing the definition of shells and anti-shells and their relation with the atomic configuration. Adapted from [98].

Initially, due to their amorphous nature, the structure of metallic glasses was associated with liquid metals, and during the '60s, several authors investigated the structure of monometallic liquids [99-101]. Among these, Bernal [99] introduced the concept of a dense random packing of hard spheres, in which the liquid could be modeled as a collection of five structural unit cells. Specifically, the regular tetrahedron unit has the highest packing fraction, resulting in the most efficient structure for ordering four identical atoms. Considering a central atom where each atom must touch three others to form a regular tetrahedron, it becomes apparent that

the maximum number of shell atoms is 12. However, it proves impossible to efficiently fill the space with tetrahedral geometries alone, and this structure leaves a gap in the shell [102, 103], which can be filled by rearranging the shell atoms at an equal distance from each other (5% longer than the distance between central and shell atoms) [104] forming a regular icosahedron. However, the fivefold rotational symmetry of this icosahedral cluster makes it impossible to fill the space with a periodic repetition (generating the LRO) of regular icosahedra, leading to a phenomenon known as geometrical frustration (**Fig. 1.8**) [105, 106].

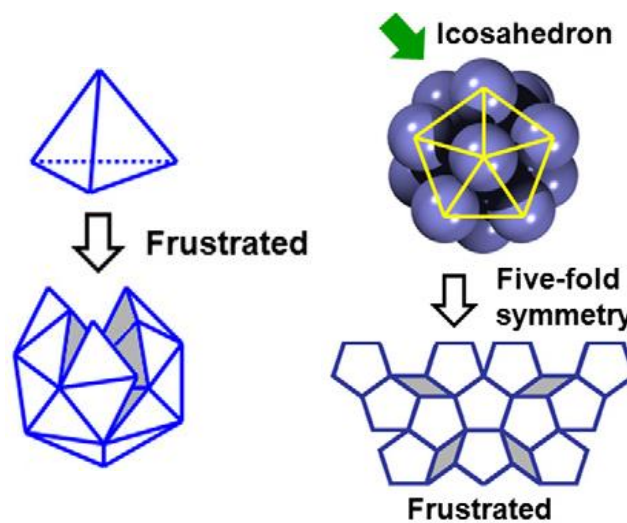


Fig. 1.8 Frustration geometry of the polyhedral packing of identical hard spheres. Adapted from [106].

In the case of multi-elemental metallic glasses, which are more reliable in reality, the atomic structure is composed of atoms with different sizes. Therefore, by permitting distortions such as slight changes in bond lengths and bond angles, as well as the presence of other polyhedral clusters, it becomes feasible to fill the 3D space. This concept, commonly referred to as polytetrahedral packing, is often coupled with PDF analysis to effectively describe the SRO, relating the structure to the mechanical properties of the material [107, 108].

The process of how these SRO clusters are then organized to constitute the bulk of the alloy—i.e., the formation of the MRO—is currently under intensive investigation. The solute-centered clusters interconnect through vertex-, edge-, or face-sharing

schemes, forming the MRO. Additionally, valuable insights into cluster interconnections can be obtained using the PDF. By plotting the reduced PDF, defined as $g(r) = \frac{G(r)}{4\pi r \rho_0} + 1$ and normalizing the position of the first peak, it is possible to gather information about the connections between clusters comprising 1, 2, or 3 atoms, as illustrated in **Fig. 1.9** [109, 110].

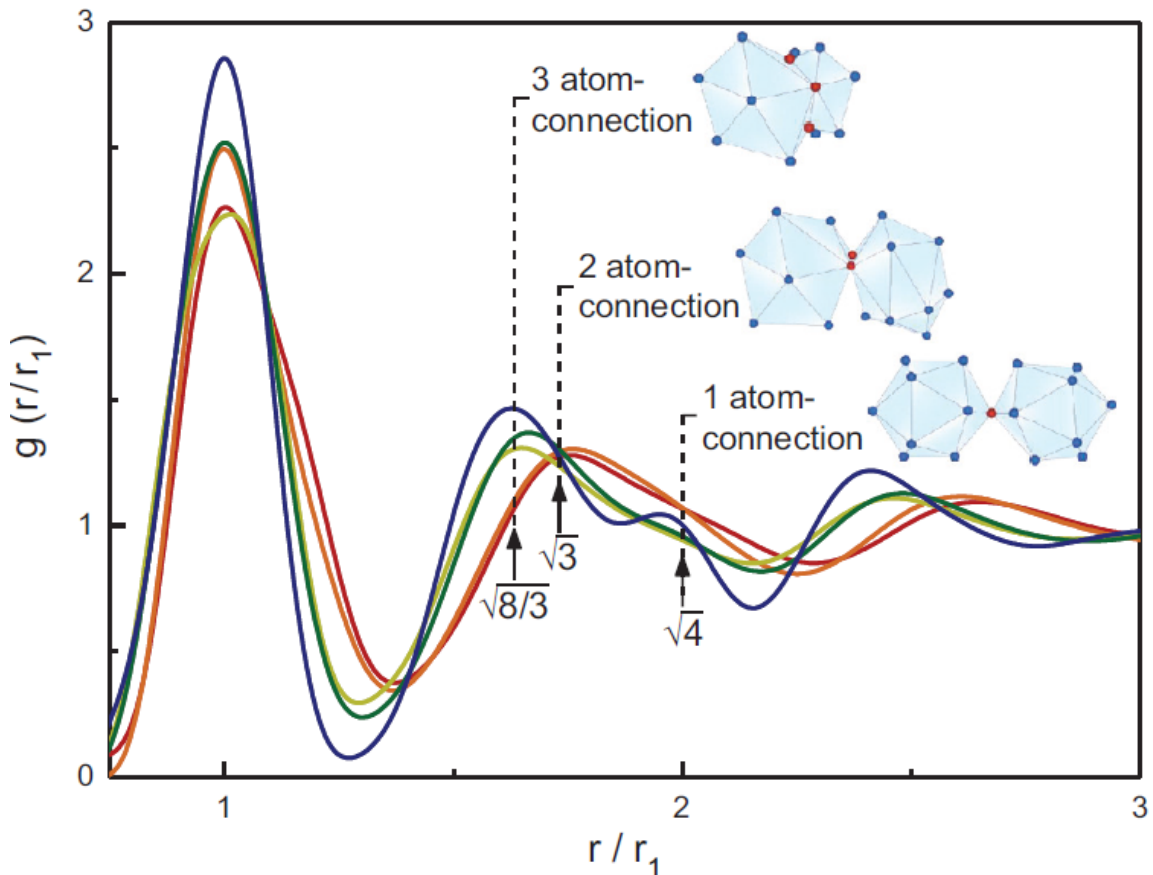


Fig. 1.9 a) Reduced PDF $g(r)$ normalized by the first peak position (r_1) for equiatomic binary $\text{Cu}_{50}\text{Zr}_{50}$ to denary $(\text{CuNiBeCoFe})_{50}(\text{ZrTiHfTaNb})_{50}$ metallic glasses. The r/r_1 values $\sqrt{4}$, $\sqrt{3}$, and $\sqrt{8/3}$ represent the 1, 2, and 3 atom-connection of clusters, respectively. Adapted from [110].

This characteristic disordered structure of BMGs is attained by employing a cooling rate larger than a critical value (R_c) in order to prevent the atomic rearrangement during crystallization and preserving their frozen liquid-like structure. In addition, R_c results inversely proportional to the glass forming ability (GFA) of the material [111]

which can be improved by considering the empirical rules presented by Inoue *et al.* [112]: *i)* The alloy must consist of at least three components. The formation of glass is facilitated by an increasing number of components within the alloy system. *ii)* A substantial difference in atomic size among the constituent elements of the alloy is essential. It is recommended that the atomic size differences between the main constituents should be approximately 12% or greater. *iii)* Negative heat of mixing is crucial for the (primary) constituent elements within the alloy system.

Considering these criteria, the first is linked to the thermodynamic and kinetic aspects of glass formation, while the second is centered on the topological aspects related to the structure and packing of atoms. The third criterion is fundamental to enable the mixing of atoms (alloying) and the subsequent development of a uniform glassy phase [113]. Several studies are aimed to improving the GFA of the amorphous materials by optimizing the chemical composition based on the aforementioned criteria, adding ternary, quaternary, or more elements to binary alloys, and designing novel BMGs with enhanced properties [114-116]. However, the investigation of the effect of chemical composition on the GFA is still an open scientific domain [117, 118]. Furthermore, establishing a correlation between the chemical composition, atomic structure, and physical properties of a material is of utmost importance in materials science, but due to the absence of long-range order in amorphous materials, designing and simulating them pose significantly greater challenges compared to their crystalline counterparts. Despite these difficulties, delving into the intricacies of amorphous materials is crucial for unlocking their unique potential and advancing various fields of research and applications [119]. In this context, the combination of experimental studies with molecular dynamics (MD) approaches is a widely adopted strategy to gain comprehensive insights into the intricate correlation between the chemical composition, atomic structure, and physical properties of amorphous materials [120, 121]. However, these studies often focus on a single composition or examine the impact of minor additions, and only a few studies are aimed to investigate relationship structure-physical properties along the entire compositional range.

The appeal of developing metallic glasses lies in their superior mechanical properties and corrosion behavior compared to their crystalline counterpart. Notably, the high yield strength (~ 2 GPa) and large elastic strain limit ($\sim 2\%$) along with their easy formability in the supercooled liquid region, make the BMGs an attractive choice for various structural applications in sport equipment, ranging from golf clubs, tennis rackets, baseball bats, snowboards, skis and beyond [122]. Moreover, the lack of crystalline features in amorphous materials results in remarkable high homogeneity at the nanoscale and one-order-of-magnitude lower shrinkage during solidification in comparison to typical casting alloys, rendering this class of materials highly interesting in the field of micro-machines [123]. For example, M. Ishida *et al.* [124] compared the wear resistance of Ni-based BMG microgears with that of those made of conventional carbon tools. The findings, illustrated in **Fig. 1.10**, reveal that the geared motor employing BMG gears exhibited a lifetime of 2500 hours, whereas the geared motor utilizing carbon steel gears lasted only 8 hours.

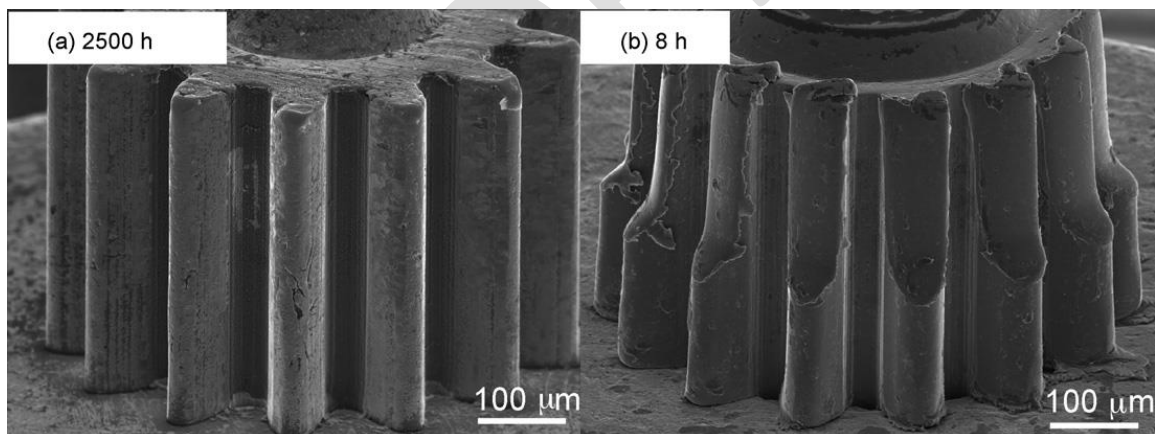


Fig. 1.10 Comparison of SEM images of the a) BMG gear after durability test for 2500h and b) the steel gear after 8h rotation.

Among the various applications of BMGs, these non-crystalline materials also find use in the biomedical field as durable (corrosion-resistant) implants. For instance, Zhu *et al.* [125] capitalized on the advantages of Ti-based alloys, such as low density, excellent biocompatibility, and corrosion resistance, to develop Ti-based BMG for biomedical purposes. Their work demonstrated a compressive strength of 1950 MPa, Young's modulus of 82 GPa, and an elastic elongation of 2.3%. Subsequently, the same

research group produced a composite $Ti_{40}Zr_{10}Cu_{36}Pd_{14}$ BMG with 6 vol.% hydroxyapatite, enhancing the material's surface bioactivity without significantly affecting its mechanical properties. This development proved to be a viable solution for dental replacements as well as in the manufacturing of plates and screws for bone fixation [126]. Moreover, metallic glasses have been proposed as promising materials for surgical blades that are sharper and more durable than those made of steel, while also being less expensive than diamond and easier to manufacture. Furthermore, in the past few decades, Mg-based BMGs have garnered significant interest for their potential as biodegradable implants. Various studies in the literature have highlighted the use of Ca and Zn as alloying elements in the development of Mg-based BMGs for biomedical applications, owing to the essential role both elements play in the human body [127]. The exploration of Mg-Zn-Ca BMGs for biodegradable applications has garnered attention within the research community. Several studies have focused on enhancing mechanical properties and corrosion resistance, both *in vitro* and *in vivo*, with minimal hydrogen evolution, while ensuring good biocompatibility [128-133]. Notably, few studies of the last decade assessed the viability of using Zr-based BMG in (permanent) self-expandable stents through experimental, finite element analysis, and molecular dynamic simulations. The findings suggested that BMG can effectively serve as materials for aortic stents, capable of being crimped without experiencing mechanical failure [134-136].

However, due to the lack of defects, such as dislocations, able to accommodate plastic deformation, the major drawback of BMGs is their macroscopically brittle behavior at T_{room} with the deformation entirely localized in narrow (~10 nm thick) shear bands (SBs) [137]. For example, Mg-based BMGs reported elongation values about 2.5-3%, close to the elastic limit, and highlighting the reduced plasticity of these materials [127]. Guo *et al.* [138] developed tensile test specimens of Zr-based MG at the sub-micron scale demonstrating that this brittle behavior of BMGs can be mitigated reducing the sample dimensions. Specifically, mechanical size effects can be activated for sub-micrometer scale samples hindering shear band nucleation and

propagation as in the case of thin film metallic glasses (TFMGs), in which large plastic deformation (~15%) and toughness are reported [139, 140].

1.4 Biomedical TFMGs and research challenges

The macroscopic brittleness of BMGs, along the difficulties of their fabrication in form of thick sheets (> 10 mm), limited their real-time application and commercialization. Instead of cooling the liquid phase until solidification, the vapor-to-solid condensation of atoms can prepare amorphous layers favoring the formation of glassy alloys with supersaturated immiscible elements.

Studies on the synthesis and characterization of TFMGs are relatively recent, as most of the efforts have been focused on BMGs. In addition, TFMGs are considered as “hot topic” in biomaterials research as promising coatings for enhancing the physical properties of the bare material. Zr-based TFMGs are widely investigated for surgical tools, for example, ZrCuAlAgSi and ZrCuNiAlSi TFMGs deposited on surgical stainless steel blade showed an improvement in both sharpness and durability [141, 142]. Similarly, ZrCuAlTa TFMGs showed beneficial effect on coated needles offering a non-sticky behavior due to the very low friction compared to the bare metal (**Fig. 1.11**) [143]. Moreover, Fe-based TFMGs showed an improvements in sharpness compared to the uncoated blade as well [144].

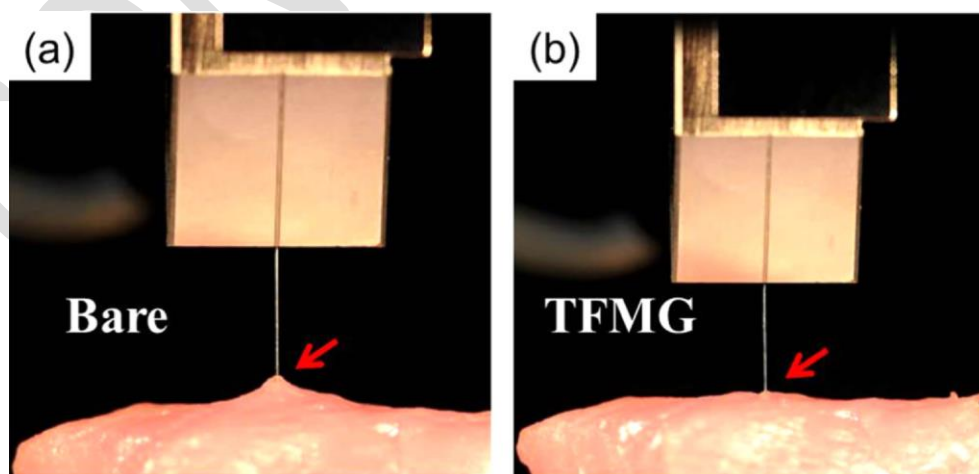


Fig. 1.11 Images of a) bare stainless steel and b) TFMG-coated needles when retracted from pork muscle [145].

Similarly to surgical tools, Zr-, Ti-, Fe- and Mg-based TFMGs represent a class of materials useful to improve the surface properties of bioimplants. Specifically, ZrCuAlAg TFMGs, when deposited on steels and Ti-alloys, have shown to promote antibacterial behavior and facilitate the formation of a bone-like apatite layer on the implant, thereby improving integration [146, 147]. The addition of elements such as Cu in Ti-based TFMGs as pointed out good antibacterial properties [148]. Furthermore, Ti-based TFMGs also showed a better blood compatibility when compared with bare Ti and nontoxicity in vivo [149]. Similarly, Fe-Zr-Nb TFMG coating improved the biocompatibility of bare stainless steel [150]. Regarding biomaterials with biodegradation purposes, only few studies are aimed to develop biodegradable TFMGs. The majority of those are investigating Mg-based (often alloyed with Zn and Ca) TFMGs because they maintain the advantages of Mg-based materials, while reducing the corrosion rate and hydrogen evolution [132, 151].

Despite these promising applications of Zr-, Ti-, Fe-, and Mg-based TFMGs, the development of Zn-based TFMGs is substantially lacking. Moreover, exploring of wide range of composition of glassy alloys, instead to a single one, is crucial in order to find the optimal chemical composition and structure to well-match the mechanical and physical requirements listed in **Table 1.1** and **Table 1.2**. However, only a few recent experimental studies are aimed to explore the relationships between structural and mechanical properties of TFMGs such as ZrCu [152], ZrCo [153] and ZrNi [154] across the entire range of composition. These amorphous binary alloys consist of Zr as an early transition (TE) metal combined with another late transition (TL) alloying metal known for their high GFA. Additionally, investigations have recently been conducted also on ZrTa [155, 156] TFMGs, which are composed of two TE metals. However, the existing literature lacks substantial knowledge regarding binary Zn-containing (as TL) metallic glasses such as ZnZr and ZnMg TFMGs as well as BMGs [157]. Nevertheless, exploring the relationship between chemical composition, atomic structure, and mechanical properties for these systems remains an unknown field and an ongoing challenge. For instance, several compositions of sputtered ZnZr TFMG have revealed non-toxic behavior in Zn-rich films and good corrosion resistance in simulated body

fluid solution (SBF) [158]. Similar features are expected for Mg-Zr films, but the effects on the structural and physical properties of Mg due to large Zr addition (>10% at.) remain unknown. In contrast with Zn-Zr and Mg-Zn binary alloys, for which a reasonable large glass-forming ability [158, 159] and various possible intermetallic compounds [160-162] are observed, Mg and Zr are immiscible elements [163] and they are not predisposed to form intermetallic or glassy solid solutions. Since the amorphization of Mg-Zr is largely unfavorable, the investigation of nano-sized grains coatings becomes necessary and this work aims to explore the Mg-Zr domain as preliminary step toward developing a novel ternary amorphous Mg-Zn-Zr alloy because of its expected specific structural and physical properties suitable for biodegradable implants. Additionally, recent studies have aimed to investigate the structural and mechanical properties of various binary Zr-based amorphous and nanocrystalline films, including ZrCu [152, 164-166], ZrCo [166], ZrNi [166, 167], ZrFe [168], ZrTa [169]. However, the majority of these studies have employed metallic element pairs with either HCP-FCC or body-centered cubic BCC-FCC crystal structures associated with soft and hard metals, leaving the fundamental understanding of the mixing of HCP-HCP crystal structures relatively unexplored.

1.5 References

- [1] V. Tsakiris, C. Tardei, F.M. Clicinschi, Biodegradable Mg alloys for orthopedic implants—A review, *Journal of Magnesium and Alloys* 9(6) (2021) 1884-1905.
- [2] P. Sekar, S. Narendranath, V. Desai, Recent progress in in vivo studies and clinical applications of magnesium based biodegradable implants—a review, *Journal of Magnesium and Alloys* 9(4) (2021) 1147-1163.
- [3] M. Hashemi, R. Alizadeh, T.G. Langdon, Recent advances using equal-channel angular pressing to improve the properties of biodegradable Mg–Zn alloys, *Journal of Magnesium and Alloys* (2023).
- [4] S. Kamrani, C. Fleck, Biodegradable magnesium alloys as temporary orthopaedic implants: a review, *Biometals* 32 (2019) 185-193.
- [5] G. Li, H. Yang, Y. Zheng, X.-H. Chen, J.-A. Yang, D. Zhu, L. Ruan, K. Takashima, Challenges in the use of zinc and its alloys as biodegradable metals: perspective from biomechanical compatibility, *Acta biomaterialia* 97 (2019) 23-45.
- [6] G. Papanikolaou, K. Pantopoulos, Iron metabolism and toxicity, *Toxicology and applied pharmacology* 202(2) (2005) 199-211.
- [7] F. Kiani, C. Wen, Y. Li, Prospects and strategies for magnesium alloys as biodegradable implants from crystalline to bulk metallic glasses and composites—A review, *Acta biomaterialia* 103 (2020) 1-23.
- [8] T.S. Keller, Z. Mao, D.M. Spengler, Young's modulus, bending strength, and tissue physical properties of human compact bone, *J Orthop Res* 8(4) (1990) 592-603.
- [9] Y. Liu, B. Lu, Z. Cai, Recent Progress on Mg- and Zn-Based Alloys for Biodegradable Vascular Stent Applications, *Journal of Nanomaterials* 2019 (2019) 1-16.
- [10] Z.Q. Zhang, Y.X. Yang, J.A. Li, R.C. Zeng, S.K. Guan, Advances in coatings on magnesium alloys for cardiovascular stents - A review, *Bioactive materials* 6(12) (2021) 4729-4757.
- [11] S. Gautam, D. Bhatnagar, D. Bansal, H. Batra, N. Goyal, Recent advancements in nanomaterials for biomedical implants, *Biomedical Engineering Advances* 3 (2022) 100029.
- [12] M. Hussain, S.M. Khan, K. Al-Khaled, M. Ayadi, N. Abbas, W. Chammam, Performance analysis of biodegradable materials for orthopedic applications, *Materials Today Communications* 31 (2022) 103167.
- [13] G. Mohandas, N. Oskolkov, M.T. McMahon, P. Walczak, M. Janowski, Porous tantalum and tantalum oxide nanoparticles for regenerative medicine, *Acta Neurobiol Exp (Wars)* 74(2) (2014) 188-196.
- [14] G. Maccauro, P.R. Iommetti, F. Muratori, L. Raffaelli, P.F. Manicone, C. Fabbriciani, An overview about biomedical applications of micron and nano size tantalum, *Recent patents on biotechnology* 3(3) (2009) 157-165.

- [15] G. Mani, D. Porter, K. Grove, S. Collins, A. Ornberg, R. Shulfer, A comprehensive review of biological and materials properties of Tantalum and its alloys, *Journal of Biomedical Materials Research Part A* 110(6) (2022) 1291-1306.
- [16] D. Cristea, I. Ghiuta, D. Munteanu, Tantalum based materials for implants and prostheses applications, *Bulletin of the Transilvania University of Brasov. Series I: Engineering Sciences* (2015) 151-158.
- [17] H. Li, Z. Yao, J. Zhang, X. Cai, L. Li, G. Liu, J. Liu, L. Cui, J. Huang, The progress on physicochemical properties and biocompatibility of tantalum-based metal bone implants, *SN Applied Sciences* 2 (2020) 1-14.
- [18] R. Wauthle, J. Van Der Stok, S.A. Yavari, J. Van Humbeeck, J.-P. Kruth, A.A. Zadpoor, H. Weinans, M. Mulier, J. Schrooten, Additively manufactured porous tantalum implants, *Acta biomaterialia* 14 (2015) 217-225.
- [19] T.D. Brown, A.B. Ferguson, Mechanical property distributions in the cancellous bone of the human proximal femur, *Acta Orthopaedica Scandinavica* 51(1-6) (1980) 429-437.
- [20] M. Sarraf, E. Rezvani Ghomi, S. Alipour, S. Ramakrishna, N. Liana Sukiman, A state-of-the-art review of the fabrication and characteristics of titanium and its alloys for biomedical applications, *Bio-design and Manufacturing* (2021) 1-25.
- [21] S. Liang, Review of the design of titanium alloys with low elastic modulus as implant materials, *Advanced Engineering Materials* 22(11) (2020) 2000555.
- [22] L.C. Zhang, L.Y. Chen, A review on biomedical titanium alloys: recent progress and prospect, *Advanced Engineering Materials* 21(4) (2019) 1801215.
- [23] C. Skjöldebrand, J.L. Tipper, P. Hatto, M. Bryant, R.M. Hall, C. Persson, Current status and future potential of wear-resistant coatings and articulating surfaces for hip and knee implants, *Materials Today Bio* 15 (2022) 100270.
- [24] P. Sahoo, S.K. Das, J.P. Davim, Tribology of materials for biomedical applications, mechanical behaviour of biomaterials, Elsevier 2019, pp. 1-45.
- [25] A. Mace, P. Khullar, C. Bouknight, J.L. Gilbert, Corrosion properties of low carbon CoCrMo and additively manufactured CoCr alloys for dental applications, *Dental Materials* 38(7) (2022) 1184-1193.
- [26] A. Scafa Udriște, A.-G. Niculescu, A.M. Grumezescu, E. Bădilă, Cardiovascular stents: A review of past, current, and emerging devices, *Materials* 14(10) (2021) 2498.
- [27] A.J. Ortiz, E. Fernández, A. Vicente, J.L. Calvo, C. Ortiz, Metallic ions released from stainless steel, nickel-free, and titanium orthodontic alloys: toxicity and DNA damage, *American Journal of Orthodontics and Dentofacial Orthopedics* 140(3) (2011) e115-e122.
- [28] E. Salahinejad, M.J. Hadianfard, D.D. Macdonald, S. Sharifi-Asl, M. Mozafari, K.J. Walker, A.T. Rad, S.V. Madihally, L. Tayebi, In vitro electrochemical corrosion and cell viability studies on nickel-free stainless steel orthopedic implants, *PloS one* 8(4) (2013) e61633.

- [29] V. Tsakiris, C. Tardei, F.M. Clicinschi, Biodegradable Mg alloys for orthopedic implants – A review, *Journal of Magnesium and Alloys* 9(6) (2021) 1884-1905.
- [30] B.E. Claessen, J.P. Henriques, F.A. Jaffer, R. Mehran, J.J. Piek, G.D. Dangas, Stent thrombosis: a clinical perspective, *JACC Cardiovasc Interv* 7(10) (2014) 1081-92.
- [31] P.H. Grewe, T. Deneke, A. Machraoui, J. Barmeyer, K.M. Muller, Acute and chronic tissue response to coronary stent implantation: pathologic findings in human specimen, *J Am Coll Cardiol* 35(1) (2000) 157-63.
- [32] J. Charnley, Anchorage of the femoral head prosthesis to the shaft of the femur, *The Journal of bone and joint surgery. British volume* 42(1) (1960) 28-30.
- [33] N. Iqbal, A.S. Khan, A. Asif, M. Yar, J.W. Haycock, I.U. Rehman, Recent concepts in biodegradable polymers for tissue engineering paradigms: A critical review, *International Materials Reviews* 64(2) (2019) 91-126.
- [34] L.S. Nair, C.T. Laurencin, Biodegradable polymers as biomaterials, *Progress in polymer science* 32(8-9) (2007) 762-798.
- [35] Y. Shen, X. Yu, J. Cui, F. Yu, M. Liu, Y. Chen, J. Wu, B. Sun, X. Mo, Development of Biodegradable Polymeric Stents for the Treatment of Cardiovascular Diseases, *Biomolecules* 12(9) (2022).
- [36] H.Y. Ang, H. Bulluck, P. Wong, S.S. Venkatraman, Y. Huang, N. Foin, Bioresorbable stents: Current and upcoming bioresorbable technologies, *Int J Cardiol* 228 (2017) 931-939.
- [37] H. Zhang, W. Zhang, H. Qiu, G. Zhang, X. Li, H. Qi, J. Guo, J. Qian, X. Shi, X. Gao, D. Shi, D. Zhang, R. Gao, J. Ding, A Biodegradable Metal-Polymer Composite Stent Safe and Effective on Physiological and Serum-Containing Biomimetic Conditions, *Adv Healthc Mater* 11(22) (2022) e2201740.
- [38] D. Jiang, F. Ning, Y. Wang, Additive manufacturing of biodegradable iron-based particle reinforced polylactic acid composite scaffolds for tissue engineering, *Journal of Materials Processing Technology* 289 (2021).
- [39] J. Lee, H. Lee, K.-H. Cheon, C. Park, T.-S. Jang, H.-E. Kim, H.-D. Jung, Fabrication of poly(lactic acid)/Ti composite scaffolds with enhanced mechanical properties and biocompatibility via fused filament fabrication (FFF)-based 3D printing, *Additive Manufacturing* 30 (2019).
- [40] E. Hasanpur, A. Ghazavizadeh, A. Sadeghi, M. Haboussi, In vitro corrosion study of PLA/Mg composites for cardiovascular stent applications, *Journal of the Mechanical Behavior of Biomedical Materials* 124 (2021) 104768.
- [41] P.K. Bowen, E.R. Shearier, S. Zhao, R.J. Guillory, 2nd, F. Zhao, J. Goldman, J.W. Drelich, Biodegradable Metals for Cardiovascular Stents: from Clinical Concerns to Recent Zn-Alloys, *Adv Healthc Mater* 5(10) (2016) 1121-40.
- [42] E. Mostaed, M. Sikora-Jasinska, J.W. Drelich, M. Vedani, Zinc-based alloys for degradable vascular stent applications, *Acta Biomater* 71 (2018) 1-23.

- [43] R. Gorejová, L. Haverová, R. Oriňaková, A. Oriňak, M. Oriňak, Recent advancements in Fe-based biodegradable materials for bone repair, *Journal of Materials Science* 54(3) (2018) 1913-1947.
- [44] L. Yuan, S. Ding, C. Wen, Additive manufacturing technology for porous metal implant applications and triple minimal surface structures: A review, *Bioactive materials* 4 (2019) 56-70.
- [45] R. Radha, D. Sreekanth, Insight of magnesium alloys and composites for orthopedic implant applications—a review, *Journal of magnesium and alloys* 5(3) (2017) 286-312.
- [46] P.K. Bowen, J. Drelich, J. Goldman, Zinc exhibits ideal physiological corrosion behavior for bioabsorbable stents, *Advanced materials* 25(18) (2013) 2577-2582.
- [47] H. Yang, C. Wang, C. Liu, H. Chen, Y. Wu, J. Han, Z. Jia, W. Lin, D. Zhang, W. Li, Evolution of the degradation mechanism of pure zinc stent in the one-year study of rabbit abdominal aorta model, *Biomaterials* 145 (2017) 92-105.
- [48] R. Werkhoven, W. Sillekens, J. Van Lieshout, *Processing aspects of magnesium alloy stent tube*, Springer 2016.
- [49] V.M. Rabeeh, T. Hanas, Progress in manufacturing and processing of degradable Fe-based implants: A review, *Progress in Biomaterials* 11(2) (2022) 163-191.
- [50] P. Liu, D. Zhang, Y. Dai, J. Lin, Y. Li, C. Wen, Microstructure, mechanical properties, degradation behavior, and biocompatibility of porous Fe-Mn alloys fabricated by sponge impregnation and sintering techniques, *Acta biomaterialia* 114 (2020) 485-496.
- [51] C.S. Obayi, R. Tolouei, C. Paternoster, S. Turgeon, B.A. Okorie, D.O. Obikwelu, G. Cassar, J. Buhagiar, D. Mantovani, Influence of cross-rolling on the micro-texture and biodegradation of pure iron as biodegradable material for medical implants, *Acta biomaterialia* 17 (2015) 68-77.
- [52] J. He, H. Ye, Y. Li, J. Fang, Q. Mei, X. Lu, F. Ren, Cancellous-bone-like porous iron scaffold coated with strontium incorporated octacalcium phosphate nanowhiskers for bone regeneration, *ACS Biomaterials Science & Engineering* 5(2) (2019) 509-518.
- [53] B. Paul, A. Lode, A.-M. Placht, A. Voß, S. Pilz, U. Wolff, S. Oswald, A. Gebert, M. Gelinsky, J. Hufenbach, Cell-material interactions in direct contact culture of endothelial cells on biodegradable iron-based stents fabricated by laser powder bed fusion and impact of ion release, *ACS Applied Materials & Interfaces* 14(1) (2021) 439-451.
- [54] H. Hermawan, A. Purnama, D. Dube, J. Couet, D. Mantovani, Fe-Mn alloys for metallic biodegradable stents: degradation and cell viability studies, *Acta biomaterialia* 6(5) (2010) 1852-1860.
- [55] T. Huang, J. Cheng, D. Bian, Y. Zheng, Fe-Au and Fe-Ag composites as candidates for biodegradable stent materials, *Wiley Online Library*, 2016, pp. 225-240.

- [56] M. Schinhammer, A.C. Hänzi, J.F. Löffler, P.J. Uggowitzer, Design strategy for biodegradable Fe-based alloys for medical applications, *Acta biomaterialia* 6(5) (2010) 1705-1713.
- [57] Y.F. Zheng, X.N. Gu, F. Witte, Biodegradable metals, *Materials Science and Engineering: R: Reports* 77 (2014) 1-34.
- [58] L. Haverová, R. Oriňaková, A. Oriňak, R. Gorejova, M. Baláž, P. Vanýsek, M. Kupkova, M. Hrubovčáková, P. Mudroň, J. Radoňák, An in vitro corrosion study of open cell iron structures with PEG coating for bone replacement applications, *Metals* 8(7) (2018) 499.
- [59] M. Hrubovčáková, M. Kupková, M. Džupon, M. Giretová, L. Medvecký, R. Džunda, Biodegradable polylactic acid and polylactic acid/hydroxyapatite coated iron foams for bone replacement materials, *Int. J. Electrochem. Sci* 12(12) (2017) 11122-11136.
- [60] R. Gorejová, R. Oriňaková, Z. Orságová Králová, M. Baláž, M. Kupková, M. Hrubovčáková, L. Haverová, M. Džupon, A. Oriňak, F. Kaňavský, In vitro corrosion behavior of biodegradable iron foams with polymeric coating, *Materials* 13(1) (2020) 184.
- [61] H. Gleiter, Nanocrystalline materials, *Advanced Structural and Functional Materials: Proceedings of an International Seminar Organized by Deutsche Forschungsanstalt für Luft-und Raumfahrt (DLR), Köln, June 1991, Springer, 1991, pp. 1-37.*
- [62] H. Gleiter, J. Weissmüller, O. Wollersheim, R. Würschum, Nanocrystalline materials: a way to solids with tunable electronic structures and properties?, *Acta Materialia* 49(4) (2001) 737-745.
- [63] C. Suryanarayana, The structure and properties of nanocrystalline materials: issues and concerns, *Jom* 54 (2002) 24-27.
- [64] M.A. Meyers, A. Mishra, D.J. Benson, Mechanical properties of nanocrystalline materials, *Progress in materials science* 51(4) (2006) 427-556.
- [65] T.J. Rupert, J.C. Trenkle, C.A. Schuh, Enhanced solid solution effects on the strength of nanocrystalline alloys, *Acta Materialia* 59(4) (2011) 1619-1631.
- [66] E. Hall, The deformation and ageing of mild steel: III discussion of results, *Proceedings of the Physical Society. Section B* 64(9) (1951) 747.
- [67] N. Petch, The cleavage strength of polycrystals, *J. Iron Steel Inst.* 174 (1953) 25-28.
- [68] J. Li, Y. Chou, The role of dislocations in the flow stress grain size relationships, *Metallurgical and materials transactions B* 1 (1970) 1145-1159.
- [69] S.N. Naik, S.M. Walley, The Hall–Petch and inverse Hall–Petch relations and the hardness of nanocrystalline metals, *Journal of Materials Science* 55(7) (2020) 2661-2681.
- [70] C. Pande, R. Masumura, R. Armstrong, Pile-up based Hall-Petch relation for nanoscale materials, *Nanostructured materials* 2(3) (1993) 323-331.

- [71] L. Murr, Dislocation ledge sources: dispelling the myth of Frank–Read source importance, *Metallurgical and Materials Transactions A* 47 (2016) 5811-5826.
- [72] B. Braeckman, F. Misják, G. Radnóczy, M. Caplovicová, P. Djemia, F. Tétard, L. Belliard, D. Depla, The nanostructure and mechanical properties of nanocomposite Nb_x-CoCrCuFeNi thin films, *Scripta Materialia* 139 (2017) 155-158.
- [73] H. Zhang, F. Liu, G. Ungar, Z. Zheng, Q. Sun, Y. Han, A regime beyond the Hall–Petch and inverse-Hall–Petch regimes in ultrafine-grained solids, *Communications Physics* 5(1) (2022) 329.
- [74] H. Conrad, Grain-size dependence of the flow stress of Cu from millimeters to nanometers, *Metallurgical and Materials Transactions A* 35 (2004) 2681-2695.
- [75] C. Pande, K. Cooper, Nanomechanics of Hall–Petch relationship in nanocrystalline materials, *Progress in materials science* 54(6) (2009) 689-706.
- [76] C.C. Koch, J. Narayan, The inverse Hall-Petch effect—Fact or artifact?, *MRS Online Proceedings Library (OPL)* 634 (2000) B5. 1.1.
- [77] M. Sharma, J. Panigrahi, V.K. Komarala, Nanocrystalline silicon thin film growth and application for silicon heterojunction solar cells: a short review, *Nanoscale Advances* 3(12) (2021) 3373-3383.
- [78] A.M. Bakr, A.B.A. Hammad, A.R. Wassel, A.M.E. Nahrawy, A. Mansour, Influence of Al, Fe, and Cu on the microstructure, diffused reflectance, THz, and dielectric properties for ZnTiO₃ nanocrystalline, *International Journal of Materials Engineering Innovation* 12(2) (2021) 115-133.
- [79] A.V. Polyakov, L. Dluhoš, G.S. Dyakonov, G.I. Raab, R.Z. Valiev, Recent advances in processing and application of nanostructured titanium for dental implants, *Advanced Engineering Materials* 17(12) (2015) 1869-1875.
- [80] S.M. Javadhesari, S. Alipour, M. Akbarpour, Biocompatibility, osseointegration, antibacterial and mechanical properties of nanocrystalline Ti-Cu alloy as a new orthopedic material, *Colloids and Surfaces B: Biointerfaces* 189 (2020) 110889.
- [81] Y. Lee, A. Dahle, D. StJohn, The role of solute in grain refinement of magnesium, *Metallurgical and Materials transactions A* 31 (2000) 2895-2906.
- [82] S.-Y. Chang, H. Tezuka, A. Kamio, Mechanical properties and structure of ignition-proof Mg–Ca–Zr alloys produced by squeeze casting, *materials Transactions, JIM* 38(6) (1997) 526-535.
- [83] Y. Li, C. Wen, D. Mushahary, R. Sravanthi, N. Harishankar, G. Pande, P. Hodgson, Mg–Zr–Sr alloys as biodegradable implant materials, *Acta biomaterialia* 8(8) (2012) 3177-3188.
- [84] E.F. Emley, *Principles of magnesium technology*, (No Title) (1966).
- [85] G. Chandra, A. Pandey, Preparation strategies for Mg-alloys for biodegradable orthopaedic implants and other biomedical applications: a review, *IRBM* (2020), DOI.

- [86] H. Li, P. Wang, C. Wen, Recent Progress on Nanocrystalline Metallic Materials for Biomedical Applications, *Nanomaterials* 12(12) (2022) 2111.
- [87] M. Kowalski, M. Jurczyk, Ultrafine grained Mg-1Zn-1Mn-0.3 Zr alloy and its corrosion behaviour, *J. Achiev. Mater. Manuf. Eng* 74 (2016) 53-59.
- [88] M.P. Staiger, A.M. Pietak, J. Huadmai, G. Dias, Magnesium and its alloys as orthopedic biomaterials: a review, *Biomaterials* 27(9) (2006) 1728-1734.
- [89] Y. Ding, J. Lin, C. Wen, D. Zhang, Y. Li, Mechanical properties, in vitro corrosion and biocompatibility of newly developed biodegradable Mg-Zr-Sr-Ho alloys for biomedical applications, *Scientific reports* 6(1) (2016) 31990.
- [90] F. Kiani, J. Lin, A. Vahid, K. Munir, C. Wen, Y. Li, Microstructures, mechanical properties, corrosion, and biocompatibility of extruded Mg-Zr-Sr-Ho alloys for biodegradable implant applications, *Journal of Magnesium and Alloys* 11(1) (2023) 110-136.
- [91] X. Zhang, G. Yuan, Z. Wang, Mechanical properties and biocorrosion resistance of Mg-Nd-Zn-Zr alloy improved by cyclic extrusion and compression, *Materials Letters* 74 (2012) 128-131.
- [92] C. Suryanarayana, Mechanical alloying and milling, *Progress in materials science* 46(1-2) (2001) 1-184.
- [93] M. Jafary-Zadeh, G. Praveen Kumar, P.S. Branicio, M. Seifi, J.J. Lewandowski, F. Cui, A Critical Review on Metallic Glasses as Structural Materials for Cardiovascular Stent Applications, *J Funct Biomater* 9(1) (2018).
- [94] M. Ashby, A. Greer, Metallic glasses as structural materials, *Scripta Materialia* 54(3) (2006) 321-326.
- [95] C.A. Schuh, T.C. Hufnagel, U. Ramamurty, Mechanical behavior of amorphous alloys, *Acta Materialia* 55 (2007) 4067-4109.
- [96] H. Sheng, W. Luo, F. Alamgir, J. Bai, E. Ma, Atomic packing and short-to-medium-range order in metallic glasses, *Nature* 439(7075) (2006) 419-425.
- [97] S. Evertz, D. Music, V. Schnabel, J. Bednarcik, J.M. Schneider, Thermal expansion of Pd-based metallic glasses by ab initio methods and high energy X-ray diffraction, *Scientific reports* 7(1) (2017) 15744.
- [98] M.E. Stiehler, N.T. Panagiotopoulos, D.S. Keeble, Y.P. Ivanov, M. Menelaou, M.R. Jolly, A.L. Greer, K. Georgarakis, The effect of Ni or Co additions on the structure of Zr₆₀Cu₃₀Al₁₀ bulk metallic glass revealed by high-energy synchrotron radiation, *Materials Today Communications* 31 (2022) 103531.
- [99] J. Bernal, Geometry of the structure of monatomic liquids, *Nature* 185(4706) (1960) 68-70.
- [100] G.D. Scott, Packing of spheres: packing of equal spheres, *Nature* 188(4754) (1960) 908-909.

- [101] J. Finney, Random packings and the structure of simple liquids. I. The geometry of random close packing, *Proceedings of the Royal Society of London. A. Mathematical and Physical Sciences* 319(1539) (1970) 479-493.
- [102] D.R. Nelson, Order, frustration, and defects in liquids and glasses, *Physical Review B* 28(10) (1983) 5515.
- [103] D.R. Nelson, F. Spaepen, Polytetrahedral order in condensed matter, *Solid State Physics* 42 (1989) 1-90.
- [104] F.C. Frank, J.S. Kasper, Complex alloy structures regarded as sphere packings. I. Definitions and basic principles, *Acta Crystallographica* 11(3) (1958) 184-190.
- [105] H.S.M. Coxeter, *Introduction to geometry*, John Wiley & Sons, Inc.1969.
- [106] Y. Cheng, E. Ma, Atomic-level structure and structure–property relationship in metallic glasses, *Progress in materials science* 56(4) (2011) 379-473.
- [107] C.H. Li, C. Poltronieri, G. Abadias, P. Djemia, Computational approach to identify structural and elastic relationship in metastable crystalline and amorphous alloy thin films: Mo_{1-x}Ni_x and Mo_{1-x}Si_x case studies, *Surface and Coatings Technology* (2023) 130168.
- [108] C. Poltronieri, A. Brognara, F. Bignoli, S. Evertz, P. Djemia, D. Faurie, F. Challali, C. Li, L. Belliard, G. Dehm, Mechanical properties and thermal stability of ZrCuAl_x thin film metallic glasses: Experiments and first-principle calculations, *Acta Materialia* 258 (2023) 119226.
- [109] J. Ding, E. Ma, M. Asta, R.O. Ritchie, Second-nearest-neighbor correlations from connection of atomic packing motifs in metallic glasses and liquids, *Scientific reports* 5(1) (2015) 17429.
- [110] J.S. Lee, H.S. Oh, W. Kim, C.W. Ryu, J.Y. Kim, H.J. Chang, J. Gu, K. Yao, B. Murty, E.S. Park, Anomalous behavior of glass-forming ability and mechanical response in a series of equiatomic binary to denary metallic glasses, *Materialia* 9 (2020) 100505.
- [111] Z. Lu, C. Liu, A new glass-forming ability criterion for bulk metallic glasses, *Acta materialia* 50(13) (2002) 3501-3512.
- [112] A. Inoue, B. Shen, N. Nishiyama, Development and applications of late transition metal bulk metallic glasses, *Bulk metallic glasses* (2008) 1-25.
- [113] C. Suryanarayana, A. Inoue, *Bulk metallic glasses*, CRC press2017.
- [114] A. Javed, M.M. Khan, J. Camiller, M. Greenlee-Wacker, W. Haider, I. Shabib, Property optimization of Zr-Ti-X (X = Ag, Al) metallic glass via combinatorial development aimed at prospective biomedical application, *Surface and Coatings Technology* 372 (2019) 278-287.
- [115] M.X. Li, S.F. Zhao, Z. Lu, A. Hirata, P. Wen, H.Y. Bai, M. Chen, J. Schroers, Y. Liu, W.H. Wang, High-temperature bulk metallic glasses developed by combinatorial methods, *Nature* 569(7754) (2019) 99-103.

- [116] L. Lang, H. Deng, Z. Tian, F. Gao, W. Hu, D. Wen, Y. Mo, The effect of Mo addition on structure and glass forming ability of Ni-Zr alloys, *Journal of Alloys and Compounds* 775 (2019) 1184-1198.
- [117] M.X. Li, Y.T. Sun, C. Wang, L.W. Hu, S. Sohn, J. Schroers, W.H. Wang, Y.H. Liu, Data-driven discovery of a universal indicator for metallic glass forming ability, *Nat Mater* 21(2) (2022) 165-172.
- [118] Y.X. Zhang, G.C. Xing, Z.D. Sha, L.H. Poh, A two-step fused machine learning approach for the prediction of glass-forming ability of metallic glasses, *Journal of Alloys and Compounds* 875 (2021).
- [119] V. Schnabel, M. Kohler, D. Music, J. Bednarcik, W.J. Clegg, D. Raabe, J.M. Schneider, Ultra-stiff metallic glasses through bond energy density design, *J Phys Condens Matter* 29(26) (2017) 265502.
- [120] Y. Yang, J. Zhou, F. Zhu, Y. Yuan, D.J. Chang, D.S. Kim, M. Pham, A. Rana, X. Tian, Y. Yao, S.J. Osher, A.K. Schmid, L. Hu, P. Ercius, J. Miao, Determining the three-dimensional atomic structure of an amorphous solid, *Nature* 592(7852) (2021) 60-64.
- [121] L.S. Luo, B.B. Wang, F.Y. Dong, Y.Q. Su, E.Y. Guo, Y.J. Xu, M.Y. Wang, L. Wang, J.X. Yu, R.O. Ritchie, J.J. Guo, H.Z. Fu, Structural origins for the generation of strength, ductility and toughness in bulk-metallic glasses using hydrogen microalloying, *Acta Materialia* 171 (2019) 216-230.
- [122] Liquidmetal Technologies homepage. (<http://www.liquidmetal.com>).
- [123] P. Sharma, W. Zhang, K. Amiya, H. Kimura, A. Inoue, Nanoscale patterning of Zr-Al-Cu-Ni metallic glass thin films deposited by magnetron sputtering, *Journal of nanoscience and nanotechnology* 5(3) (2005) 416-420.
- [124] M. Ishida, H. Takeda, N. Nishiyama, K. Kita, Y. Shimizu, Y. Saotome, A. Inoue, Wear resistivity of super-precision microgear made of Ni-based metallic glass, *Materials Science and Engineering: A* 449 (2007) 149-154.
- [125] S. Zhu, X. Wang, F. Qin, A. Inoue, A new Ti-based bulk glassy alloy with potential for biomedical application, *Materials Science and Engineering: A* 459(1-2) (2007) 233-237.
- [126] S. Zhu, X. Wang, G. Xie, F. Qin, M. Yoshimura, A. Inoue, Formation of Ti-based bulk glassy alloy/hydroxyapatite composite, *Scripta Materialia* 58(4) (2008) 287-290.
- [127] S.J.B. Bin, K.S. Fong, B.W. Chua, M. Gupta, Mg-based bulk metallic glasses: A review of recent developments, *Journal of magnesium and alloys* 10(4) (2022) 899-914.
- [128] B. Zberg, P.J. Uggowitzer, J.F. Löffler, MgZnCa glasses without clinically observable hydrogen evolution for biodegradable implants, *Nature materials* 8(11) (2009) 887-891.
- [129] B. Zberg, E.R. Arata, P.J. Uggowitzer, J.F. Löffler, Tensile properties of glassy MgZnCa wires and reliability analysis using Weibull statistics, *Acta Materialia* 57(11) (2009) 3223-3231.

- [130] Y.-Y. Zhao, X. Zhao, Structural relaxation and its influence on the elastic properties and notch toughness of Mg–Zn–Ca bulk metallic glass, *Journal of Alloys and Compounds* 515 (2012) 154-160.
- [131] X. Zhang, G. Chen, T. Bauer, Mg-based bulk metallic glass composite with high bio-corrosion resistance and excellent mechanical properties, *Intermetallics* 29 (2012) 56-60.
- [132] J. Li, F.S. Gittleson, Y. Liu, J. Liu, A.M. Loye, L. McMillon-Brown, T.R. Kyriakides, J. Schroers, A.D. Taylor, Exploring a wider range of Mg–Ca–Zn metallic glass as biocompatible alloys using combinatorial sputtering, *Chemical Communications* 53(59) (2017) 8288-8291.
- [133] C. Jin, Z. Liu, W. Yu, C. Qin, H. Yu, Z. Wang, Biodegradable Mg–Zn–Ca-Based Metallic Glasses, *Materials* 15(6) (2022) 2172.
- [134] G. Praveen Kumar, M. Jafary-Zadeh, R. Tavakoli, F. Cui, Feasibility of using bulk metallic glass for self-expandable stent applications, *J Biomed Mater Res B Appl Biomater* 105(7) (2017) 1874-1882.
- [135] G. Praveen Kumar, M. Jafary-Zadeh, F. Cui, Deployment of a Bulk Metallic Glass-Based Self-Expandable Stent in a Patient-Specific Descending Aorta, *ACS Biomater Sci Eng* 2(11) (2016) 1951-1958.
- [136] L. Huang, C. Pu, R.K. Fisher, D.J. Mountain, Y. Gao, P.K. Liaw, W. Zhang, W. He, A Zr-based bulk metallic glass for future stent applications: Materials properties, finite element modeling, and in vitro human vascular cell response, *Acta biomaterialia* 25 (2015) 356-368.
- [137] A.L. Greer, Y.Q. Cheng, E. Ma, Shear bands in metallic glasses, *Materials Science and Engineering R* 74(4) (2013) 71-132.
- [138] H. Guo, P. Yan, Y. Wang, J. Tan, Z. Zhang, M. Sui, E. Ma, Tensile ductility and necking of metallic glass, *Nature materials* 6(10) (2007) 735-739.
- [139] J.P. Chu, J.S.C. Jang, J.C. Huang, H.S. Chou, Y. Yang, J.C. Ye, Y.C. Wang, J.W. Lee, F.X. Liu, P.K. Liaw, Y.C. Chen, C.M. Lee, C.L. Li, C. Rullyani, Thin film metallic glasses: Unique properties and potential applications, *Thin Solid Films* 520(16) (2012) 5097-5122.
- [140] M. Ghidelli, H. Idrissi, S. Gravier, J.-J. Blandin, J.-P. Raskin, D. Schryvers, T. Pardoën, Homogeneous flow and size dependent mechanical behavior in highly ductile Zr₆₅Ni₃₅ metallic glass films, *Acta Materialia* 131 (2017) 246-259.
- [141] P. Tsai, Y. Lin, J. Li, S. Jian, J. Jang, C. Li, J. Chu, J. Huang, Sharpness improvement of surgical blade by means of ZrCuAlAgSi metallic glass and metallic glass thin film coating, *Intermetallics* 31 (2012) 127-131.
- [142] P. Tsai, T. Li, K. Hsu, J. Chiou, J. Jang, J. Chu, Effect of coating thickness on the cutting sharpness and durability of Zr-based metallic glass thin film coated surgical blades, *Thin Solid Films* 618 (2016) 36-41.

- [143] J.P. Chu, C.-C. Yu, Y. Tanatsugu, M. Yasuzawa, Y.-L. Shen, Non-stick syringe needles: Beneficial effects of thin film metallic glass coating, *Scientific reports* 6(1) (2016) 31847.
- [144] J.S.-C. Jang, P.-H. Tsai, A.-Z. Shiao, T.-H. Li, C.-Y. Chen, J.P. Chu, J.-G. Duh, M.-J. Chen, S.-H. Chang, W.-C. Huang, Enhanced cutting durability of surgical blade by coating with Fe-based metallic glass thin film, *Intermetallics* 65 (2015) 56-60.
- [145] S.T. Rajan, A. Arockiarajan, Thin film metallic glasses for bioimplants and surgical tools: A review, *Journal of Alloys and Compounds* 876 (2021) 159939.
- [146] S. Thanka Rajan, M. Karthika, A. Bendavid, B. Subramanian, Apatite layer growth on glassy Zr 48 Cu 36 Al 8 Ag 8 sputtered titanium for potential biomedical applications, *Applied Surface Science* 369 (2016) 501-509.
- [147] A.C. Parau, G.A. Juravlea, J. Raczowska, C. Vitelaru, M. Dinu, K. Awsiuik, D.M. Vranceanu, E. Ungureanu, C.M. Cotrut, A. Vladescu, Comparison of 316L and Ti6Al4V biomaterial coated by ZrCu-based thin films metallic glasses: Structure, morphology, wettability, protein adsorption, corrosion resistance, biomineralization, *Applied Surface Science* 612 (2023) 155800.
- [148] B. Subramanian, In vitro corrosion and biocompatibility screening of sputtered Ti₄₀Cu₃₆Pd₁₄Zr₁₀ thin film metallic glasses on steels, *Materials Science and Engineering: C* 47 (2015) 48-56.
- [149] S.T. Rajan, A. Bendavid, B. Subramanian, Cytocompatibility assessment of Ti-Nb-Zr-Si thin film metallic glasses with enhanced osteoblast differentiation for biomedical applications, *Colloids and Surfaces B: Biointerfaces* 173 (2019) 109-120.
- [150] B.-S. Lou, T.-Y. Lin, W.-T. Chen, J.-W. Lee, Corrosion property and biocompatibility evaluation of Fe-Zr-Nb thin film metallic glasses, *Thin Solid Films* 691 (2019) 137615.
- [151] J. Liu, Y. Fu, Y. Tang, X. Wang, Q. Cao, D. Zhang, J. Jiang, Thickness dependent structural evolution in Mg-Zn-Ca thin film metallic glasses, *Journal of Alloys and Compounds* 742 (2018) 524-535.
- [152] A. Brognara, J.P. Best, P. Djemia, D. Faurie, G. Dehm, M. Ghidelli, Effect of composition and nanostructure on the mechanical properties and thermal stability of Zr_{100-x}Cu_x thin film metallic glasses, *Materials & Design* 219 (2022).
- [153] M. Apreutesei, P. Djemia, L. Belliard, G. Abadias, C. Esnouf, A. Billard, P. Steyer, Structural-elastic relationships of Zr-TL (TL = Cu, Co, Ni) thin films metallic glasses, *Journal of Alloys and Compounds* 707 (2017) 126-131.
- [154] M. Ghidelli, S. Gravier, J.-J. Blandin, T. Pardoën, J.-P. Raskin, F. Mompiou, Compositional-induced structural change in Zr_xNi_{100-x} thin film metallic glasses, *Journal of Alloys and Compounds* 615 (2014) S348-S351.
- [155] A.B. Behboud, A. Motallebzadeh, S. Özerinç, Nanoheterogeneous ZrTa metallic glass thin films with high strength and toughness, *Journal of Alloys and Compounds* 901 (2022).

- [156] S. Achache, F. Sanchette, Effect of Tantalum Addition on Properties of Cu–Zr–Based Thin Film Metallic Glasses (TFMGs), *Coatings* 10(6) (2020).
- [157] N. Annonay, F. Challali, M.N. Labour, V. Bockelee, A. Garcia-Sanchez, F. Tetard, M.P. Besland, P. Djemia, F. Chaubet, Thin films of binary amorphous Zn-Zr alloys developed by magnetron co-sputtering for the production of degradable coronary stents: A preliminary study, *Bioact Mater* 3(4) (2018) 385-388.
- [158] N. Annonay, F. Challali, M.-N. Labour, V. Bockelée, A. Garcia-Sanchez, F. Tetard, M.-P. Besland, P. Djemia, F. Chaubet, Thin films of binary amorphous Zn-Zr alloys developed by magnetron co-sputtering for the production of degradable coronary stents: A preliminary study, *Bioactive materials* 3(4) (2018) 385.
- [159] K. Schlüter, C. Zamponi, N. Hort, K. Kainer, E. Quandt, Polycrystalline and amorphous MgZnCa thin films, *Corrosion science* 63 (2012) 234-238.
- [160] Y. Wang, K. Gao, X. Tao, W.-S. Ko, J. Wang, F. Chen, G. Xu, Y. Cui, Experimental investigation and thermodynamic description of Mg–Sc–Zn ternary system, *Calphad* 77 (2022) 102406.
- [161] Y. Ren, Y. Guo, D. Chen, S. Li, W. Pei, G. Qin, Isothermal section of Mg–Zn–Zr ternary system at 345 C, *Calphad* 35(3) (2011) 411-415.
- [162] H. Okamoto, Zn-Zr (zinc-zirconium), *Journal of Phase Equilibria and Diffusion* 28 (2007) 236-237.
- [163] H. Okamoto, Mg-Zr (magnesium-zirconium), *Journal of phase equilibria* 23(2) (2002) 198.
- [164] Z. Wang, K. Zeng, Y. Li, The correlation between glass formation and hardness of the amorphous phase, *Scripta Materialia* 65(9) (2011) 747-750.
- [165] M. Apreutesei, C. Esnouf, A. Billard, P. Steyer, Impact of local nanocrystallization on mechanical properties in the Zr-59 at.% Cu metallic glass thin film, *Materials & Design* 108 (2016) 8-12.
- [166] M. Apreutesei, P. Djemia, L. Belliard, G. Abadias, C. Esnouf, A. Billard, P. Steyer, Structural-elastic relationships of Zr-TL (TL= Cu, Co, Ni) thin films metallic glasses, *Journal of Alloys and Compounds* 707 (2017) 126-131.
- [167] M. Ghidelli, S. Gravier, J.-J. Blandin, P. Djemia, F. Momprou, G. Abadias, J.-P. Raskin, T. Pardoën, Extrinsic mechanical size effects in thin ZrNi metallic glass films, *Acta Materialia* 90 (2015) 232-241.
- [168] A. Rauf, Y. Fang, H. Zhang, G. Peng, T. Feng, Thickness effects on microstructure, mechanical and soft magnetic properties of sputtered FeZr thin film metallic glass, *Journal of Non-Crystalline Solids* 521 (2019) 119500.
- [169] A.B. Behboud, A. Motallebzadeh, S. Özeriç, Nanoheterogeneous ZrTa metallic glass thin films with high strength and toughness, *Journal of Alloys and Compounds* 901 (2022) 163578.

CHAPTER 2: MATERIALS AND METHODS

2.1 GFA evaluation and first-principles calculations

2.1.1 Thermodynamic evaluation of GFA

Thermodynamical calculations were conducted to investigate the glass forming ability (GFA) of ZnZr and ZnMg alloys. Specifically, the borders of the glass-forming compositional range (which is closely linked to the glass forming ability) of an alloy were defined based on the compositions at which the free energy of formation of amorphous phase (ΔG_{am}) becomes lower than that of the crystalline counterpart (ΔG_{ss}), as proposed by J. M. Lòpez *et al.* [1]. The free energy of mixing of a solid solution was calculated as

$$\Delta G_{ss} = \Delta H_{ss} - T\Delta S_{ss} \quad (1)$$

While, the amorphous one is defined as

$$\Delta G_{am} = \Delta H_{am} - T\Delta S_{am} \quad (2)$$

Where ΔH_{ss} , ΔH_{am} and ΔS_{ss} , ΔS_{am} are the enthalpies and entropies of mixing of the crystalline and amorphous phase, respectively and T is the temperature (298 K). The enthalpies of mixing, or enthalpies of formation, of amorphous and solid solution phases were evaluated as it has been suggested from Refs. [2, 3]. ΔH_{am} comprises two terms:

$$\Delta H_{am} = \Delta H_{chem} + \Delta H_m \quad (3)$$

Where ΔH_{chem} is the chemical contribution is given by the mixing enthalpies between the elements i and j ($\Delta H_{i,j}^{mix}$) which are tabulated in Ref. [4] averaged on the chemical fractions c_i and c_j .

$$\Delta H_{chem} = 4 \sum_{i=1, j \neq i}^n c_i c_j \Delta H_{i,j}^{mix} \quad (4)$$

The second enthalpy term considers the topological disorder. With the hypothesis that the enthalpy of the amorphous pure metals is the same as for the liquid pure metals [5], the difference in enthalpies between the amorphous and crystalline phases is given by:

$$\Delta H_m = T_m \Delta S_m \quad (5)$$

For reasons of simplicity, it is assumed that the melting entropy ΔS_m is constant for all metals. Furthermore, the enthalpy of the amorphous state is lower than for the liquid due to structural relaxation, and therefore it is convenient to replace ΔS_m with the smaller constant entropic term for liquids α ($3.5 \frac{J}{mol K}$) [3]. So, the formation enthalpy of the amorphous phase is:

$$\Delta H_{am} = 4 \sum_{i=1, j \neq i}^n c_i c_j \Delta H_{i,j}^{mix} + \alpha \sum_{i=1}^n c_i T_{m,i} \quad (6)$$

Where $T_{m,i}$ is the melting temperature of the i^{th} element.

For the estimation of the mixing enthalpy of solid solution ΔH_{ss} , three terms must be considered:

$$\Delta H_{ss} = \Delta H_{chem} + \Delta H_{elastic} + \Delta H_{structural} \quad (7)$$

The first term ΔH_{chem} is computed as for the amorphous phase since it is based on the same considerations and these values were tabulated in Ref. [4]. The elastic term $\Delta H_{elastic}$ is regarding the elastic energy and this is much larger than in the liquid or amorphous state. This contribution is not considered in amorphous phase because of the lack of periodicity, the atoms are not constrained to fit a certain volume [1]. It is calculated as below and it is also tabulated in Ref. [6].

$$\Delta H_{elast}^{i \text{ in } j} = \frac{2B_i G_j (V_j - V_i)^2}{3B_i V_j + 4G_j V_i} \quad (8)$$

Where G_j is the shear modulus of the matrix, B_i is the bulk modulus of the inclusion and V_j, V_i are the volumes of hole (atom in the matrix) and inclusion (atom as solute), respectively.

In this derivation, the change in volume due to charge transfer has been neglected completely and it is possible to evaluate this change by correcting the atomic volumes of the holes and the inclusion as in Ref. [7]. Finally, the elastic contribution results:

$$\Delta H_{elastic} = c_i c_j (c_j \Delta H_{elast}^{i \text{ in } j} + c_i \Delta H_{elast}^{j \text{ in } i}) \quad (9)$$

Finally, $\Delta H_{structural}$ is a structural contribution related to the difference in valence electrons and crystalline structure between solvent and solute. This contribution showed a minor effect compared to the size effect and it is often neglected [2]. In addition, in this study both solvent and solute have the same HCP crystalline structure and for these reasons $\Delta H_{structural}$ contribution will not be considered.

The values of entropy of mixing of both solid solution and amorphous phase involve a contribute coming from the configurational entropy, present in an ideal mixing

$$\Delta S^{conf} = -R \sum_{i=1}^n c_i \ln c_i \quad (10)$$

With R the gas constant and c_i is the molar fraction of the i th-element considered in the alloy. In the case of the amorphous phase, another contribute should be added in order to consider also the entropy of the liquid-like structure. This is done by adding a constant value α ($3.5 \frac{J}{mol K}$) [3]. So, the formation entropy of the solid solution and amorphous phases is:

$$\Delta S_{ss} = \Delta S^{conf} + \Delta S^{\delta} \quad (11)$$

$$\Delta S_{am} = \Delta S^{conf} + \alpha \quad (12)$$

Specifically, Mansoori *et al.* [8] proposed a thermodynamic parameter called mismatch entropy (ΔS^{δ}) to take into consideration the entropy caused by mixing elements with different atomic radii and it can be calculated with the solution of the Ornstein-Zernike integral equation in the Percus-Yevick hard sphere approximation [9] :

$$\Delta S^\delta = \left\{ \frac{3}{2} (\zeta^2 - 1) y_1 + \frac{3}{2} (\zeta - 1)^2 y_2 - \left[\frac{1}{2} (\zeta - 1)(\zeta - 3) + \ln \zeta \right] (1 - y_3) \right\} k_B \quad (13)$$

Where $\zeta = \frac{1}{1-PF}$ with PF the packing fraction (constant and equal to 0.64) and the dimensionless factors are:

$$y_1 = \frac{1}{\sigma^3} \sum_{i=1, j \neq i}^n c_i c_j (d_i + d_j)(d_i - d_j)^2 \quad (14)$$

$$y_2 = \frac{\sigma^2}{(\sigma^3)^2} \sum_{i=1, j \neq i}^n c_i c_j (d_i + d_j)(d_i - d_j)^2 \quad (15)$$

$$y_3 = \frac{(\sigma^2)^3}{(\sigma^3)^2} \quad (16)$$

And $\sigma^k = \sum_{i=1}^n c_i d_i^k$, with d_i the atomic diameter of the i^{th} element. ΔS^δ has a negligible effect on the calculation of the glass-forming compositional range, but it is often related to the packing efficiency of metallic glasses [10, 11], playing a crucial role on physical properties such as hardness and electrical resistivity [12].

This thermodynamical approach to evaluate the compositional range of amorphization of metallic alloys has been used in other studies showing a satisfactory agreement between predicted and experimental glass-forming compositional range values for binaries ZrNi, ZrCo and ZrCu alloys [1].

Finally,

Table 2.1 presents the list of input parameters utilized for estimating the glass-forming compositional range. These parameters include the shear modulus (G), bulk modulus (B), atomic volume (V), atomic diameter (d), melting temperature (T_{melt}), and enthalpy of mixing (ΔH_{mix}).

Table 2.1 List of input parameters to calculate the glass-forming compositional range.

| <i>Element</i> | <i>G (Pa)</i> | <i>B (Pa)</i> | <i>V (m³/mol)</i> | <i>d (pm)</i> | <i>T_{melt} (K)</i> | <i>ΔH_{mix} (kJ/mol)</i> |
|----------------|----------------------|----------------------|------------------------------|---------------|-----------------------------|----------------------------------|
| Zn | 4.7×10^{10} | 6.0×10^{10} | 9.2×10^{-6} | 266 | 692 | -29 |
| Zr | 3.7×10^{10} | 9.7×10^{10} | 1.4×10^{-5} | 315 | 2128 | |
| Zn | 4.7×10^{10} | 6.0×10^{10} | 9.2×10^{-6} | 266 | 692 | -4 |
| Mg | 1.6×10^{10} | 3.0×10^{10} | 1.4×10^{-5} | 309 | 923 | |
| Zr | 3.7×10^{10} | 9.7×10^{10} | 1.4×10^{-5} | 315 | 2128 | +6 |
| Mg | 1.6×10^{10} | 3.0×10^{10} | 1.4×10^{-5} | 309 | 923 | |

2.1.2 Special quasi-random structures for single crystalline random alloys

Total energies (E) and elastic constants (c_{ij}) were calculated using density functional theory as implemented in the VASP code [13]. The projector augmented wave method [14, 15] was used to describe the electronic wave functions, and the PBE [16] functional for the electronic exchange and correlation. The special quasi-random structures (SQS) [17] generated by the alloy theoretic automated toolkit program (ATAT) [18] were utilized to model random solid solutions. Supercells of $3 \times 3 \times 3$ times the conventional HCP unit cell were employed. The k -point grid $9 \times 9 \times 3$ was used for the integration of electronic states in the Brillouin zone in all supercells. The energy cutoff of 500 eV was employed for the plane wave basis. The electronic energy convergence criterion was set to 10^{-5} eV/cell. Geometry optimizations in this work were performed using the conjugate gradient algorithm, with a stopping criterion of all the forces smaller than 0.01 eV/Å.

The whole set of single elastic constants were calculated using the stress-strain method by the Hooke law $\sigma = c \varepsilon$, the stress was calculated as $\sigma = E/V$ where V is the volume of the strained cell and the deformation matrices ε are listed as following, with ε equals to 0.005 in our calculations.

$$\begin{pmatrix} \varepsilon_1 & \varepsilon_6 & \varepsilon_5 \\ \varepsilon_6 & \varepsilon_2 & \varepsilon_4 \\ \varepsilon_5 & \varepsilon_4 & \varepsilon_3 \end{pmatrix} = \begin{pmatrix} \pm\varepsilon & \frac{1}{2}\varepsilon & 0 \\ \frac{1}{2}\varepsilon & 0 & 0 \\ 0 & 0 & 0 \end{pmatrix}, \begin{pmatrix} 0 & \frac{1}{2}\varepsilon & 0 \\ \frac{1}{2}\varepsilon & \pm\varepsilon & 0 \\ 0 & 0 & 0 \end{pmatrix}, \begin{pmatrix} 0 & \frac{1}{2}\varepsilon & 0 \\ \frac{1}{2}\varepsilon & 0 & 0 \\ 0 & 0 & \pm\varepsilon \end{pmatrix} \\
\begin{pmatrix} 0 & \frac{1}{2}\varepsilon & \frac{1}{2}\varepsilon \\ \frac{1}{2}\varepsilon & 0 & 0 \\ \frac{1}{2}\varepsilon & 0 & 0 \end{pmatrix}, \begin{pmatrix} 0 & \frac{1}{2}\varepsilon & -\frac{1}{2}\varepsilon \\ \frac{1}{2}\varepsilon & 0 & 0 \\ -\frac{1}{2}\varepsilon & 0 & 0 \end{pmatrix}, \begin{pmatrix} 0 & \frac{1}{2}\varepsilon & 0 \\ \frac{1}{2}\varepsilon & 0 & \frac{1}{2}\varepsilon \\ 0 & \frac{1}{2}\varepsilon & 0 \end{pmatrix} \\
\begin{pmatrix} 0 & \frac{1}{2}\varepsilon & 0 \\ \frac{1}{2}\varepsilon & 0 & -\frac{1}{2}\varepsilon \\ 0 & -\frac{1}{2}\varepsilon & 0 \end{pmatrix}, \begin{pmatrix} 0 & \varepsilon & 0 \\ \varepsilon & 0 & 0 \\ 0 & 0 & 0 \end{pmatrix}, \begin{pmatrix} 0 & 0 & 0 \\ 0 & 0 & 0 \\ 0 & 0 & 0 \end{pmatrix}$$

The five independent ones (c_{11} , c_{12} , c_{13} , c_{33} , c_{44}) for the HCP phase were then obtained from the average on relevant elastic tensor components [19]. The two averaged polycrystalline elastic constants C_{11} and C_{44} , were calculated by the Voigt-Reuss-Hill averages [20].

2.1.3 Ab initio molecular dynamics to design amorphous materials

AIMD simulations by the VASP code [21] were employed to design glassy solid solutions, aiming to examine the local atomic arrangement in relation to composition and its impact on structural and mechanical properties. A cutoff energy of 350 eV for the plane-wave basis set was selected to balance both speed and accuracy for all the computationally intensive AIMD calculations. A cubic box with periodic boundary conditions was used, containing 256 atoms of the desired alloy. Initially, all alloys were heated to 2500 K and equilibrated for a minimum of 11 picoseconds (ps) under isobaric-isothermal (NPT) ensemble, ensuring the attainment of a homogeneous molten alloy with relaxed atomic positions. Subsequently, a rapid quenching process was employed to lower the system temperature from 2500 K to 300 K with a cooling rate of 733×10^{13} K/s (using a time step of 0.3×10^{-15} s and 1000 steps). We tried several cooling time like Houska *et al.* [22] on ZrSiN who indicated that the cooling

duration should not be less than 2 picoseconds to generate structures that are unaffected by the cooling rate, because of the presence of a light element (N) that is not our case. The quenched alloys were then relaxed at 300 K (time > 11 ps) using the NPT ensemble to determine the atomic volume and mass density. An example of simulated structure cell and its reduced PDF $g(r)$ is represented and compared with experimental measure obtained using synchrotron source X-ray scattering at SOLEIL in **Fig. 2.1** for amorphous $Zr_{50}Cu_{50}$ (DIFFABS line managed by D. Thiaudière, beamtime from 13th to 20th Nov. 2023) using an energy of 18 keV) .

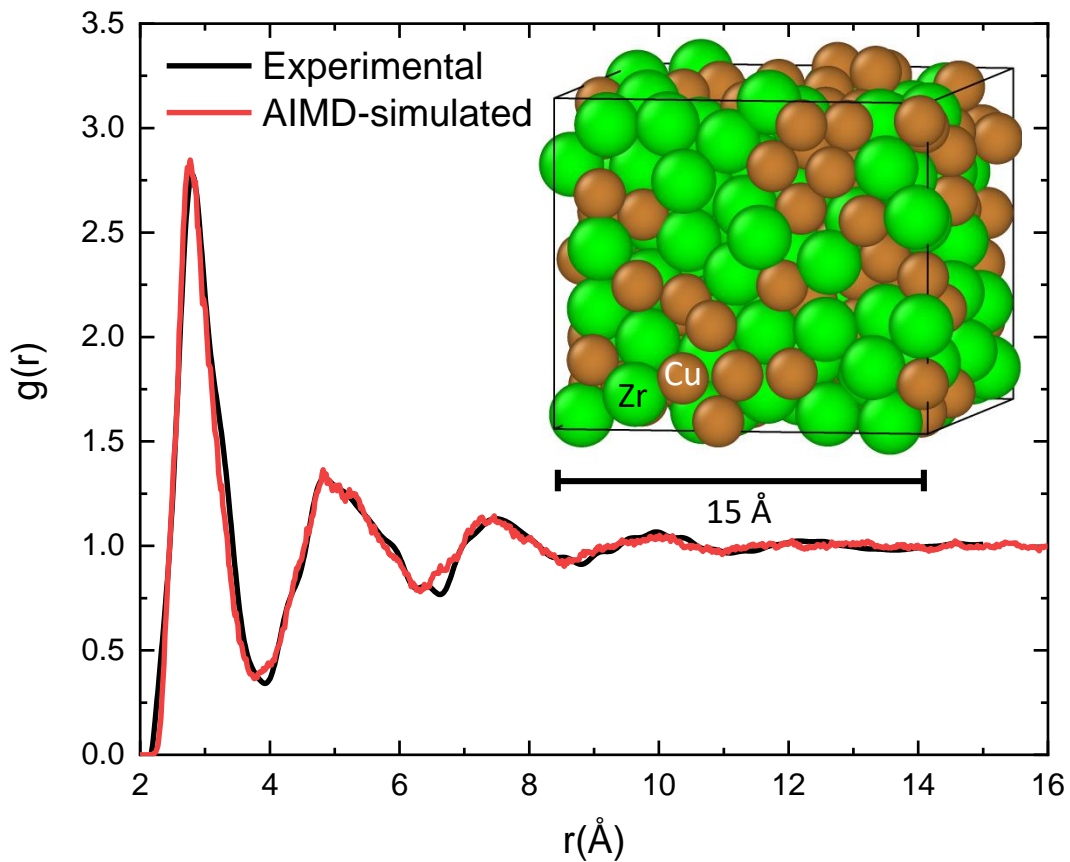


Fig. 2.1 Comparison of reduced PDFs $g(r)$ obtained by AIMD and experimental measures. The insert represents the simulated amorphous cell containing 256 atoms (128 Zr and 128 Cu).

To obtain elastic constants C_{ij} with the same accuracy as for the HCP solid solutions, we then optimized the as-obtained amorphous structures at 0 K using the same algorithm and parameters as previously described for the crystalline phase, and calculating their

elastic constants considering both relaxed and unrelaxed atomic positions after each applied strain. The amorphous structure of a glassy material can be described with the packing of several Voronoi clusters and their population gives some insight on the mechanical properties of the material. The Voronoi tessellation method, implemented through the OVITO software package [23], was employed to analyze the last thousand-time steps of the quenched alloys. In this analysis, each polyhedral cell was assigned five indices $\langle n_3 n_4 n_5 n_6 n_7 \rangle$, where n_i represents the number of faces with i -edges in each Voronoi cell. Of particular interest were icosahedral structures denoted by the Voronoi index $\langle 0 0 12 0 0 \rangle$, with the cluster-central atom coordination number (Σn_i) [24]. **Fig. 2.2** shows an example of the coordination (i.e. Σn_i) of MoNi and MoSi amorphous alloys. Despite the coordination of MoNi remains nearly constant close to 14, MoSi shows a transition from 14 to lower coordination when Si content is larger than 70 at.% and this transition is also reflected to the mechanical properties of the material caused by the formation of more covalent atomic bonds [25].

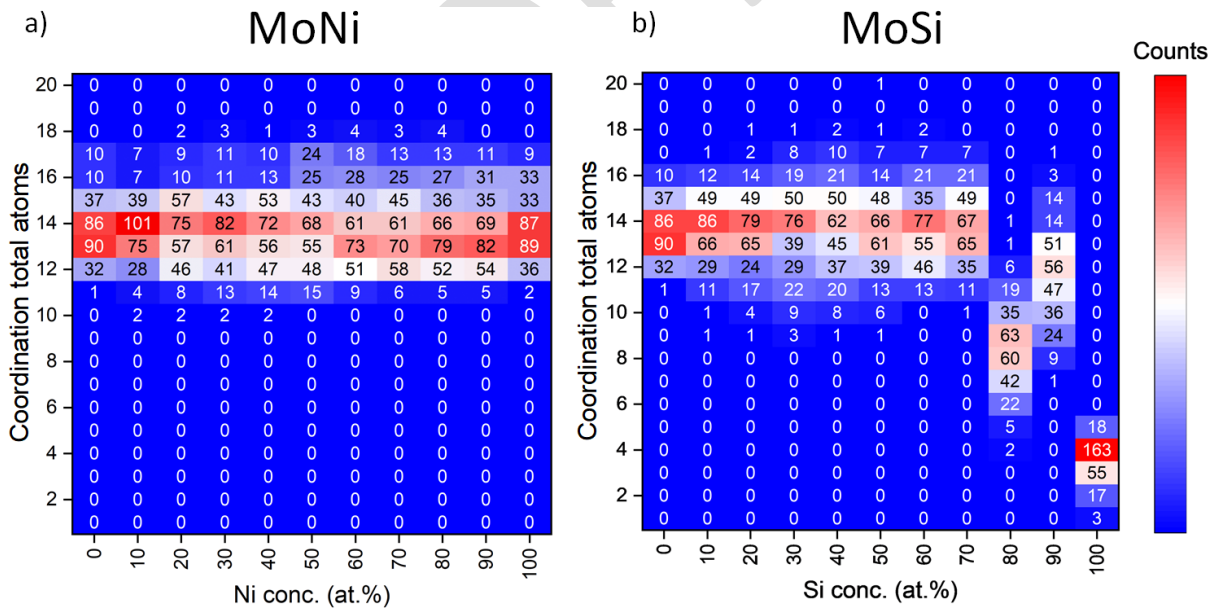


Fig. 2.2 Clusters coordination analysis for amorphous a) $\text{Mo}_{100-x}\text{Ni}_x$, and b) $\text{Mo}_{1-x}\text{Si}_x$ alloys.

In addition, **Fig. 2.3** illustrates the topological structure and the associated Voronoi cells of the most common Voronoi clusters [26].

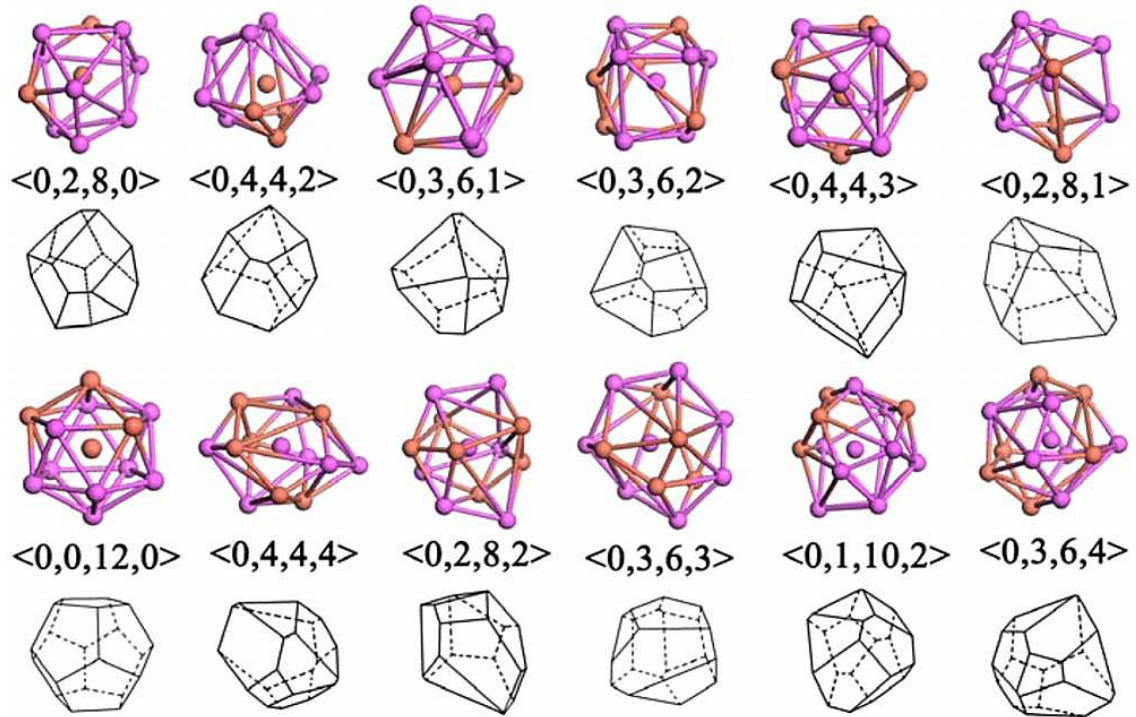
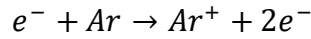


Fig. 2.3 Representative topologic structures of the most frequent clusters as well as their Voronoi cells [26].

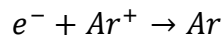
2.2 Thin films elaboration by magnetron sputtering

In Physical Vapor Deposition (PVD) processes, deposition species are either thermally evaporated or sputtered from a source (solid target) under ion bombardment. Sputter deposition has been recognized for decades as a flexible, reliable, and effective method. In sputtering and other plasma-based PVD processes, porosity can be controlled by tuning the energy of deposited particles through an external electric field.

In PVD plasmas, electron energies are typically on the order of a few electron volts (e.g., 2 eV), corresponding to 23000 K ($E=k_B T$). Due to the small fraction of electrons, the chamber walls do not appreciably heat. To initiate plasma, a source of electrons is needed. By applying a low negative voltage to an electrode, spontaneous emission of electrons occurs. These electrons are accelerated, and ions may be produced by collision with inert gases, such as argon. Free electrons in a vacuum can also be used for ionization



One electron is accelerated by the electric field and collides with a gas atom, producing an ion and two electrons. In this event, a new free electron is created, leading to another collisional event. In principle, this is a self-sustained reaction. There are also termination events where electrons can be collected from the anodes and all grounded surfaces inside the system. Additionally, ions are involved in neutralization reactions:



Conventional planar direct current magnetron sputtering commonly operates using Ar as the working gas at pressures of a few Pa and an applied cathode voltage of hundreds of Volts. The confining magnetic field strength at the target surface is in the range of 20 – 50 mT. This leads to current densities of the order of 4 – 60 mA/cm² and power densities of several tens of W/cm². If a proper balance between collisions is achieved, a steady-state condition is established. An electric field is employed to accelerate electrons, imparting them with high energy.

Ions, electrons, and molecules move randomly and can be collected by the workpiece. Consequently, its surface accumulates a current density (J), determined by the electrical charge (q_i) multiplied by the flux of these species:

$$J_i = \frac{q_i n_i v_i}{4} \quad (17)$$

where n_i is the concentration of the species, and v_i is their mean velocity.

The mean velocity derived from the Maxwell-Boltzmann distribution is given by:

$$v_i = \sqrt{\frac{8K_B T}{\pi m_i}} \quad (18)$$

Furthermore, the ratio of electronic current density (J_{el}) to ionic current density (J_{ion}) is expressed as:

$$\frac{J_{el}}{J_{ion}} = \frac{q_{el}n_{el}}{q_{ion}n_{ion}} \left(\frac{T_{el}m_{ion}}{T_{ion}m_{el}} \right)^{1/2} \quad (19)$$

Since the ionic current density is significantly lower than the electronic one, a negative charge will accumulate at one surface, accelerating ions. A delicate balance between these two current densities must be maintained: the electronic flow slows down, while the ion flow is accelerated, ultimately reaching the steady-state condition.

When ions from the plasma bombard the target (cathode), they not only release secondary electrons but also atoms of the cathode material through a process known as sputtering. The enhanced ionization, facilitated by confining the charged species using a magnetic field, enables operation at significantly lower working gas pressures (0.1 to 1.5 Pa). The purpose of magnetic fields in a magnetron sputtering system is to prolong the lifetime of electrons by trapping them in the proximity of the cathode, thereby increasing the likelihood of collision events (refer to **Fig. 2.4**).

Within the magnetic field, charged species are also subject to the electric force arising from the potential difference. Thus, any charge will experience a Lorentz force, expressed as:

$$\mathbf{F} = -q(\mathbf{E} + \mathbf{v} \times \mathbf{B}) \quad (20)$$

Due to magnetic forces, electrons undergo a helicoidal trajectory near the target. This configuration is advantageous because the confinement of electrons near the target significantly enhances the erosion rate.

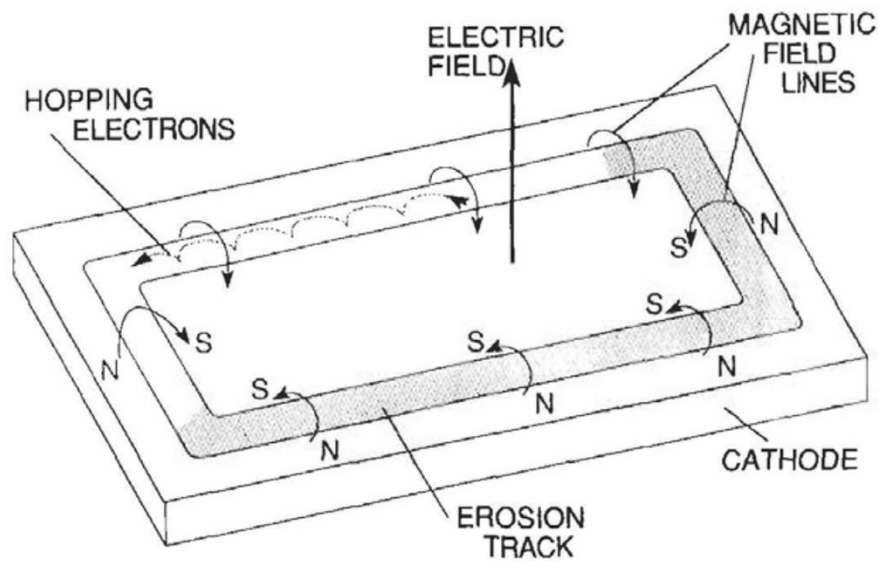


Fig. 2.4 Representation of the surface of the magnetron target indicating the electric and magnetic fields as well as electron trajectory.

The depositions were carried out in clean-room environment and a photo of the magnetron sputtering facility is illustrated in **Fig. 2.5**.

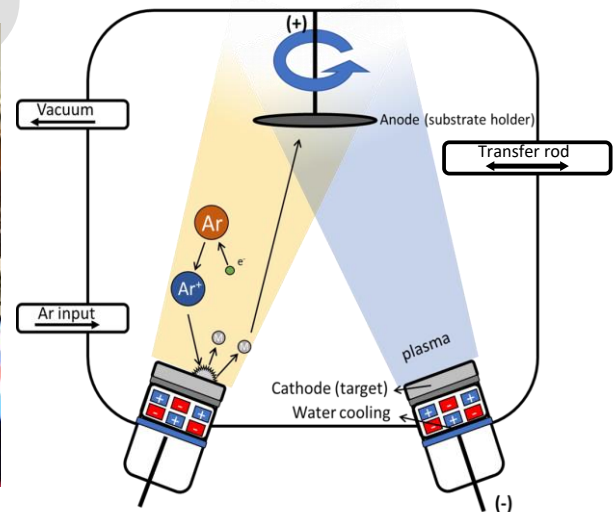


Fig. 2.5 Photo (left) and representative scheme (right) of magnetron sputtering facility in clean-room environment at Sorbonne Paris Nord University.

In this work, all binary and ternary alloys with different chemical compositions were deposited on Silicon (100) and Kapton® substrates by RF and/or DC magnetron co-

sputtering from pure metallic targets: Zn, Zr and Mg at room temperature. The target-substrate distance was fixed at 9 cm. Prior to deposition, the Kapton® substrates were ultrasonically cleaned in acetone, ethanol and deionized water, and then dried in blowing nitrogen, respectively. The deposition chamber was initially evacuated to a base pressure of about 2×10^{-5} Pa. Thanks to a regulation valve; the working pressure in the chamber, was fixed at 0.5 Pa with argon flow rate of 40 sccm (purity: 99.999 %) regulated by a mass flow controller during deposition processes. The atomic percentage of the different elements in binaries and ternaries alloys was varied by adjusting the powers applied to the different targets. The rotation speed of the substrate holder was set at 10 RPM to ensure uniform deposits on 2-inch surface samples. The main parameters used to make the different binary alloys are summarized in **Table 2.2**.

Table 2.2 List of the magnetron sputtering deposition parameters employed for the fabrication of the thin films.

| <i>Parameters</i> | <i>Range/values</i> |
|----------------------------|----------------------------|
| Targets | Zn, Mg et Zr |
| Substrates | Si and Kapton® |
| Base pressure | $\sim 2 \times 10^{-5}$ Pa |
| Working pressure | 0.5 Pa |
| Ar flow rate | 40 sccm |
| Power supply | RF and DC |
| Sputtering powers | 50 to 300 W |
| Substrates-target distance | ~ 9 cm |
| Substrate rotation speed | 10 RPM |
| Deposition temperature | Room temperature |

2.3 Structural characterization (SEM/EDX and XRD)

A field emission Scanning Electron Microscopy (SEM-FEG) ZEISS Supra 40VP was used to acquire the surface and cross-sectional images, visualizing the deposited

morphology and measuring the thickness of as-deposited thin films. To ensure the accuracy of our film thickness measurements, the growing rate of the films was calibrated using an *in situ* quartz crystal microbalance and additionally, systematical profilometer measurements were performed immediately after the film deposition. The chemical composition was measured by Energy Dispersive x-ray Spectroscopy (EDX) with a Bruker XFlash 4010. X-ray Diffraction Inel EQUINOX 1000 diffractometer was used to analyze the crystalline/amorphous structures of the deposited alloys. The instrument was equipped with a curved detector and Co-K_{α1} radiation ($\lambda = 1.789010 \text{ \AA}$) and the angle of incidence of the radiation was 2° to avoid silicon contribution. The acquisition time of each spectrum took one-night of accumulation.

2.4 Mechanical characterization

2.4.1 Nanoindentation

Young's modulus (E) and hardness (H) were determined as a function of indentation depth through nanoindentation tests conducted using an MTS Nanoindenter (Oak Ridge, TN, USA). The continuous stiffness measurement (CSM) method [27] was employed, where the sample was subjected to small oscillations with a frequency of 45 Hz and an amplitude of 2 nm. Indentations were performed with a diamond-type Berkovich indenter mounted on an XP head, assuming a Poisson ratio of $\nu = 0.35$ (consistently with BLS measurements findings) and the constant strain rate of 0.05 s^{-1} . Prior to and after the measurements, tip and frame stiffness calibrations were performed using standard fused silica. Three typical load-displacement curves for ZrCuAl_x TFMGs are represented in **Fig. 2.6**.

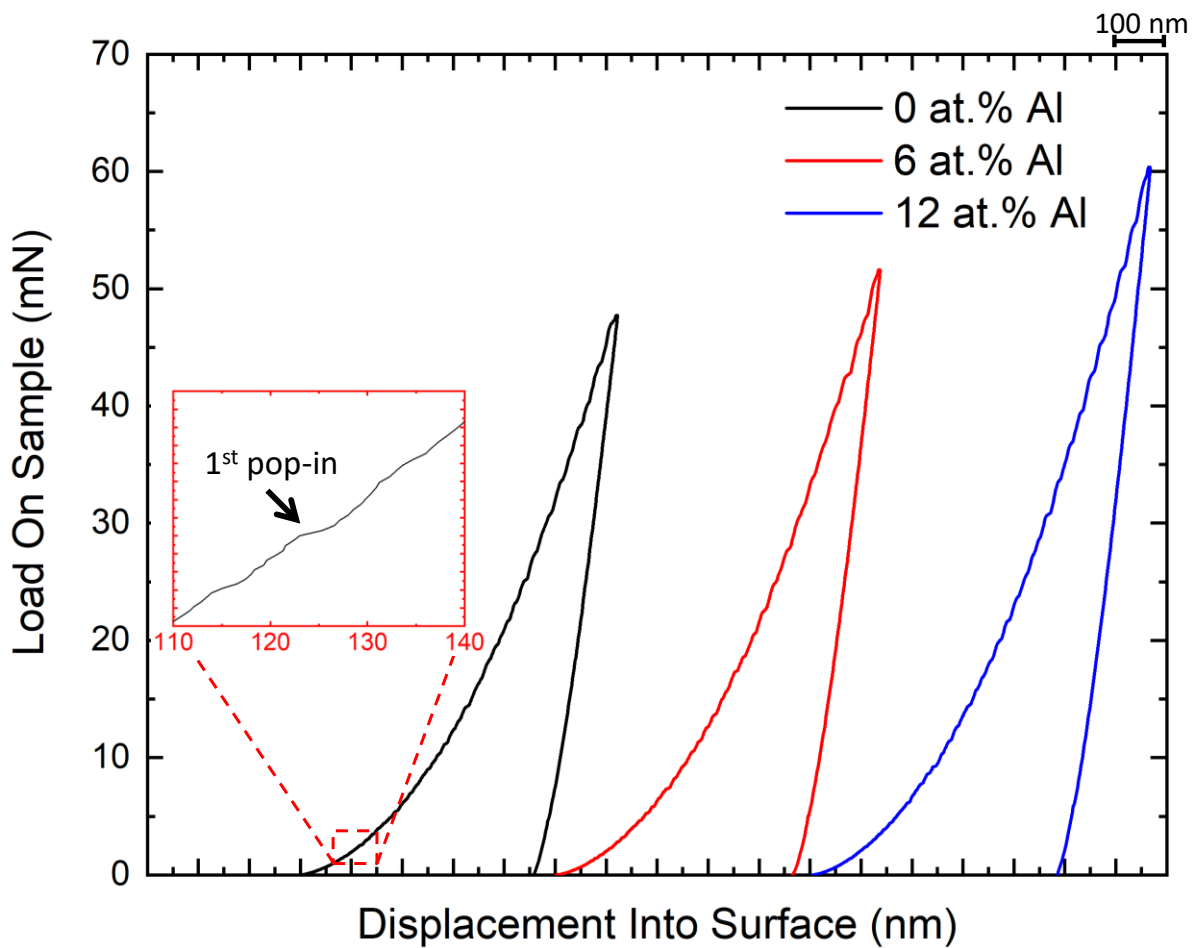


Fig. 2.6 Nanoindentation load displacement curves for ZrCuAl_x TFMs (refer to **Annex**) [28]. The insert represents the first pop-in effect observed in the curves around 100 nm of displacement.

A minimum of 20 indentations were conducted on each sample, and E and H values were extracted at indentation depths of approximately 10% of the film thickness, following the Oliver and Pharr methodology [29]. The resulting E and H in functions of the displacement are illustrated in **Fig. 2.7** showing the increase of mechanical properties with the addition of Al.

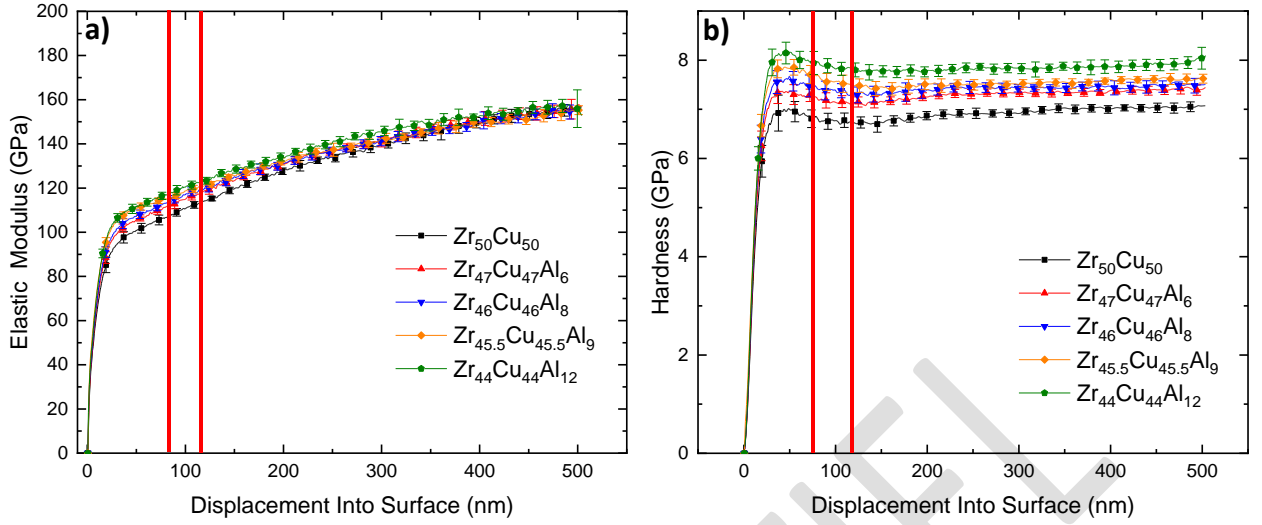


Fig. 2.7 a) Elastic modulus and b) hardness as function of the displacement of $ZrCuAl_x$ TFMGs (refer to **Annex**) [28]. The red lines highlight the range to measure the values of E and H .

2.4.2 Brillouin light scattering

BLS spectra were acquired in air at room temperature with an incidence angle of 65° during 20 minutes at 100 mW of a p-polarized incident light (wavelength $\lambda = 532$ nm). The technique allows the extraction of both Rayleigh and Sezawa surface waves sound velocities. For thick enough films (i.e. > 300 nm), the Rayleigh surface wave sound velocity (V_R) is closely related to the shear sound velocity (V_S), hence shear modulus $G = C_{44} = \rho(V_S)^2$ by knowing the mass density of the film (ρ). Under the hypothesis of isotropy of the material (which is perfectly correct in case of metallic glasses and non-textured polycrystalline materials), C_{11} is directly related to C_{12} and C_{44} through the relation $C_{11} = 2C_{44} + C_{12}$, and it is measured by simulating the whole BLS spectra with the frequency positions of additional Sezawa modes. The experimental details regarding the measurements of elastic C_{11} and C_{44} constants are reported in Ref. [30]. The Young's modulus (E) and the Poisson's ratio (ν) are calculated with the following equations:

$$E = \frac{C_{44}(3C_{11} - 4C_{44})}{(C_{11} - C_{44})} \quad (21)$$

and

$$v = \frac{(C_{11} - 2C_{44})}{(C_{11} - C_{44})} \quad (22)$$

Two examples of BLS spectra are displayed in **Fig. 2.8** showing the presence of Rayleigh peaks labelled with R and, in case of the thin film, Sezawa peaks labelled with S_i . For thick samples, the frequency at the end of the “tail” labelled with LT is related to the longitudinal velocity.

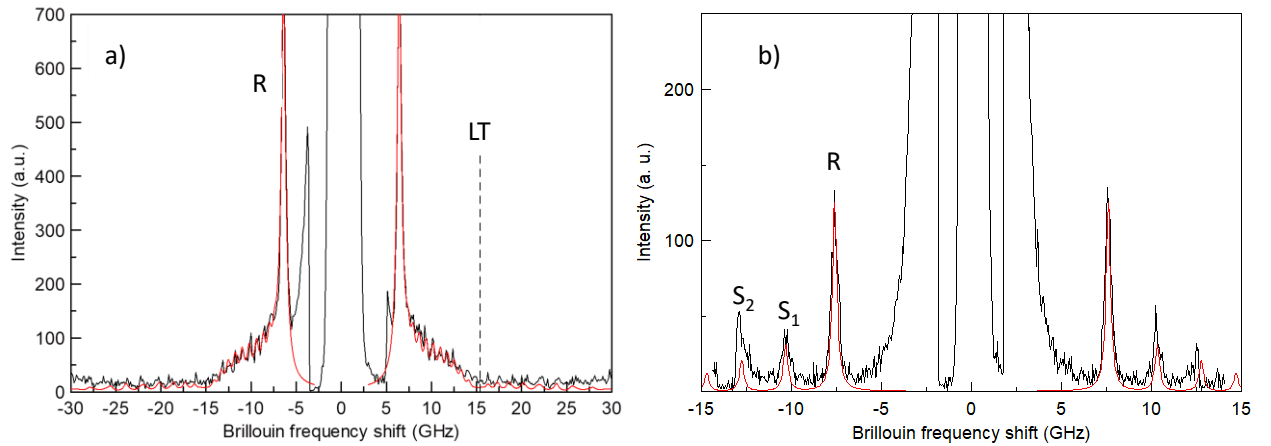


Fig. 2.8 Typical BLS spectra for a) thick (3 μm) ZrCu and thin (300 nm) pure Zr films.

2.4.3 Tensile test on Kapton® substrate

Tensile tests were conducted on films that were deposited onto flexible Kapton® substrates (4 cm \times 0.5 cm), which had a thickness of 125 μm . The testing was carried out using a Deben tensile machine with a capacity of 300 N, coupled with a Keyence confocal microscope [31]. The films were subjected to a tensile speed of 0.5 mm/min, while the sample gage length was set at 40 mm, resulting in a strain rate of approximately $2.1 \times 10^{-4} \text{ s}^{-1}$. To monitor the evolution of crack density relative to the applied strain, a 10x objective was utilized. The linear crack density was determined by quantitatively estimating the number of cracks perpendicular to the loading direction over the length of the sample observed through the microscope objective, which corresponded to a distance of 1050 μm .

2.5 Static immersion test

To evaluate the corrosion behavior of Mg-Zr thin films, static immersion tests have been performed in SBF at 37 °C which chemical composition is listed in **Table 2.3** [32]. The samples with an exposed area of 0.25 cm² have been immersed in 4 ml SBF for different periods of immersion (1 and 8 weeks) in static conditions and prior SEM analysis, the samples have been rinsed with deionized water and they have been dried in atmosphere at 60 °C.

Table 2.3 Chemical composition for 1L solution of SBF [32]

| <i>Reagent</i> | | | | | | | | |
|----------------|--------------------|---------|---------------------------------|--------------------------------------|---------|-------------------|---------------------------------|---------|
| NaCl | NaHCO ₃ | KCl | KH ₂ PO ₄ | MgCl ₂ ·6H ₂ O | HCl 1 M | CaCl ₂ | Na ₂ SO ₄ | Tris |
| 7.996 g | 0.350 g | 0.224 g | 0.228 g | 0.305 g | 40 mL | 0.278 g | 0.071 g | 6.117 g |

2.6 References

- [1] J.M. Lopez, J.A. Alonso, L.J. Gallego, Determination of the glass-forming concentration range in binary alloys from a semiempirical theory: Application to Zr-based alloys, *Phys Rev B Condens Matter* 36(7) (1987) 3716-3722.
- [2] P. Loeff, A. Weeber, A. Miedema, Diagrams of formation enthalpies of amorphous alloys in comparison with the crystalline solid solution, *Journal of the Less common Metals* 140 (1988) 299-305.
- [3] G. Van der Kolk, A. Miedema, A. Niessen, On the composition range of amorphous binary transition metal alloys, *Journal of the Less Common Metals* 145 (1988) 1-17.
- [4] A. Takeuchi, A. Inoue, Classification of bulk metallic glasses by atomic size difference, heat of mixing and period of constituent elements and its application to characterization of the main alloying element, *Materials transactions* 46(12) (2005) 2817-2829.
- [5] J. Somoza, L. Gallego, C. Rey, S. Rozenberg, B. Arcondo, H. Sirkin, R. De Tandler, J. Kovacs, J. Alonso, An experimental and theoretical study of the glass-forming region of the Mg-Cu-Sn system, *Journal of Materials Science* 30 (1995) 40-46.
- [6] A. Niessen, A. Miedema, F. De Boer, R. Boom, Enthalpies of formation of liquid and solid binary alloys based on 3d metals: IV. Alloys of cobalt, *Physica B+ C* 151(3) (1988) 401-432.
- [7] A. Miedema, A. Niessen, Volume effects upon alloying of two transition metals, *Physica B+ C* 114(3) (1982) 367-374.
- [8] G.A. Mansoori, N.F. Carnahan, K.E. Starling, T.W. Leland, Equilibrium Thermodynamic Properties of the Mixture of Hard Spheres, *The Journal of Chemical Physics* 54(4) (1971) 1523-1525.
- [9] J.L. Lebowitz, Exact Solution of Generalized Percus-Yevick Equation for a Mixture of Hard Spheres, *Physical Review* 133(4A) (1964) A895-A899.
- [10] K.-W. Park, J.-i. Jang, M. Wakeda, Y. Shibutani, J.-C. Lee, Atomic packing density and its influence on the properties of Cu-Zr amorphous alloys, *Scripta Materialia* 57(9) (2007) 805-808.
- [11] H.L. Peng, M.Z. Li, W.H. Wang, C.Z. Wang, K.M. Ho, Effect of local structures and atomic packing on glass forming ability in Cu_xZr_{100-x} metallic glasses, *Applied Physics Letters* 96(2) (2010).
- [12] B. Braeckman, Sputter deposition of complex alloy thin films, Ghent University, 2016.
- [13] J. Hafner, Ab-initio simulations of materials using VASP: Density-functional theory and beyond, *Journal of computational chemistry* 29(13) (2008) 2044-2078.
- [14] P.E. Blöchl, Projector augmented-wave method, *Physical Review B* 50(24) (1994) 17953-17979.

- [15] G. Kresse, D. Joubert, From ultrasoft pseudopotentials to the projector augmented-wave method, *Physical Review B* 59(3) (1999) 1758-1775.
- [16] J.P. Perdew, K. Burke, M. Ernzerhof, Generalized Gradient Approximation Made Simple, *Phys. Rev. Lett.* 77(18) (1996) 3865-3868.
- [17] S. Wei, L.G. Ferreira, J.E. Bernard, A. Zunger, Electronic properties of random alloys: Special quasirandom structures, *Phys Rev B Condens Matter* 42(15) (1990) 9622-9649.
- [18] A. van de Walle, P. Tiwary, M. de Jong, D.L. Olmsted, M. Asta, A. Dick, D. Shin, Y. Wang, L.Q. Chen, Z.K. Liu, Efficient stochastic generation of special quasirandom structures, *Calphad* 42 (2013) 13-18.
- [19] M. Moakher, A.N. Norris, The Closest Elastic Tensor of Arbitrary Symmetry to an Elasticity Tensor of Lower Symmetry, *Journal of Elasticity* 85(3) (2006) 215-263.
- [20] R. Hill, The elastic behaviour of a crystalline aggregate, *Proceedings of the Physical Society. Section A* 65(5) (1952) 349.
- [21] G. Kresse, J. Furthmüller, Efficient iterative schemes for ab initio total-energy calculations using a plane-wave basis set, *Physical Review B* 54(16) (1996) 11169.
- [22] J. Houska, S. Kos, Ab initio modeling of complex amorphous transition-metal-based ceramics, *Journal of Physics: Condensed Matter* 23(2) (2010) 025502.
- [23] A. Stukowski, Visualization and analysis of atomistic simulation data with OVITO—the Open Visualization Tool, *Modelling and Simulation in Materials Science and Engineering* 18(1) (2010) 015012.
- [24] G. Guo, Quasi-Icosahedral Clusters in Zr-Based Metallic Glasses, *Metals* 10(9) (2020) 1135.
- [25] C.H. Li, C. Poltronieri, G. Abadias, P. Djemia, Computational approach to identify structural and elastic relationship in metastable crystalline and amorphous alloy thin films: Mo_{1-x}Ni_x and Mo_{1-x}Si_x case studies, *Surface and Coatings Technology* (2023) 130168.
- [26] S. Wang, M. Kramer, M. Xu, S. Wu, S. Hao, D. Sordelet, K. Ho, C. Wang, Experimental and ab initio molecular dynamics simulation studies of liquid Al₆₀Cu₄₀ alloy, *Physical Review B* 79(14) (2009) 144205.
- [27] X. Li, B. Bhushan, A review of nanoindentation continuous stiffness measurement technique and its applications, *Materials characterization* 48(1) (2002) 11-36.
- [28] C. Poltronieri, A. Brognara, F. Bignoli, S. Evertz, P. Djemia, D. Faurie, F. Challali, C. Li, L. Belliard, G. Dehm, Mechanical properties and thermal stability of ZrCuAl_x thin film metallic glasses: Experiments and first-principle calculations, *Acta Materialia* 258 (2023) 119226.
- [29] W.C. Oliver, G.M. Pharr, An improved technique for determining hardness and elastic modulus using load and displacement sensing indentation experiments, *Journal of Materials Research* 7(6) (2011) 1564-1583.

- [30] M. Apreutesei, P. Djemia, L. Belliard, G. Abadias, C. Esnouf, A. Billard, P. Steyer, Structural-elastic relationships of Zr-TL (TL= Cu, Co, Ni) thin films metallic glasses, *Journal of Alloys and Compounds* 707 (2017) 126-131.
- [31] C.H. Li, R. Dedoncker, L.W. Li, F. Sedghgooya, F. Zighem, V. Ji, D. Depla, P. Djemia, D. Faurie, Mechanical properties of CoCrCuFeNi multi-principal element alloy thin films on Kapton substrates, *Surface and Coatings Technology* 402 (2020) 126474.
- [32] T. Kokubo, H. Takadama, How useful is SBF in predicting in vivo bone bioactivity?, *Biomaterials* 27(15) (2006) 2907-2915.

CHAPTER 3: NANOCRYSTALLINE AND AMORPHOUS BINARY ALLOYS

As crystalline alloys and composite materials are susceptible to localized corrosion and pitting phenomena, the ongoing challenge remains the development of materials with consistent and controllable corrosion rates. A promising solution to address this challenge lies in the use of TFMGs, which are garnering increasing attention due to their disordered atomic structure, imparting them with unique mechanical properties. Furthermore, the homogeneous and isotropic atomic structure characteristic of TFMGs holds the potential to lead to a more uniform and tunable corrosion behavior, contingent on the alloy composition. Another notable advantage of TFMGs lies in their fabrication techniques, such as PVD, which are able to rapidly explore a wide range of alloy compositions through combinatorial screening. Despite these promising aspects, delving into the intricate relationships between chemical composition, atomic structure, and mechanical properties in the context of TFMGs remains a relatively uncharted territory, posing an enduring challenge to materials scientists.

As discussed in **Chapter 1: State-of-the-art**, specifically in Section **1.1.2**, the utilization of certain elements such as Mg, Zn and Fe holds paramount significance in the realm of biodegradable material development. Notably, among these elements, Fe exhibits a positive ΔH^{mix} when combined with Mg (18 kJ/mol) and Zn (4 kJ/mol). This thermodynamic aspect results in a limited glass-forming ability for Fe-Zn or Fe-Mg alloys in this context. Consequently, there arises a necessity to explore alternative strategies to enhance the amorphous phase formation capabilities of these alloys. One effective approach to broaden the compositional range of amorphous alloys involves the incorporation of Zr as a glass-former element. Zr has been strategically employed to augment the amorphization potential of ZnZr and ZnMgZr, while reducing the crystal size of Mg-Zr binary alloys, circumventing the constraints imposed less

favorable enthalpy of mixing of Fe. By introducing Zr into the alloy composition, we can effectively manipulate the atomic structure and crystalline properties, thus opening up new avenues for the development of biodegradable materials with improved characteristics.

In this chapter, we embark on a comprehensive exploration of the synthesis, structural characteristics, and mechanical properties of nanocrystalline and amorphous binary alloys: ZrMg, ZnMg and ZnZr. The chapter is divided in two parts: the first one will present the results and discussion of nanocrystalline MgZr films. Successively, the other two systems (ZnMg and ZnZr) will be introduced focusing on the glassy compositions, with a particular emphasis on identifying their GFA. Moreover, we aim to establish a robust correlation between the amorphous structures present in these alloys and their resulting mechanical properties. This endeavor is further augmented by employing advanced first-principles calculations, specifically *ab initio* molecular dynamics and special quasi-random structures coupled with density functional theory. By delving into these aspects, we endeavor to shed light on this previously uncharted territory, uncovering critical insights that contribute to our understanding of Zn-based TFMGs and their potential applications. The overarching objective of this chapter is to delve into a comprehensive analysis of the atomic structure and physical properties of these binary materials. This preliminary study serves as a crucial foundation for our subsequent exploration of ternary alloys, specifically focusing on the Zn-Mg-Zr system. Through this progressive investigation, we aim to gain deeper insights into the intricate interplay of elements and their impact on material properties, ultimately paving the way for the design and development of advanced biodegradable alloys.

3.1 Nanocrystalline MgZr

3.1.1 Deposition process

The deposition of thin films was accomplished through magnetron sputtering, a process that is comprehensively described in Section 2.2 of this work. In this context, **Table 3.1** provides an overview of the target powers employed during the deposition process, as well as the resultant chemical composition and thickness of the deposited films.

Table 3.1 Deposition parameters, chemical composition and thickness measured by SEM imaging of the film cross-section.

| P_{Zr} (W) | P_{Mg} (W) | P_{Zr}/P_{Mg} | Conc. (at.%) | Thickness (± 10 nm) |
|--------------|--------------|-----------------|-------------------------------|--------------------------|
| 50-250 | 50-200 | 0.25-5 | Mg: 11 to 88 and Zr: 12 to 87 | 590-900 |

The positive enthalpy of mixing observed in Mg-Zr alloys (+6 kJ/mol), coupled with the absence of any intermetallic phases within the phase diagram (see **Fig. 3.1**) [1], highlights the limited solubility of Zr within the Mg matrix and *vice versa*. These characteristics are indicative of a weak GFA in this alloy system. In fact, the formation of distinct Mg and Zr phases is favorable, with little tendency for these elements to intermix. This propensity for phase separation is an important consideration in the study of nanocrystalline Mg-Zr alloys, as it impacts their structural and material properties.

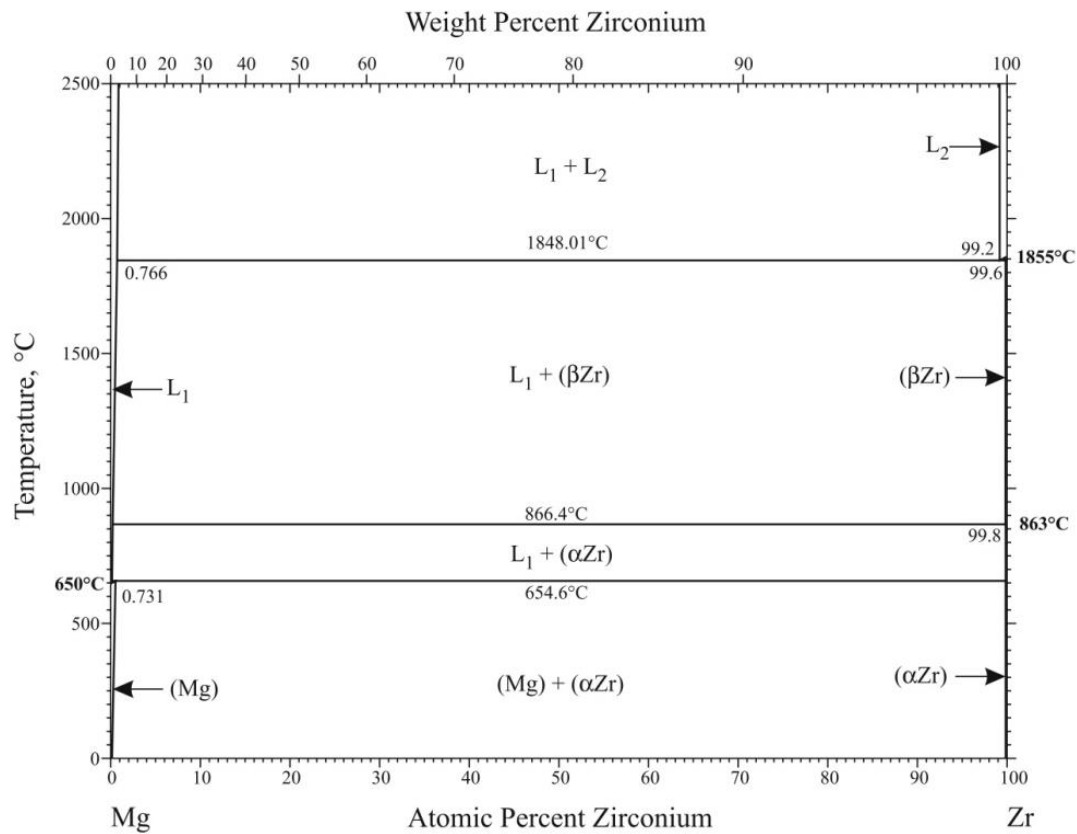


Fig. 3.1 Mg-Zr phase diagram, showing the limited solubility of the two elements.

3.1.2 Structure

Fig. 3.2 displays the SEM cross-section of Mg-Zr films, with the inserts showing the surface top-view of the as-deposited films. The thickness of the samples ranged from 590 to 900 nm, depending on the alloy composition. Specifically, a higher concentration of Zr resulted in thinner films due to the lower sputtering yield compared to Mg. In addition, the microstructure of the film can be predicted through the Thornton's diagram [2]. In this study, considering an Ar pressure of approximately 3.8 mTorr, T_{melt} of Mg and Zr of 923 and 2128 K, respectively and assuming a substrate temperature around 300 K, Zone T and Zone 1-type structures are predicted for Mg- and Zr-rich films, respectively. However, an observable transition from a compact-to-columnar structure is observed on the fracture surface for $54\% < x_{\text{Zr}} < 78 \text{ at.}\%$, while a common granular structure is observed on the surface of all the deposited films. It is worth noting that this discrepancy may be attributed to the fact that the Thornton's

diagram is based on the examination of much thicker sputtering coatings, ranging from 25 to 250 μm , which differs from the scope of this study.

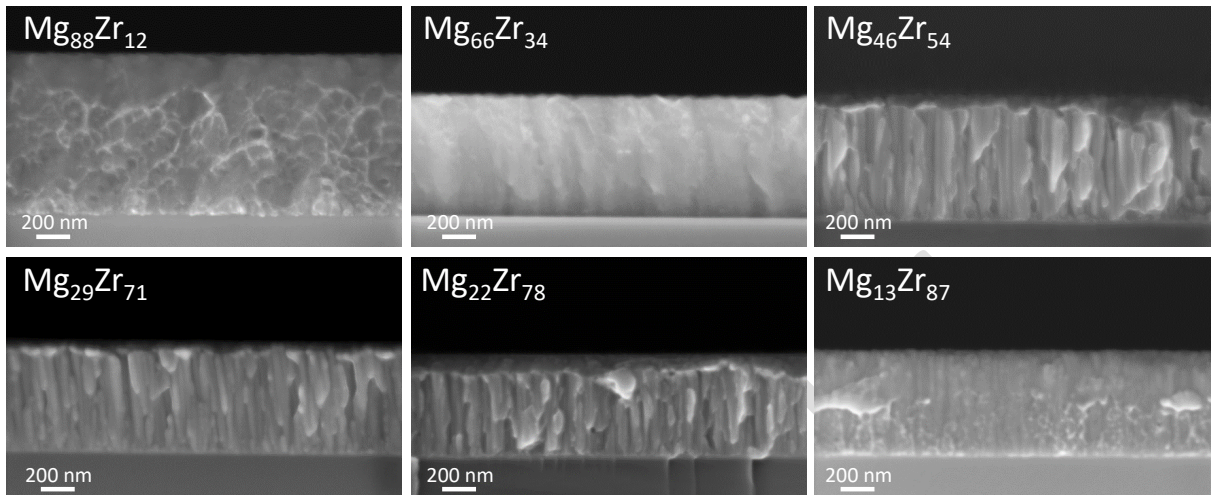


Fig. 3.2 SEM cross-view and top-surface of as-deposited Mg-Zr films exhibiting either columnar or fine grains growth. The inserts illustrate the surface top-view of the deposited films.

The mass of the substrates was measured both before and after the deposition, enabling to determine the mass of the deposited films. By combining the mass and the thickness measurements, obtained using a mechanical profilometer and SEM-cross section imaging, the mass density and related atomic volume of the films are calculated and shown in **Fig. 3.3**. The Vergard's rule provides a reliable prediction of the mass density and atomic volume by considering the values of pure Zr and Mg. These values are in good agreement with those calculated using first-principles methods, which suggests a satisfactory level of accuracy in our simulated structures.

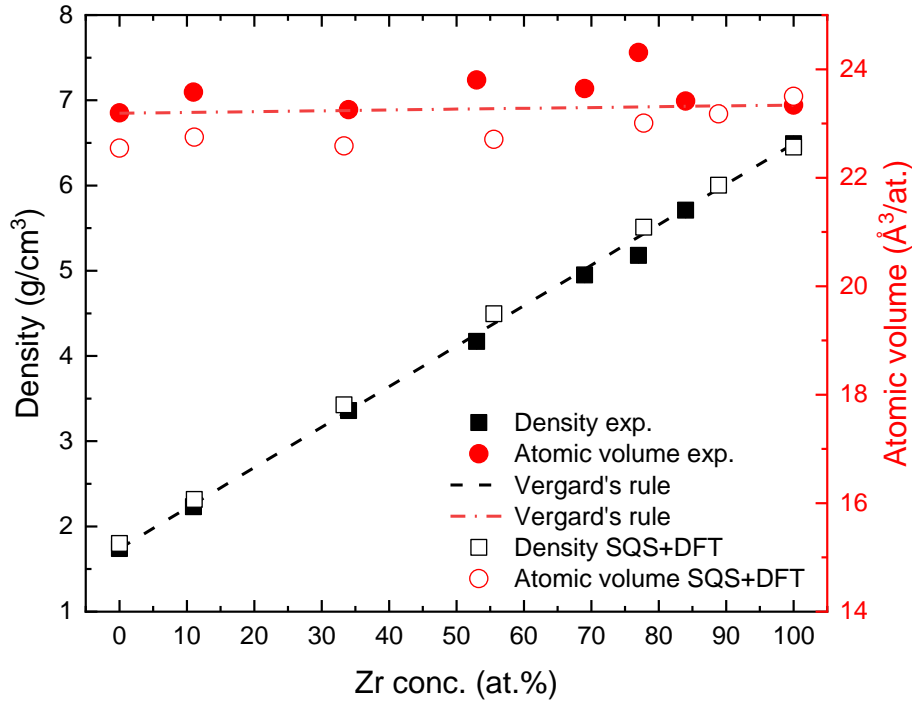


Fig. 3.3 Measured mass density ρ by weighting and atomic volume V_a of Mg-Zr films as a function of Zr content. Lines are the linear Vegard's rule of mixture. Error bars are symbol's size.

X-ray diffractograms of Mg-Zr films are displayed in **Fig. 3.4a**, revealing an HCP crystalline structure for both pure Mg and Zr. The diffractogram of pure Mg exhibits only a few peaks, indicating some preferential texturing along (002), (102), (103) and (203) crystallographic planes. In contrast, pure Zr does not show any preferential texturing. Similarly, Mg-rich films ($x_{Zr} < 50\%$) also show only three distinct main peaks attributed to the (002), (103) and (203) HCP crystalline planes of Mg. The formation energy of HCP, FCC, and BCC crystalline phases in Mg-Zr was investigated using first-principle calculations by K. Edalati *et al.* [3], showing a large energetic stability of the HCP structure except for $25 < x_{Zr} < 50$ where a slightly higher stability of the FCC structure was predicted. However, in this study the alloying of Mg-Zr resulted in an HCP crystalline structure across the entire compositional range. The lattice parameters of the various alloys and their c/a ratio were determined from the peaks-position of the crystalline planes described above and are plotted in **Fig. 3.4b**.

The HCP-lattice parameters of pure Zr and Mg were calculated (Zr: $a = 0.324$ nm, $c = 0.519$ nm and Mg: $a = 0.321$ nm, $c = 0.526$ nm), demonstrating slightly deviations in c

(5-6 pm) from bulk (powders) values (Zr: $a = 0.323$ nm, $c = 0.514$ nm and Mg: $a = 0.320$ nm, $c = 0.520$ nm) [4, 5]. This discrepancy may be attributed to the presence of residual stresses in the films, which are known to influence the positions of XRD peaks in PVD-deposited coatings [6]. The HCP-lattice parameters of Mg-Zr alloys lie within the lattice parameters of pure Mg and Zr, and are in good agreements to the first-principles calculated values of the Mg-Zr HCP random solid solutions, suggesting the dissolution and supersaturation of the two elements in each other [3]. This explains the observed HCP solid solutions in all the Mg-Zr films, with the exception of $Mg_{66}Zr_{34}$, which exhibits an asymmetric peak at $2\theta \sim 74^\circ$ associated to the superposition of (103) peaks attributed to demixed crystalline HCP-Mg and HCP-Zr phases. It's worth noting that Mg and Zr are immiscible and do not typically form intermetallic compounds under normal temperature and pressure conditions [1]. In fact, severe plastic deformation is required to mix these elements; for instance, unique nanostructured and solid solution phases were observed in Mg-50 at.% Zr fabricated through high-pressure torsion [3]. For this reason, the extreme out of equilibrium-conditions involved in PVD processes may result in a greater solubility of Mg into Zr (or *vice versa*) compared to the traditional fabrication methods.

Additionally, the Zr addition to Mg-rich films resulted in an increase of the full-width at half maximum (FWHM) of the aforementioned peaks. Moreover, **Fig. 3.4c** illustrates the grain size calculated following the same analysis of Ref. [7] with Scherrer equation. The broadening of the peaks indicates a reduction in average grain size from 32 ± 5 nm for pure Mg to 5 ± 2 nm for $Mg_{66}Zr_{34}$.

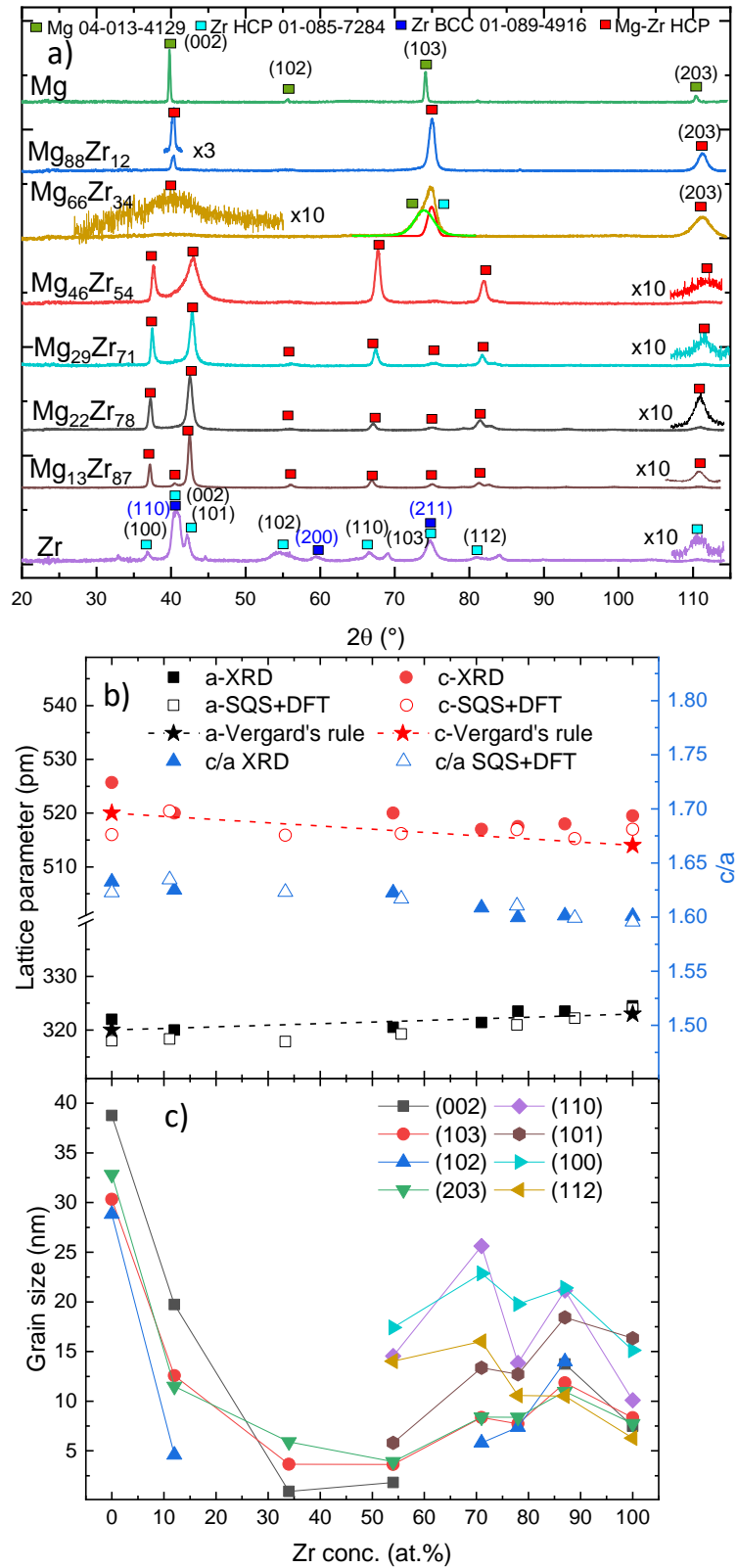


Fig. 3.4 a) XRD diffractograms of Mg-Zr nanocrystalline thin films. The peaks that are not indexed for pure Zr are from Si substrate. b) Evolution of lattice parameters of the HCP-crystalline structure. c) Grain size of the different visible orientations (hkl) as function of the Zr content of Mg-Zr alloys and pure elements.

3.1.3 Mechanical properties

The mechanical properties of Mg-Zr thin films were evaluated using nanoindentation to extract Young's modulus (E) and hardness (H), as well as Brillouin light scattering (BLS) to measure E and shear modulus (G) under an isotropic approximation. The results for G and E are presented in **Fig. 3.5a** and **Fig. 3.5b** and compared with those of bulk materials [8, 9] and values theoretically predicted by DFT methods for a random solid solutions, considering whether atoms positions were allowed to relax or not after straining the cell. Similar methods have been employed in the study of nanocrystalline materials and metallic glasses [10, 11]. Notably, the elastic moduli of the relaxed structures provided better reproducibility of the experimental values. Although both BLS and nanoindentation measurements of Young's modulus exhibit increasing trends, BLS values are approximately 10-20% lower. This difference has been previously observed and discussed in our previous study on metallic glasses having even higher yield strength [10] than the present nanocrystalline materials. The observed trends show a monotonic increase by Zr addition with some deviations from linearity which have been investigated by comparing the experimental values with the Voigt-Reuss averages defined as follows (for $M = E, G$ or H) [8, 12, 13]:

Voigt:

$$M_{tot}^V = x_{Zr}M_{Zr} + (1 - x_{Zr})M_{Mg} \quad (23)$$

Reuss:

$$\frac{1}{M_{tot}^R} = \frac{x_{Zr}}{M_{Zr}} + \frac{(1 - x_{Zr})}{M_{Mg}} \quad (24)$$

Where x_{Zr} represents the Zr concentration in volume fraction and $M_{Zr/Mg}$ denotes the G and E of bulk pure elements, in good agreement with those of the thin films investigated in this work. In the case of H , the values of pure elemental films were selected to account for Hall-Petch hardening [14]. This model considers the constant and compositionally independent contributions of the two phases, with M_{Mg} and M_{Zr} representing end-bound moduli and hardness, typical of demixed phases. As the Zr content increases, both G and E increase from 17 and 35 GPa for pure Mg to 55 and 130 GPa for pure Zr, respectively. Additionally, a similar trend is observed for hardness

(Fig. 3.5c), which increases from 0.8 to 7.5 GPa (6.8 GPa in Ref. [15]). Furthermore, the nanoindentation hardness is related to the yield strength of the material through the relation:

$$\sigma_y = \frac{H_v}{3} = \frac{H}{1.25 \cdot 3} \quad (25)$$

Where σ_y is the yield strength of the material, H_v is the Vickers hardness and H is the hardness measured by nanoindentation [16-18]. However, these trends do not follow a simple Vegard's rule of mixture (referred to here as the Voigt average) or the Reuss average. Instead, they fall between these averages, in alignment with Hill's theorem [12], which is consistent with similar findings in the case of demixed CuMo annealed alloys with immiscible constituents [19].

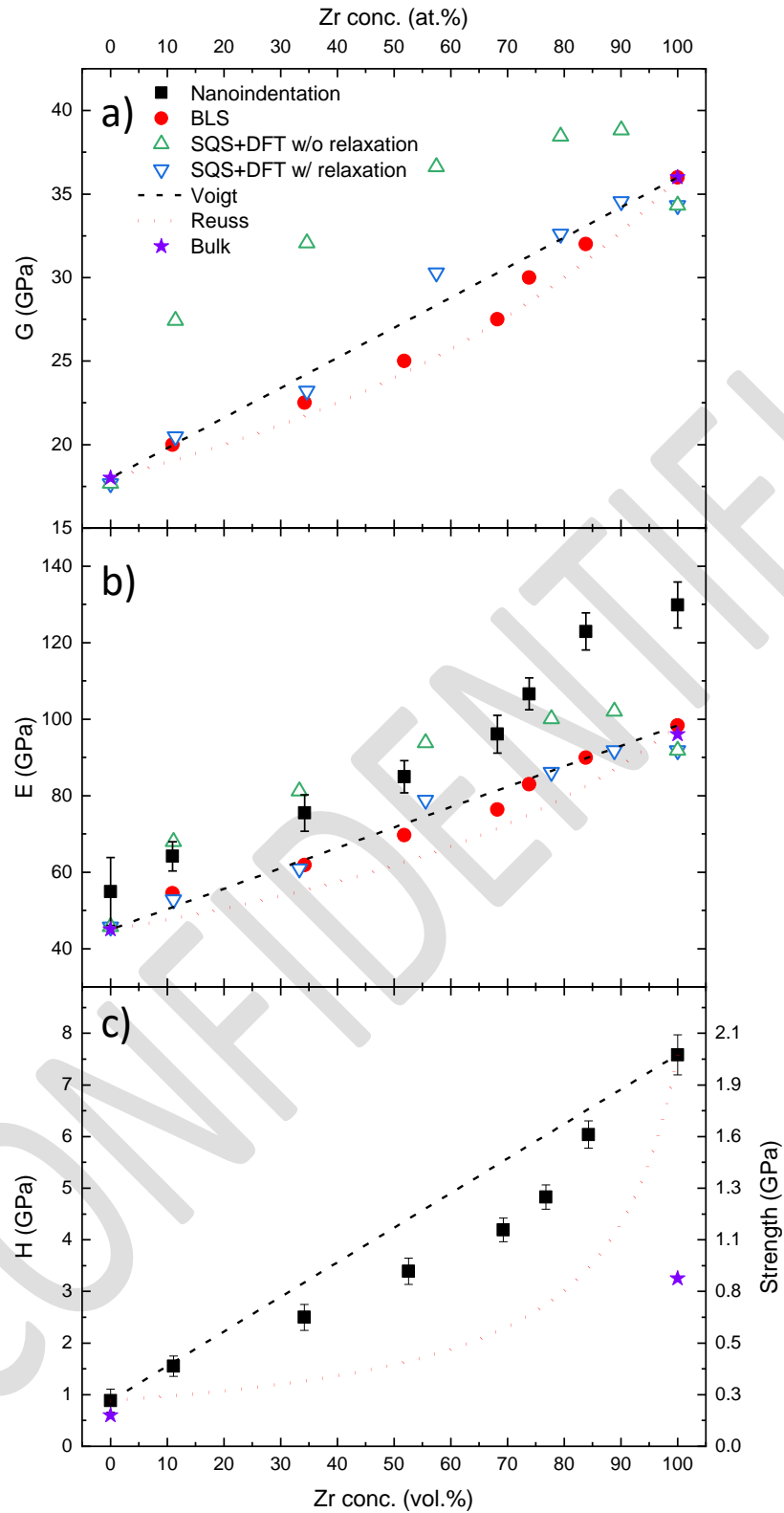


Fig. 3.5 a) Shear modulus G , b) Young's modulus E and c) hardness H of Mg-Zr films measured by nanoindentation, BLS and calculated by DFT methods and with Voigt and Reuss averages.

3.1.4 Degradation in SBF

Static immersion tests in simulated body fluid (SBF) at 37 °C were performed, and the top-view of the sample surfaces after 1 and 8 weeks of immersion is illustrated in **Fig. 3.6**. After one week of immersion, the sample with the highest magnesium content ($\text{Mg}_{88}\text{Zr}_{12}$) exhibited several noticeable macroscopic cracks on its surface, and the film delaminated in various regions. In contrast, the other compositions remained undamaged by the SBF, with their films firmly adherent to the surface.

After 8 weeks of immersion, the $\text{Mg}_{88}\text{Zr}_{12}$ displayed an increased number of cracks compared to the one-week mark, but is still remaining on the surface. The $\text{Mg}_{66}\text{Zr}_{34}$ exhibited some initial damage at the micron-scale, while the Zr-rich coatings ($x_{\text{Zr}} > 50\%$) remained adherent to the surface, showing no visible signs of delamination.

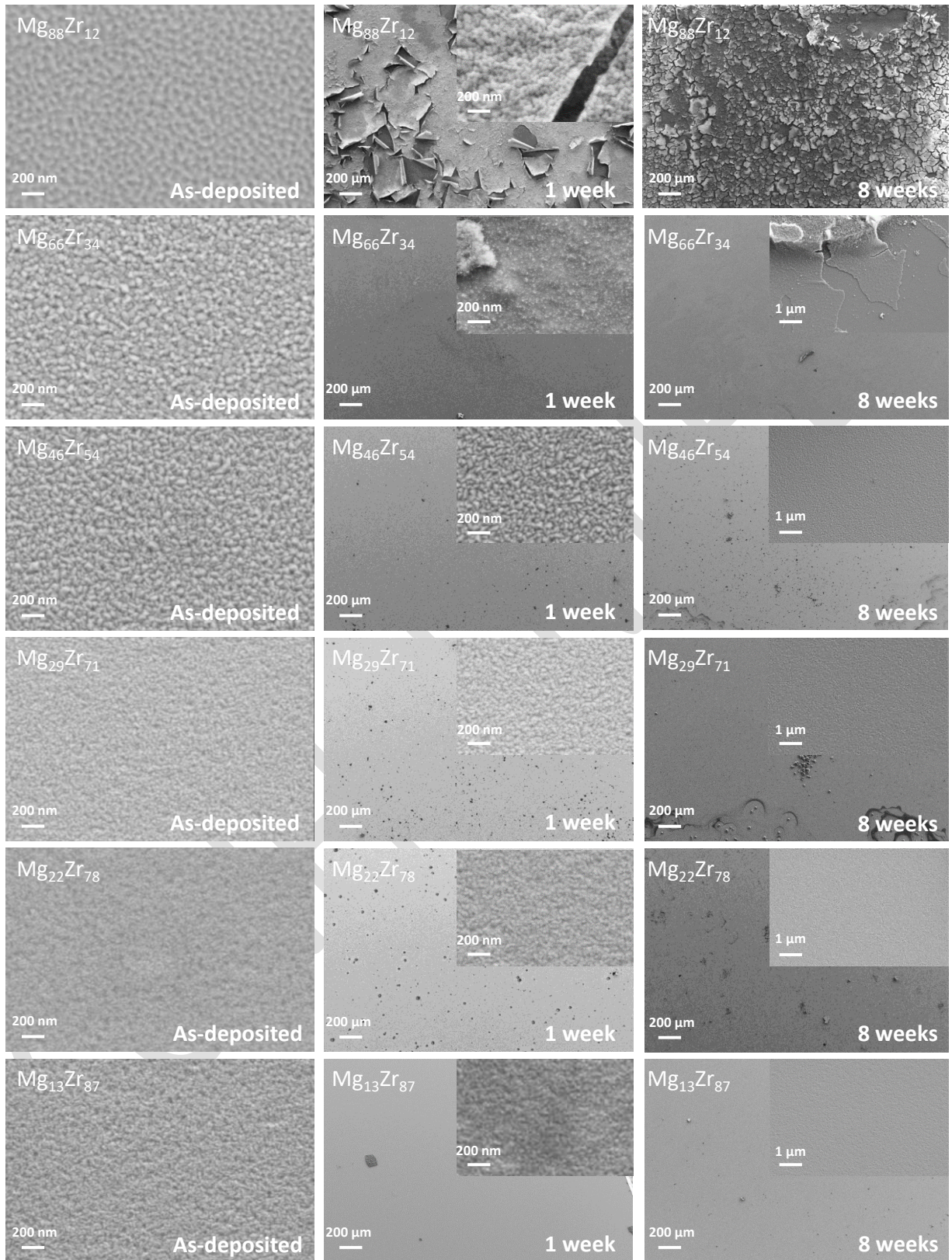


Fig. 3.6 SEM top-views of MgZr films after a) 1 week and b) 8 weeks of immersion in SBF solution at 37 °C.

3.1.5 Summary and conclusions

In summary, nanocrystalline $\text{Mg}_{100-x}\text{Zr}_x$ ($0 \leq x \leq 100$) thin films were fabricated with thicknesses ranging from 590 to 900 nm by RF magnetron co-sputtering. The crystalline structure and the mechanical properties were investigated in detail as well as the biodegradability behavior in SBF for an immersion period up to 8 weeks. The XRD analysis revealed that Mg-Zr films formed HCP-solid solutions with the exception for $\text{Mg}_{64}\text{Zr}_{36}$ which shows demixed HCP-Mg and HCP-Zr phases. In addition, the average grain size was reduced from 32 ± 5 nm for pure Mg to 5 ± 2 nm for $\text{Mg}_{64}\text{Zr}_{36}$. The static immersion test of Mg-Zr films showed a premature cracking and delamination of the richest-Mg film ($\text{Mg}_{88}\text{Zr}_{12}$) after one week, while the other Zr-richer compositions resulted still adherent to the surface even after 8 weeks of immersion. Moreover, some micron-scale corrosion products were present on the surface of $\text{Mg}_{64}\text{Zr}_{36}$ after 8 weeks of immersion. The mechanical characterization showed that G , E and H of Mg-Zr alloys lie in between pure Mg and Zr ones, following the Voigt-Reuss-Hill averages, and are in good agreements with first-principles calculations of Mg-Zr solid solutions. The values of these elastic quantities cover a wide range. Both G and E increase from 17 and 35 GPa for pure Mg up to 55 and 130 GPa for pure Zr, while H and σ_y increases from 0.8 and 0.2 GPa up to 7.5 and 2 GPa, respectively.

In conclusion, this chapter focused on the fabrication and characterization of nanocrystalline Mg-Zr thin films coatings. It was demonstrated that this class of materials exhibits a wide range of mechanical properties, and it was also shown that the addition of Zr can be used to modulate the biodegradability behavior and grain size of Mg-rich coatings. Finally, these preliminary findings may provide a foundation for future research aimed at developing tailored nanocrystalline coatings with customized structures and tuned physical properties in alignment with the specific requirements for targeted biomedical applications, offering promising enhancements for existing metallic implants.

3.2 Zn-based binary alloys: ZnMg and ZnZr

3.2.1 Thin film synthesis and composition tailoring

Prior to deposition, the base chamber pressure was minor than 10^{-5} Pa and the depositions were performed at a working pressure of $p = 0.5$ Pa with a constant Ar flow rate of 40 sccm. The substrate was at a distance $d = 9.4$ cm from the cathodes (hence, $p \times d = 4.7$ Pa.cm) and kept at room temperature (T_{room}) while rotating at 10 rpm. The RF power applied to the targets was calibrated to apply and ranged from 25 to 200 W to obtain a wide compositional range of ZnMg and ZnZr films. For the ZnZr samples, the nominal thickness was fixed to around 400 nm, while ZnMg films were from 600 to 800 nm-thick.

Fig. 3.7 illustrates the elements concentration measured by EDX of the deposited alloys in relation to the applied power ratio of the targets (P_{Zn}/P_{Zr} and P_{Zn}/P_{Mg}) during the deposition process. A strong correlation between the chemical composition of the films and the power target ratio is observed, suggesting that precise control over film composition can be achieved by appropriately adjusting the power targets ratio during the deposition process. A similar methodology has been employed in other studies involving ZrCu metallic glasses [20, 21].

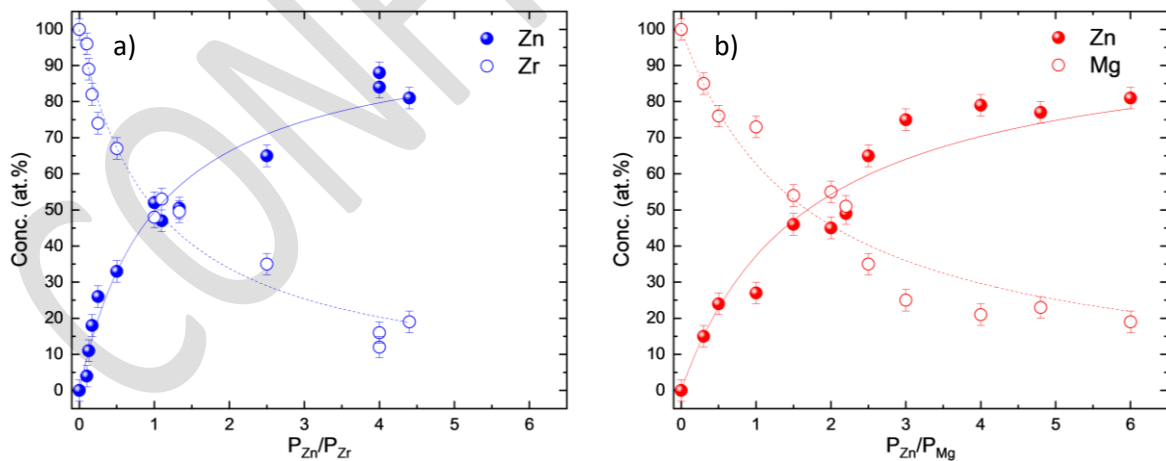


Fig. 3.7 Thin film chemical composition as function of the magnetron targets RF-applied power ratio during the deposition process of a) ZnZr and b) ZnMg films. The solid and dashed lines are guide for eyes for Zn and Zr (or Mg) points, respectively.

Furthermore, **Fig. 3.8** depicts a comparison between experimentally measured mass density (and atomic volume) and values calculated through AIMD and SQS methods, demonstrating a strong agreement. Particularly, both crystalline and amorphous alloys' density and atomic volume exhibit a linear trend that aligns closely with the values of the constituent pure elements.

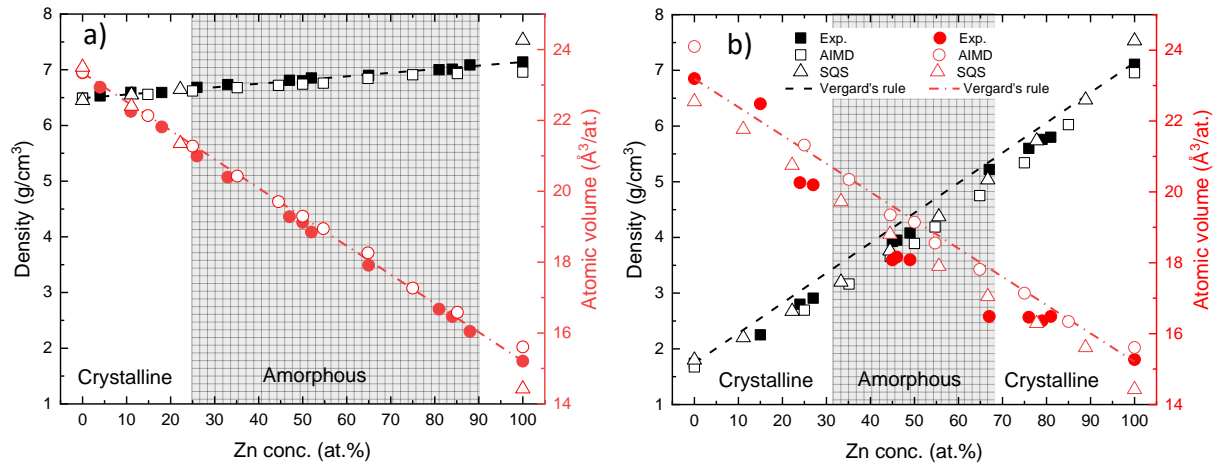


Fig. 3.8 Measured and calculated mass density and atomic volumes of a-c) ZnZr and b-d) ZnMg.

3.2.2 Glass-forming ability and average interatomic distance

Contrarily to MgZr, ZnZr and ZnMg have negative values of mixing enthalpy and several intermetallic are present in their phase diagrams illustrated in **Fig. 3.9**. These features suggest an improved glass forming ability compared to MgZr and several films along the entire compositional range have been deposited to identify the glass-forming compositional range of these systems.

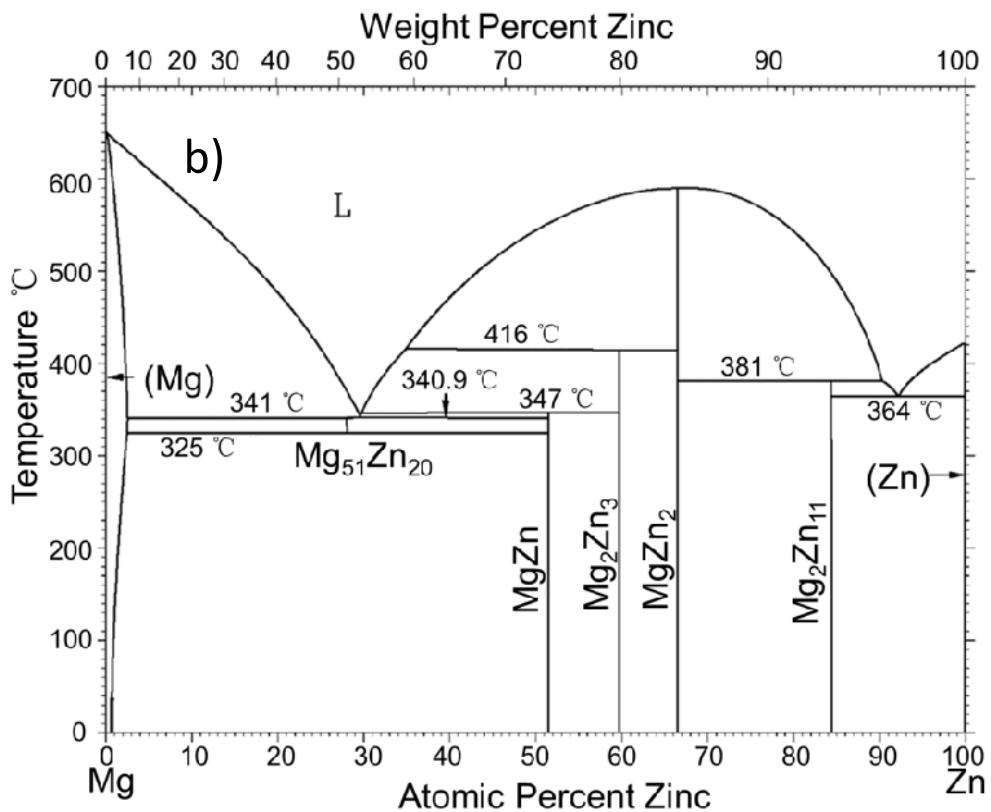
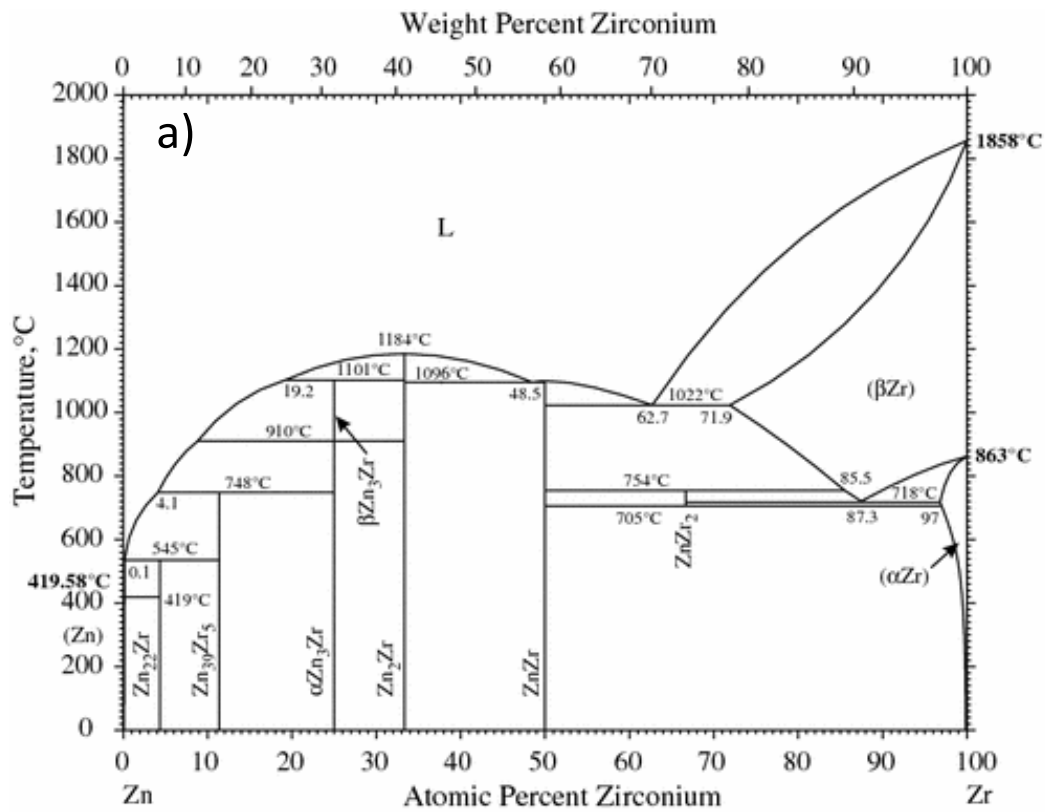


Fig. 3.9 Phase diagram of a) ZnZr and b) ZnMg showing the presence of several intermetallic [22, 23].

The model proposed by J. M. Lòpez et al. [24] was used to assess the GFA of ZnZr and ZnMg alloys, enabling the prediction of free energy of formation for both amorphous (ΔG_{am}) and crystalline phases (ΔG_{ss}). Further information can be found in the Section 2.1.1. The results, depicted in Fig. 3.10, indicate a predicted compositional amorphization range, where $\Delta G_{am} < \Delta G_{ss}$, of 24 to 95 at.% Zn for ZnZr alloys and 20 to 90 at.% Zn for ZnMg alloys.

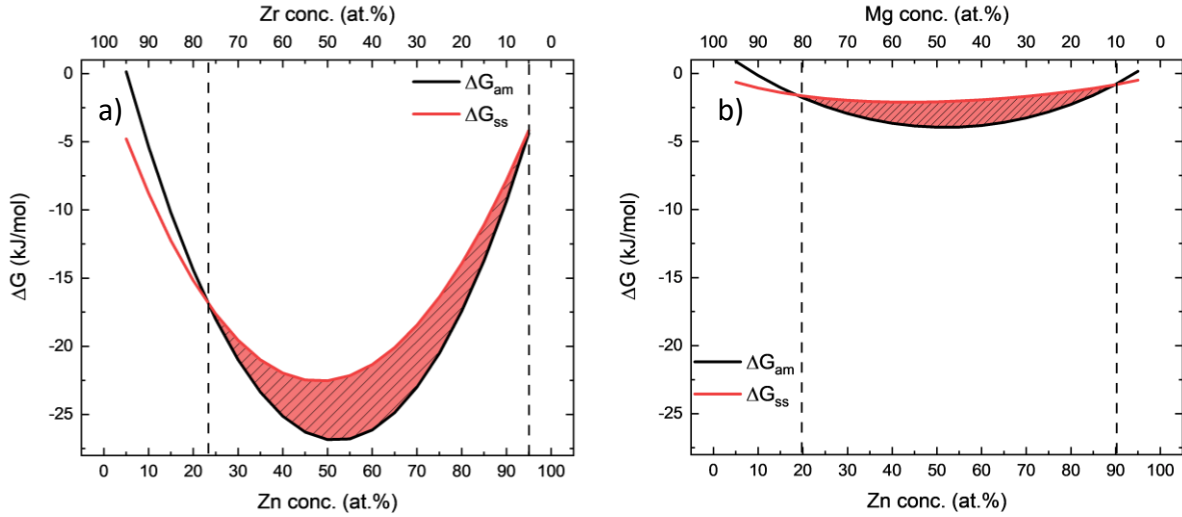


Fig. 3.10 Free-energy of formation of amorphous (ΔG_{am}) and crystalline (ΔG_{ss}) phases for a) ZnZr and b) ZnMg alloys. The thermodynamically predicted glass-forming compositional range is identified by the dashed lines where $\Delta G_{am} < \Delta G_{ss}$.

To validate these thermodynamical findings, the theoretical glass-forming compositional ranges were compared to the amorphous compositions found in XRD diffractograms (detailed in Section 2.1.1), as shown in Fig. 3.11. The diffractograms of ZnZr films show a broad primary diffraction peak (PDP) in the range of $2\theta \approx 42-47^\circ$, which is characteristic of amorphous materials. This broad peak is consistently present across a wide range of compositions, ranging from 26 to 88 at. % of Zn, indicating a superior GFA of ZnZr compared to ZnMg films. All crystalline Zr-rich ZnZr films exhibit distinct peaks at $2\theta \approx 41, 42, 60,$ and 75° , corresponding to hexagonal close-packed (HCP) Zr-Zn solid solution. Notably, in $Zn_{18}Zr_{82}$, the broad peak at $2\theta \approx 41^\circ$ indicates a convolution of nanocrystalline peaks of (002) and (101) HCP Zr-Zn solid solution phase. For ZnMg, a narrower compositional range for amorphization limited to 45-67 at. % Zn is observed, thereby highlighting the lower GFA compared to ZnZr films. Composite

amorphous/nanocrystalline structures are observed for compositions close to the crystalline-to amorphous transition, in particular for $Zn_{27}Mg_{73}$, where both amorphous hump and crystalline peaks are present. Crystalline Mg-rich films exhibit a large single peak at 74-75°, corresponding to the presence of nanocrystalline demixed Mg. On the other hand, Zn-rich ZnMg compositions close the amorphous-to-crystalline transition, $Zn_{75}Mg_{25}$, and $Zn_{76}Mg_{24}$, show the presence of demixed nanocrystalline Zn and a broad peak which is too large and flat for an amorphous hump, suggesting the presence of nanocrystalline intermetallic $MgZn_2$ and/or Mg_2Zn_{11} phase. However, due to the overlapping of several large crystalline peaks in $Zn_{79}Mg_{21}$ and $Zn_{81}Mg_{19}$, it is challenging to precisely discriminate the individual crystalline phases and the presence of Mg_2Zn_{11} is not excluded among the possible present intermetallic crystalline phases.

CONFIDENTIAL

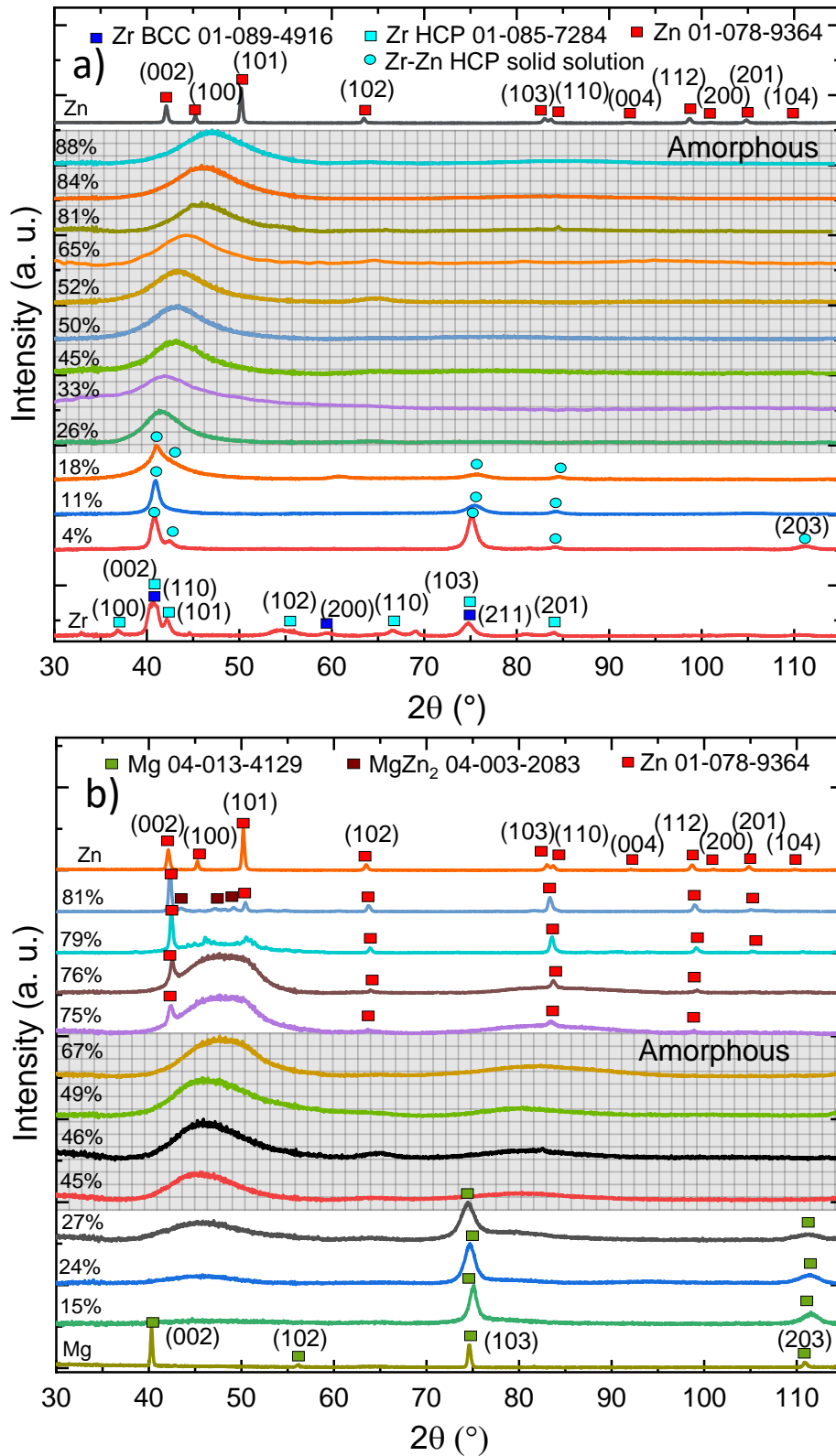


Fig. 3.11 XRD diffractograms in the Bragg angular range of $2\theta = 30\text{-}115^\circ$ of a) ZnZr thin films and b) ZnMg thin films. The percentages on the right-side of the graphs indicate the Zn content, while the grey panels highlight the compositional range of amorphization.

The position of the crystalline peaks highlighted in **Fig. 3.11** enabled the calculation of the lattice parameters (a and c for HCP structures) of both nanocrystalline ZnZr and ZnMg alloys. **Fig. 3.12** illustrates the measured and calculated lattice constants (a and c) and grain size determined using the Scherrer formula [7], for the nanocrystalline phases whose compositions are located beyond the glass-formation compositional range. In both systems, the grain size ranges from 35 to few nanometers. In the case of ZnZr films, the lattice parameter values (and their ratio) display gradual variations with Zn addition from $a \sim 326$ nm, $c \sim 520$ nm, $c/a \sim 1.59$ for pure Zr to $a \sim 320$ nm, $c \sim 510$ nm, $c/a \sim 1.59$ for $\text{Zn}_{18}\text{Zr}_{82}$, in good agreement with those obtained for solid solutions through SQS methods, indicating the formation of Zr-Zn HCP solid solutions in Zr-rich films. Conversely, in ZnMg films, the nearly consistent lattice parameters of both Mg-rich and Zn-rich alloys closely match the lattice parameters of the respective pure elements (Mg: $a \sim 319$ nm, $c \sim 522$ nm, $c/a \sim 1.63$; Zn: $a \sim 268$ nm, $c \sim 494$ nm, $c/a \sim 1.85$), confirming the presence of demixed Mg and Zn phases.

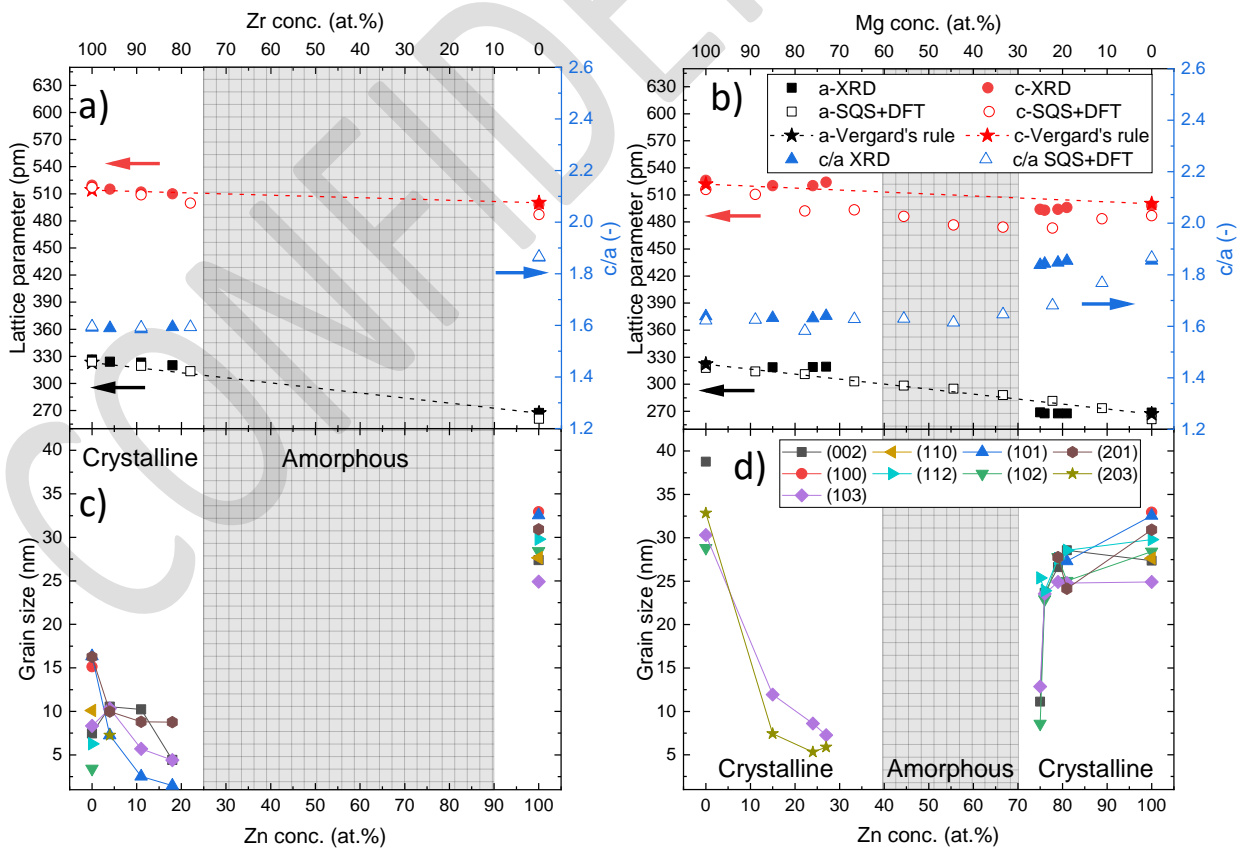


Fig. 3.12 Lattice parameters a and c (and their ratio c/a) and grain size calculated from XRD peaks of a-c) ZnZr and b-d) ZnMg alloys.

The position of the PDP in ZnMg and ZnZr TFMGs shifts towards larger 2θ values while increasing the Zn content and this is strictly related to the shortening of average interatomic distances (d_{av}) which can be calculated through the Ehrenfest equation [25]. Under the hypothesis of diatomic molecules with fixed interatomic distances (d_{av}) which scatter independently, the Ehrenfest relation is derivable from the simplified Debye formula and setting its derivative to zero [26] obtaining:

$$1.23 \lambda = 2d_{av} \sin \theta \quad (26)$$

where λ is the wavelength of the X-ray used (Co-K α =1.788965 Å) and θ is the Bragg's angle. Furthermore, the variation of d_{av} can be predicted as well with theory of alloys, especially by using the Zen's law which is an empirical model that considers the interatomic distance as the average on atomic volumes [27], for example for ZnZr alloys:

$$d_{av} = 2(f_{Zn}r_{Zn}^3 + (1 - f_{Zn})r_{Zr}^3)^{1/3} \quad (27)$$

where f_{Zn} is the atomic fraction of Zn, r_{Zn} and r_{Zr} are the atomic radii of Zn and Zr (here, we used the ones calculated by AIMD, 133, 157 and 154 pm for Zn, Zr and Mg respectively). These AIMD-calculated atomic radii and average interatomic distances of amorphous alloys were evaluated with by analyzing the position of the first peak in the computed pair distribution functions (PDFs), indicative of the atomic distances between the nearest neighbors on the first shell of coordination [28]. As shown in **Fig. 3.13**, the shift of the first peak highlights the shortening of average interatomic distances in both amorphous ZnZr and ZnMg alloys with the increase of Zn content.

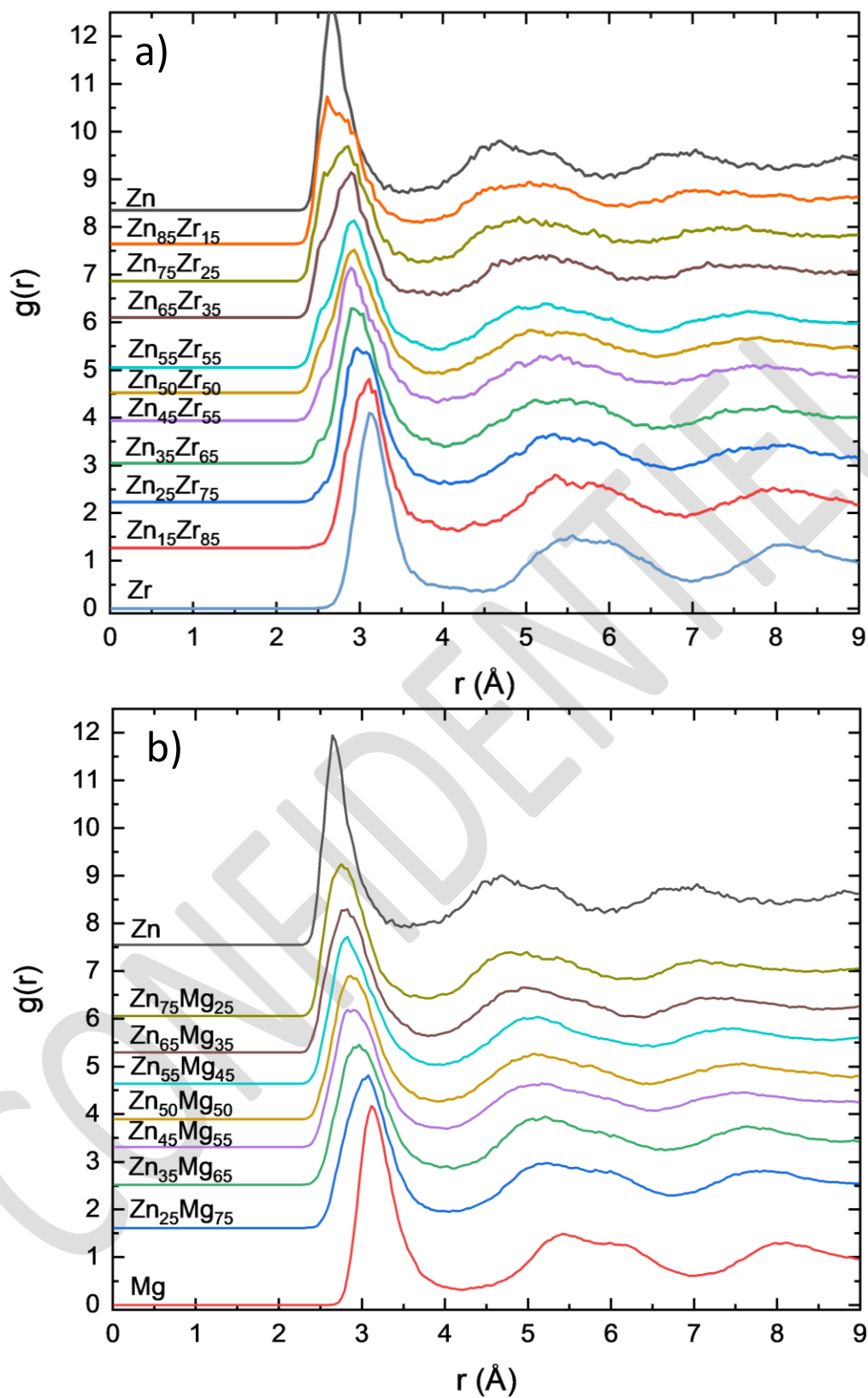


Fig. 3.13 Calculated pair distribution function of a) ZnMg and b) ZnZr with different content of Zn.

Finally, the experimental and theoretically predicted values of d_{av} in the glassy state are represented in **Fig. 3.14** which exhibits a good overall agreement. Within the crystalline-forming compositional range of ZnZr, the values of d_{av} closely correspond to SQS values, providing evidence for the existence of a solid solution. Contrarily, in the case of crystalline ZnMg alloys, d_{av} aligns more closely with that of the pure elements, in agreement with segregation of Zn and Mg.

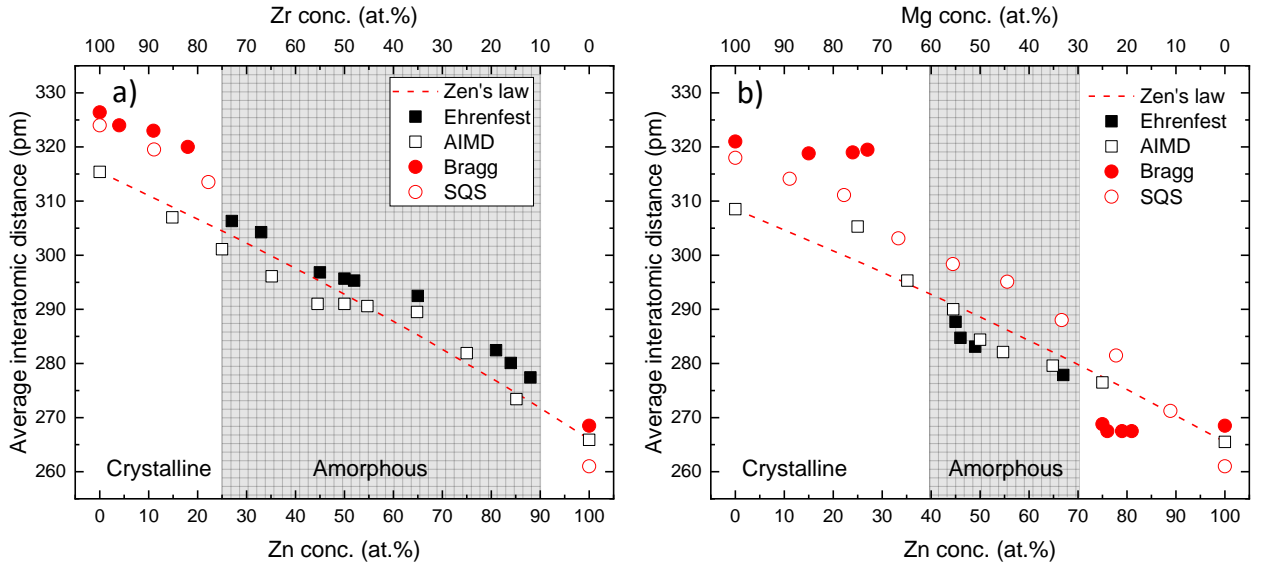


Fig. 3.14 Average interatomic distances of a) ZnZr and b) ZnMg thin films measured experimentally (through the Ehrenfest equation) compared with those predicted from Zen's law and calculated by AIMD and SQS methods.

3.2.3 Hardness, yield strength and mismatch entropy

The hardness measured by nanoindentation gives an estimation of the yield strength of the material through the relation:

$$\sigma_y = \frac{H_v}{3} = \frac{H}{1.25 \cdot 3} \quad (28)$$

where σ_y is the yield strength of the material, H_v is the Vickers hardness and H is the hardness measured by nanoindentation [16-18]. It is known that the hardness of MGs is related to the packing density of the material [29, 30] and Mansoori *et al.* [31] showed that the packing of two atomic species with different radii generates mismatch entropy ΔS^δ which can be calculated by the solution of the generalized Percus-Yevick

equation for a mixture of hard spheres [32] (refer to **Equation 13** in Section 2.1.1). **Fig. 3.15a** and **Fig. 3.15b** show, respectively, the measured H and the estimated σ_y of ZnZr and ZnMg thin films as function of the Zn content. The maximum hardness values for ZnZr and ZnMg were 7.5-8 GPa and 5.5 GPa, respectively. These values correspond to the range of composition between 45 and 65 at. % Zn which match to the maximum of ΔS^δ , and a maximum yield strength ~ 2 GPa for ZnZr and ~ 1.3 GPa for ZnMg.

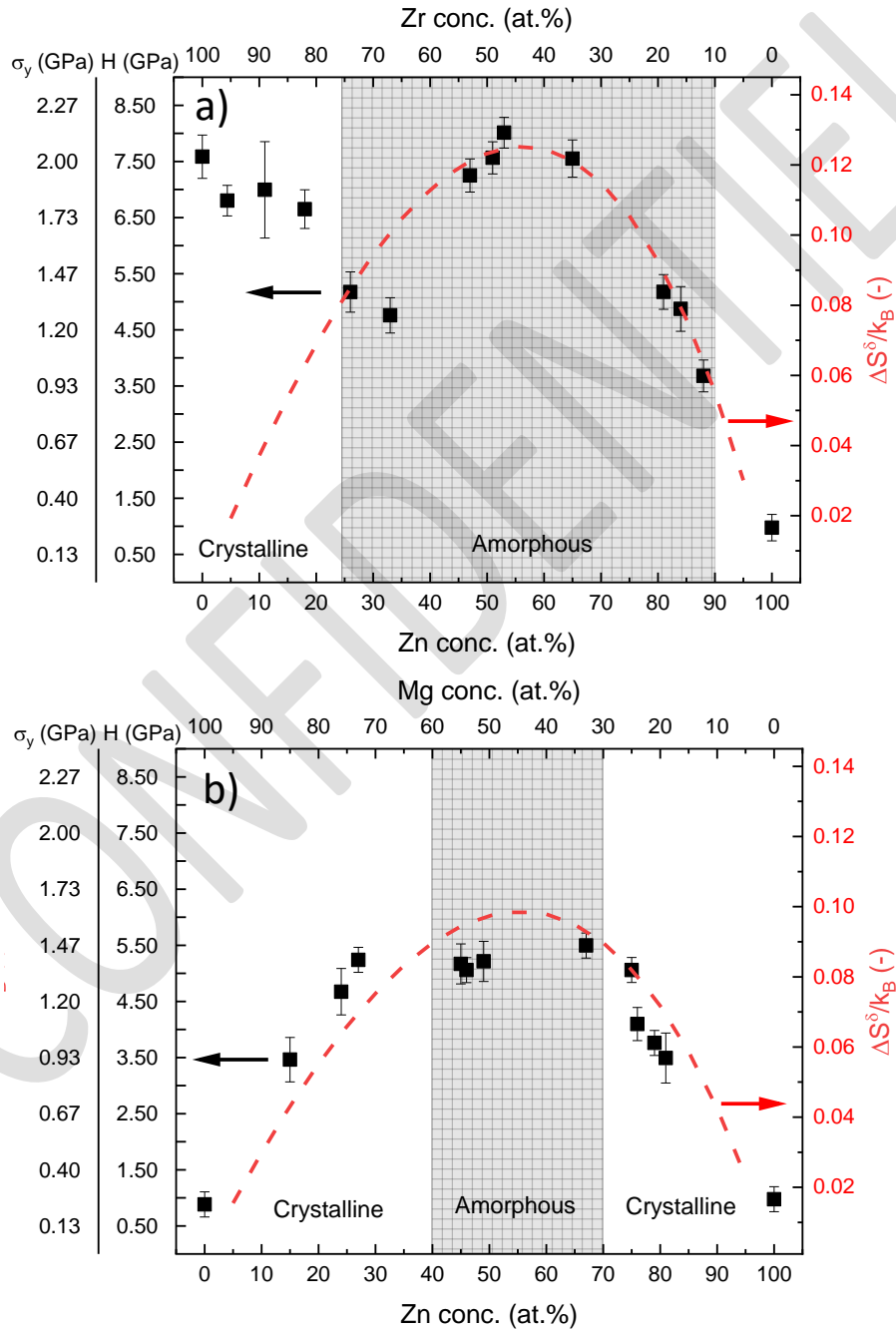


Fig. 3.15 Measured hardness H , estimated yield strength σ_y and calculated mismatch entropy ΔS^δ divided the Boltzmann constant k_B for a) ZnZr and b) ZnMg alloys.

3.2.4 Elastic moduli

The mechanical properties of ZnZr and ZnMg thin films were assessed using nanoindentation to extract Young's modulus (E) and hardness (H), as well as Brillouin light scattering (BLS) to measure Young's modulus (E) and shear modulus (G). **Fig. 3.16** presents two typical BLS spectra of ZnZr and ZnMg and the correspondent surface modes frequencies. Simulating the spectrum, it is possible to extract the longitudinal elastic constant C_{11} (in **Fig. 3.17**) and the longitudinal sound velocity $V_L=(C_{11}/\rho)^{1/2}$ (related to S_i frequency position), and the shear elastic constant C_{44} (in **Fig. 3.17**) and the shear sound velocity $V_T=(C_{44}/\rho)^{1/2}$ (related to R frequency position). ρ represents the mass density of the film illustrated in **Fig. 3.8**.

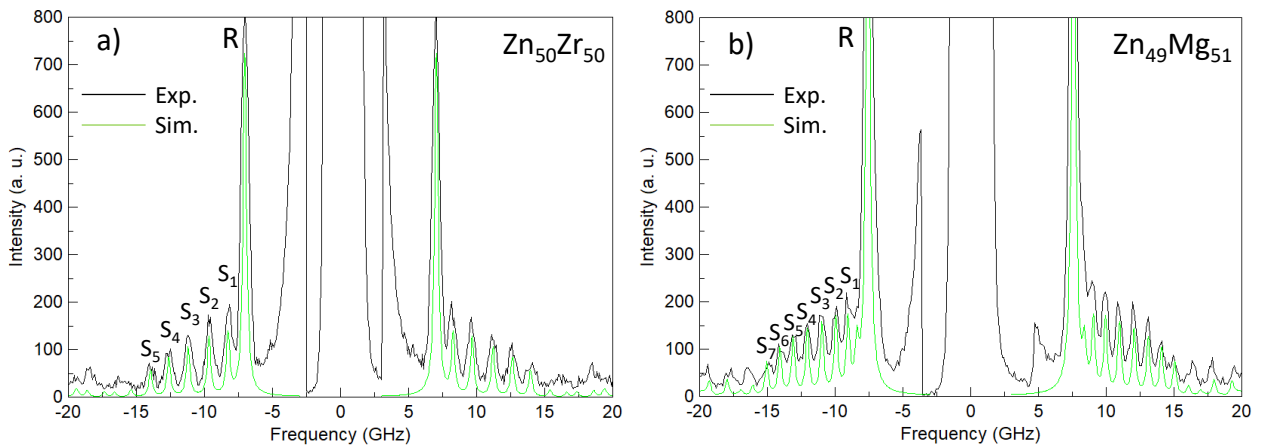


Fig. 3.16 BLS spectra of a) 450 nm-thick $Zn_{50}Zr_{50}$ and b) 650 nm-thick $Zn_{49}Mg_{51}$. The labels R and S_i indicate the frequency peaks related to Rayleigh and Sezawa surface modes, respectively. The black line represents the experimental data while the green line illustrates the simulation.

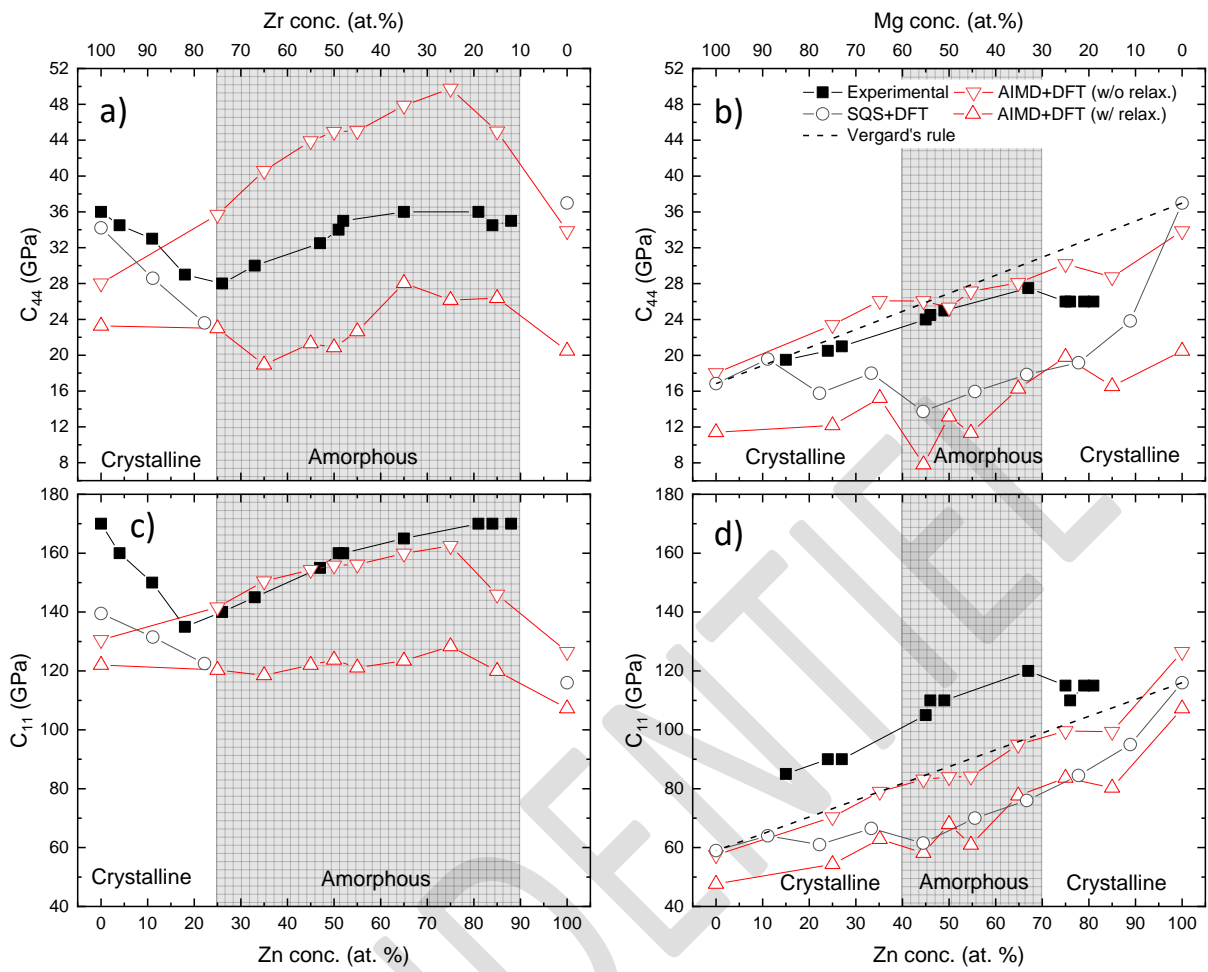


Fig. 3.17 Elastic constants (C_{44} and C_{11}) measured by BLS and calculated by AIMD (or SQS) and DFT of a-c) ZnZr and b-d) ZnMg alloys. The values predicted by SQS+DFT methods were obtained by using the Hill average [12]. The dashed line represent Vergard's rule between pure crystalline Zn and Mg values from SQS+DFT.

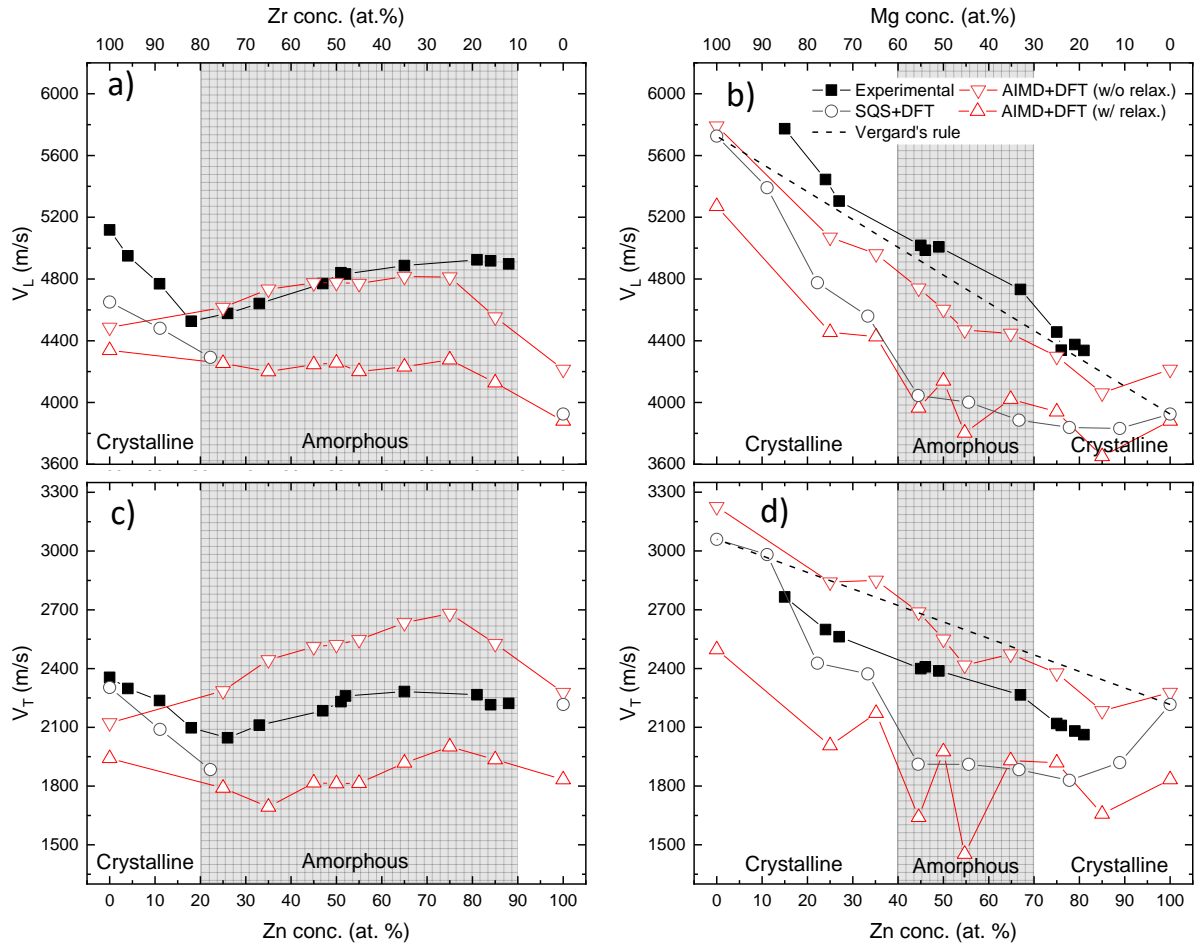


Fig. 3.18 Longitudinal (V_L) and transversal (V_T) sound velocities measured by BLS and calculated by AIMD (or SQS) and DFT of a-c) ZnZr and b-d) ZnMg alloys. The values predicted by SQS+DFT methods were obtained by using the Hill average [12]. The dashed line represent Vergard's rule between pure crystalline Zn and Mg values from SQS+DFT.

Assuming the material's isotropy (which is perfectly valid in the case of metallic glasses and non-textured polycrystalline materials), C_{11} is directly related to C_{12} and C_{44} through the relation $C_{11}=2C_{44}+C_{12}$. Hence, these constants are determined by simulating the entire BLS spectra with the frequency positions of Rayleigh (R) and Sesawa modes (S_i) and the resulting values of C_{44} and C_{11} are presented and compared with first principle-calculated values in **Fig. 3.17**. In ZnZr films, SQS methods well-predict the decreasing in elastic constants of nanocrystalline films, while AIMD method (being relaxed and unrelaxed structures the lower and upper theoretical limits) can reproduce the trend of the elastic constants in the glass-forming compositional range.

For ZnMg, C_{44} is mostly comparable with Vergard's rule of mixture, typical of demixed phases and the presence of nanocrystalline phases might lead to a stiffening (increase in C_{11}) of the material. Similar statements are valuable for sound velocities displayed in **Fig. 3.18**.

The Debye temperature shown in **Fig. 3.19**, is closely related to phase transitions in the material and is calculated using the formula:

$$T_{Debye} = \frac{\hbar}{k_B} \left[\left(\frac{3}{\frac{1}{V_L^3} + \frac{2}{V_T^3}} \right) \frac{6\pi^2}{V_{at}} \right]^{\frac{1}{3}} \quad (29)$$

Where k_B is the Boltzmann constant and V_{at} is the atomic volume illustrated in **Fig. 3.8**. For ZnMg, the experimentally measured Debye temperature decreases monotonically from ~290 K for pure Mg, in agreement with bulk experimental value of 318 K [33] to 270 K for $Zn_{80}Mg_{20}$ much below the one of pure Zn: ~320 K [34]. This tendency makes challenging the identification of the first transition from Mg-rich crystalline alloys to amorphous phase.

The presence of nanocrystallites in the amorphous matrix makes the nanocomposite stiffer, which in turn give an apparent higher Debye temperature. However, in the case of ZnZr, the Debye temperature initially is of 275 K for pure α -Zr, which agrees with the experimental and DFT calculations values of 274.4 [35] and 273.6 K [8], respectively. Then it decreases to 250 K for $Zn_{25}Zr_{75}$, which coincides with the crystalline-to-amorphous transition observed experimentally, followed by an increase to 300 K for $Zn_{90}Zr_{10}$, again this is in agreement with the pure zinc Debye temperature of ~320 K [34].

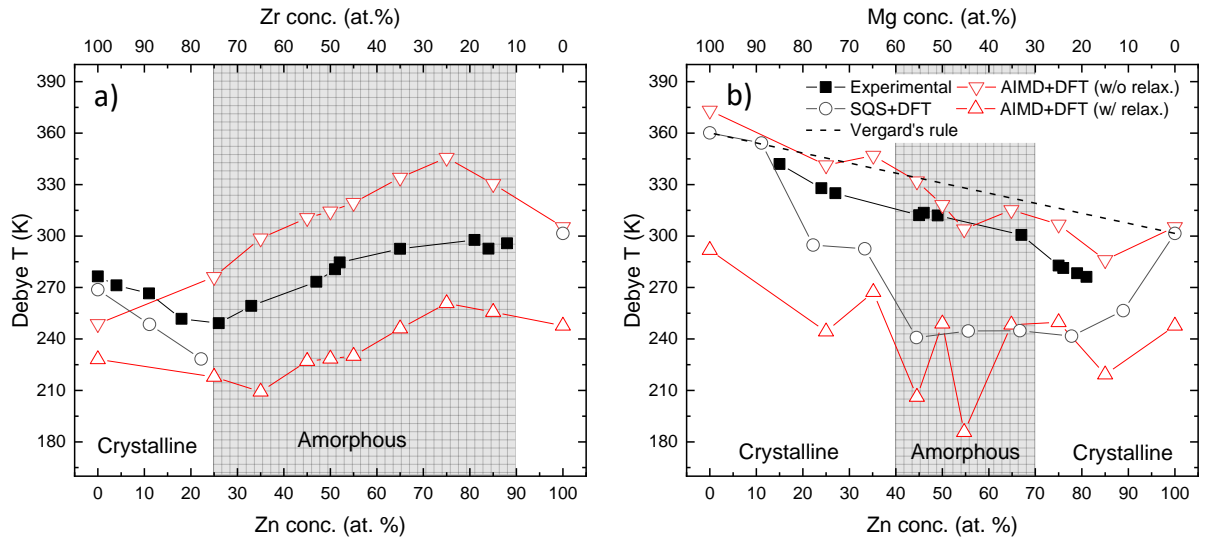


Fig. 3.19 Debye's temperatures measured by BLS and calculated by AIMD (or SQS) and DFT for ZnZr and ZnMg alloys. The values predicted by SQS+DFT methods were obtained by using the Hill average [12]. The dashed line represent Vergard's rule between pure crystalline Zn and Mg values from SQS+DFT.

The measured elastic moduli of ZnZr and ZnMg, calculated as $G = C_{44}$ and

$$E = \frac{C_{44}(3C_{11} - 4C_{44})}{(C_{11} - C_{44})} \quad (30)$$

were compared with the values predicted by DFT calculations at 0 K for the glassy and crystalline solid solutions (generated with AIMD and SQS methods, respectively) in **Fig. 3.20**. In case of amorphous materials, these comparisons were performed considering both relaxed and unrelaxed structures, where atomic positions were either allowed or not allowed to relax after straining the cell, respectively. In disordered materials like metallic glasses, the atomic positions of each element are not equivalent, preventing uniform elastic relaxation throughout the entire volume like in a crystalline lattice. This is due to the change in local atomic ordering and chemical neighboring for all non-equivalent positions within the simulated cell having a finite volume (but being periodically repeated) and it is depending on the type of applied strain (tension or shear).

As predicted by SQS+DFT methods, the elastic moduli of Zr-rich films show a softening effect about $\sim 30\%$ with the addition of Zn up to 25 at. %. Within the glass-forming compositional range, further Zn addition up to 50 at. % results in an increase in elastic

moduli of ~30%. This stiffening effect is attributed to the shortening of the average interatomic distance (d_{av}) mentioned in Section 3.2.2, related to the increasing fraction of stiffer homometallic Zn-Zn and heterometallic Zr-Zn bonds, regardless the homometallic Zr-Zr bond. As the Zn content surpasses this range, the elastic moduli reach a plateau, converging towards values calculated for the hypothetical amorphous Zn (a-Zn). In contrast to ZnZr, the elastic moduli of ZnMg **Fig. 3.20b**) exhibit a monotonic increase with the addition of Zn linked to the shortening of average interatomic distances and an augmented fraction of stiffer homometallic Zn-Zn and heterometallic Mg-Zn bonds, again converging towards values calculated for amorphous Zn (a-Zn). Overall, the Young's modulus and shear modulus of ZnZr thin films fall within the range of 75-100 GPa and 28-35 GPa, while for ZnMg thin films their values are within 60-75 GPa and 25-30 GPa, respectively. It is also worth noting that the elastic moduli values (E , G) of the virtual pure a-Zn and a-Mg are close to those of their polycrystalline counterparts: 96 and 43 GPa for Zn [36] and 46 and 17 GPa for Mg [9], respectively. Conversely, the elastic moduli of virtual a-Zr (57 and 21 GPa) differ from the values for polycrystalline counterpart (95 and 36 GPa [8]), in line with existing literature [37].

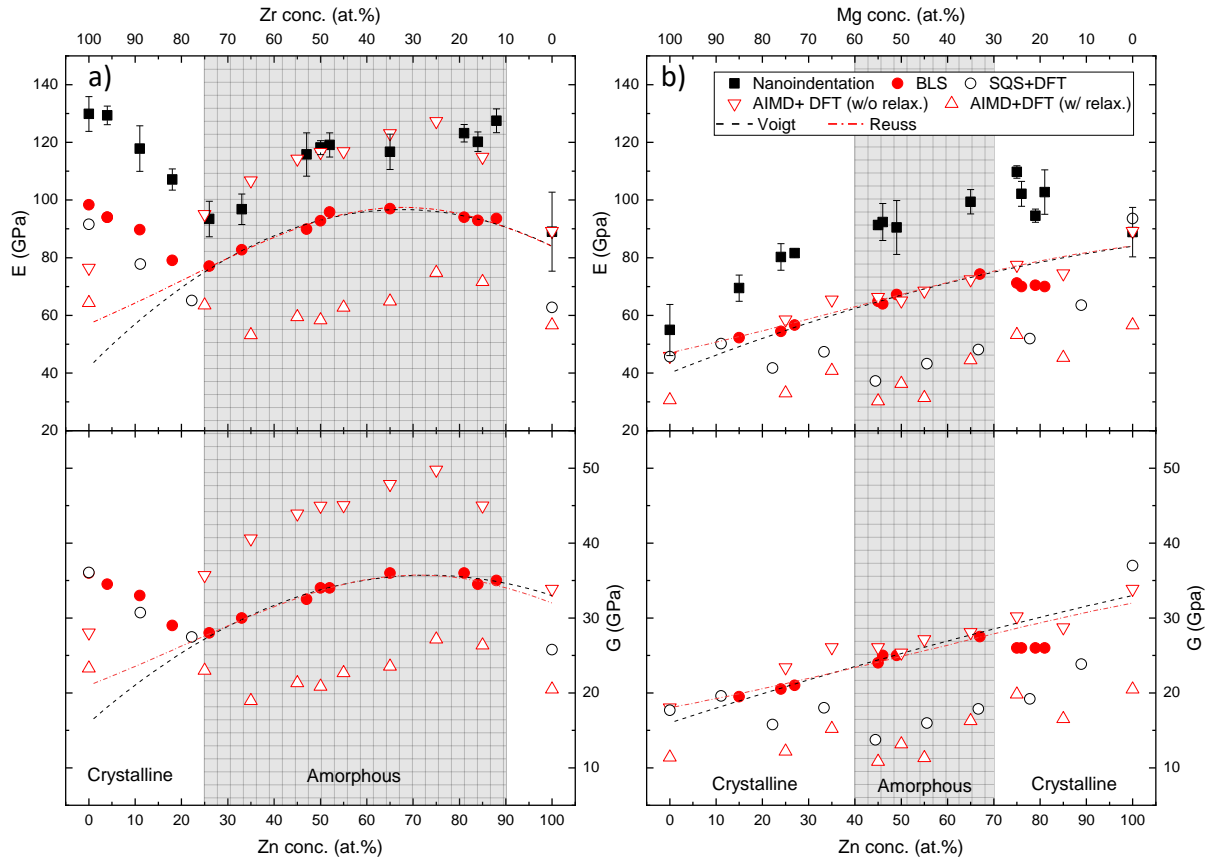


Fig. 3.20 Elastic moduli measured by nanoindentation and BLS techniques at room temperature and calculated by density functional theory at 0 K for a) ZnZr and b) ZnMg alloys. The dashed and point-dashed lines indicate the Voigt and Reuss fits, respectively, of elastic moduli measured by BLS in the glass-forming compositional range. Empty symbols are DFT calculations of 54 atoms SQS supercells for polycrystalline solid solutions (Hill-averaged).

3.2.5 Voronoi tessellation and clusters analysis

Fig. 3.21 illustrates the distribution of icosahedral structures in AIMD-simulated materials, specifically full- ($\langle 0\ 0\ 12\ 0\ 0 \rangle$) and *quasi*-icosahedra, in both ZnZr and ZnMg amorphous alloys. The *quasi*-icosahedra, named with the indices such as $\langle 0\ 2\ 8\ 1\ 0 \rangle$, $\langle 0\ 2\ 8\ 2\ 0 \rangle$, and $\langle 0\ 1\ 10\ 2\ 0 \rangle$, identify slightly distorted icosahedra which exhibit structural similarities to full-icosahedra among various polyhedral structures as suggested by Guo [38]. In the experimental range of amorphous compositions for ZnMg, a nearly linear increase in the fraction of Zn-centered full and *quasi*-icosahedra was observed, while the fraction of Mg-centered clusters remains lower than 2.5 %

with the addition of Zn. In the case of ZnZr alloys within the Zn concentration range of 25 to 45 at. %, the population fraction of Zn- and Zr-centered clusters shows values in the range around 20% and lower than 5%, respectively. As more Zn is added, the fraction of Zn-centered clusters decreases to values between 7% and 15%, while Zr-centered polyhedra are completely absent when Zn contents exceed 55 at.%.

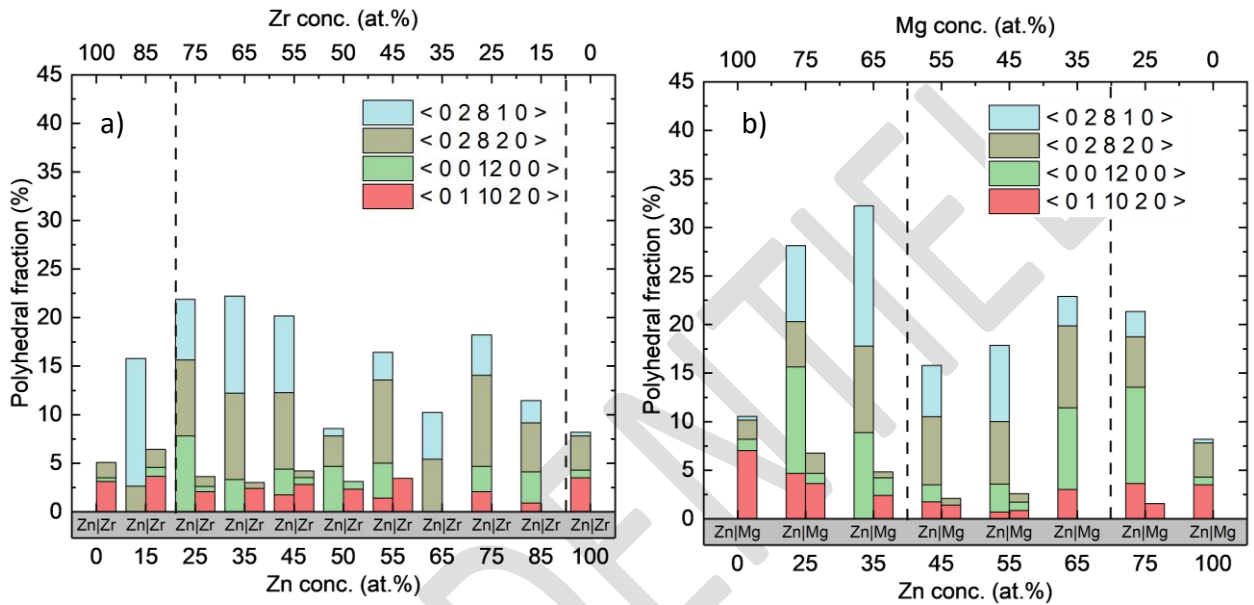


Fig. 3.21 Polyhedral fraction full and quasi-icosahedra present in the simulated cell of ZnZr and ZnMg alloys. For each composition, one pair of column is displayed: the left columns represent the polyhedral fraction of Zn-centered clusters, while the right columns represent Zr- or Mg-centered clusters. The dashed lines highlight the glass-forming compositional range found experimentally, but it is worth to notice that all the simulated compositions are amorphous.

3.2.6 Tensile tests on Kapton®

The cracking behavior during tensile tests of some compositions of ZnZr and ZnMg TFMGs deposited on polymeric (Kapton®) substrates was analyzed to gain further insights into the mechanical properties of the films. **Fig. 3.22** and **Fig. 3.23** show top-view confocal microscope images of the ZnZr and ZnMg surfaces, respectively, during the tensile tests. Ductile features, such as crack-blocking phenomena and crack deviations were observed during the nucleation of the first crack on crystalline Zn_4Zr_{96} film and similar values of crack initiation strains were observed for amorphous

samples. In contrast, Zn-rich film showed a significantly higher density of crack for unit of length, and the cracks were straight and propagated throughout the entire length of the sample, highlighting a more brittle behavior.

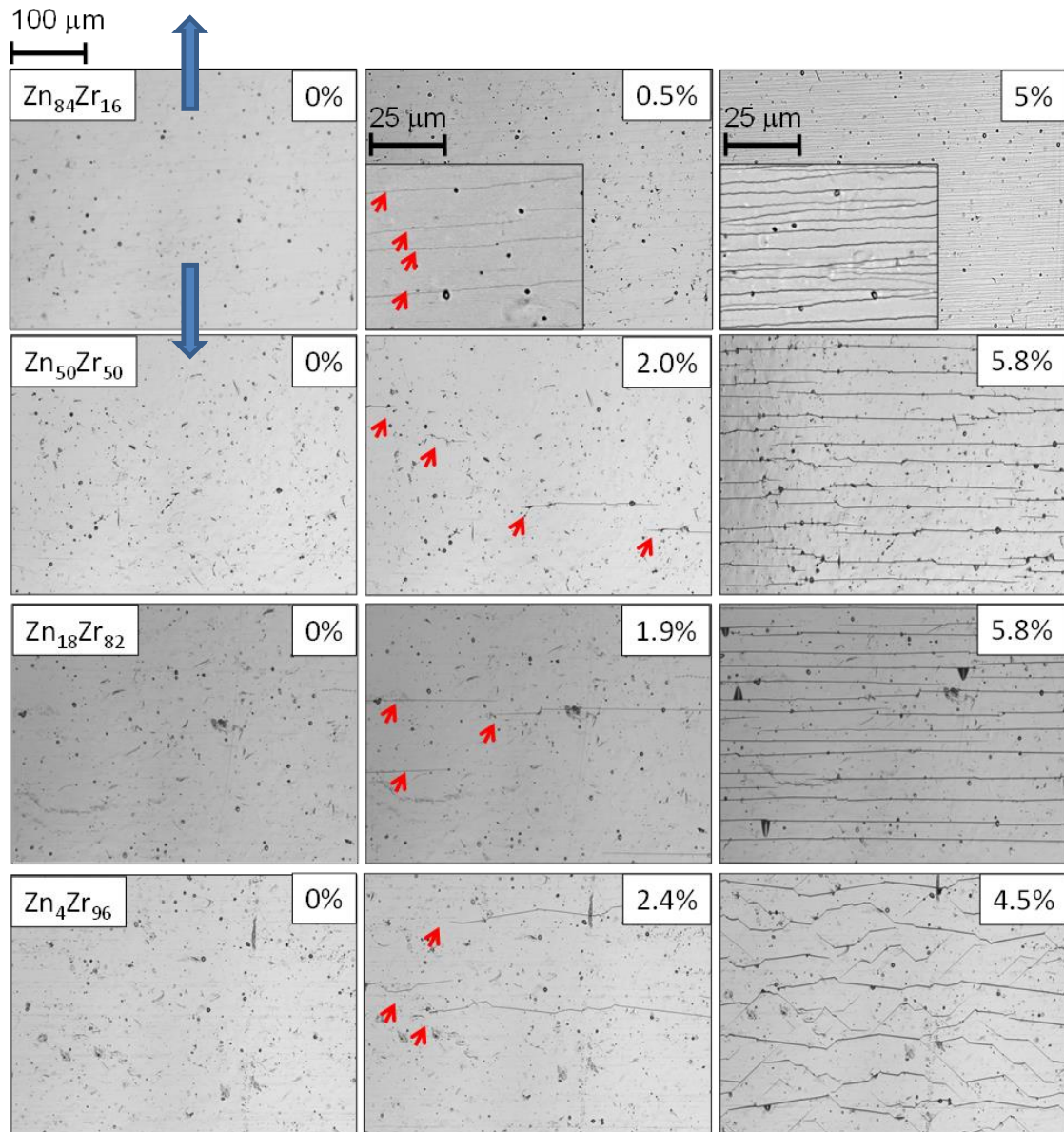


Fig. 3.22 Confocal images of top view of 400 nm-thick ZnZr TFMGs deposited on Kapton® during tensile test. All the images have been taken with 10x zoom. The blue arrows indicate the traction direction while the red arrows in the images highlight the cracks.

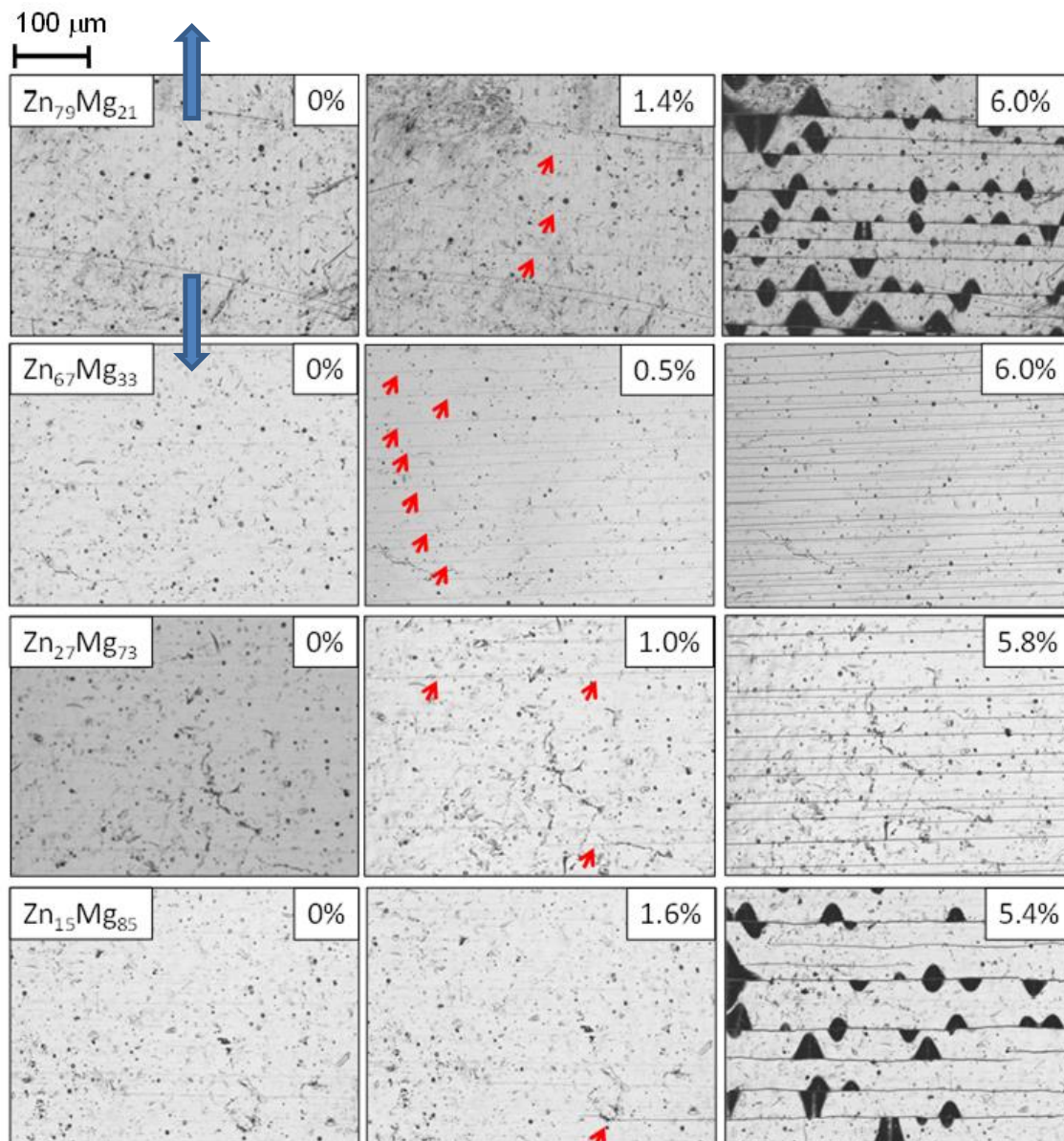


Fig. 3.23 Confocal images of top view of 700 nm-thick ZnMg TFMGs deposited on Kapton® during tensile test. All the images have been taken with 10x zoom. The blue arrows indicate the traction direction while the red arrows in the images highlight the cracks.

Fig. 3.24 represents the values of crack initiation strain and crack saturation density. In addition, the crack initiation strain could be used as an estimation for the lowest value of elastic strain of the material. The appearance and morphology of the first crack provide valuable information regarding the film's ductile or brittle behavior. Films with high toughness exhibit crack-blocking or crack-deflection phenomena, resulting in discontinuous cracks. This behavior was observed in ZnZr films when the crack

initiation strain was equal to or greater than 1.9%. However, the Zn-richest film ($\text{Zn}_{84}\text{Zr}_{16}$) exhibited a high density of straight cracks propagating throughout the entire sample length, indicating a brittle behavior. In comparison to ZnZr, ZnMg films displayed a less damage-tolerant behavior, evident from the lower values of crack initiation strain ranging from 0.5% to 1.6%. Moreover, amorphous samples exhibited the lowest crack initiation strain (0.5%), indicating the most brittle behavior. These results are coherent with the measured values of crack saturation density which are inversely proportional to the spacing within cracks confirming a lower toughness of the material [39, 40].

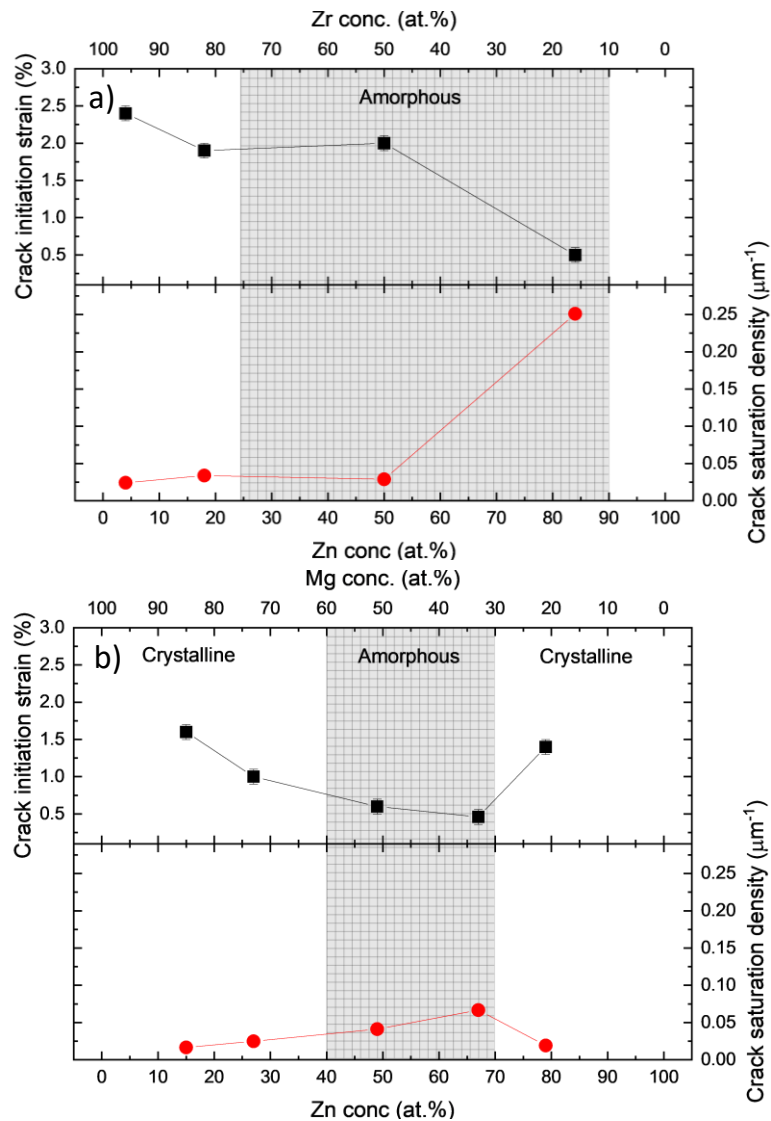


Fig. 3.24 Crack initiation strain and crack saturation density as function of the composition for a) ZnZr and b) ZnMg thin films.

3.3 Discussion

3.3.1 Glass forming ability, atomic distances and bonds fractions

In terms of incident ion energy, Zn demonstrates a sputtering yield that is four times higher than that of Zr. However, as shown in **Fig. 3.7**, during the deposition process, ZnZr TFMGs exhibit a chemical composition close to $Zn_{50}Zr_{50}$ when the target's power ratio approaches 1 (within the range of 75-100 W). This is due to the fact that the Zr target was already partially eroded because of previous depositions; the surface area in contact with the plasma was increased, leading to a larger number of incident ions and sputtered atoms. On the other hand, in order to deposit $Zn_{50}Mg_{50}$, a target power ratio greater than 1 (approximately 1.7) was required, highlighting the higher sputtering yield of Mg compared to Zn under the described deposition parameters in Section 2.2. The GFA of ZnZr and ZnMg alloys was assessed both thermodynamically and experimentally. Overall, the ZnZr system demonstrated a superior GFA, closely aligned with the predicted compositional range of 24-95 at. % Zn. Contrarily, the GFA of ZnMg alloys found experimentally was limited to a narrower compositional range of 45-67 at. % Zn, in contrast to the wider range (20-90 at. %) predicted thermodynamically. Moreover, ZnMg elements show a reduced enthalpy of mixing (-4 kJ/mol) compared to ZnZr (-29 kJ/mol). Nevertheless, in alloys with small negative enthalpy of mixing, there are limitations of the thermodynamic model employed to explain the amorphous phase formation [41].

The XRD analysis of ZnZr and ZnMg alloys revealed a clear crystalline-to-amorphous transition. In the crystalline compositional range, the Zr-rich nanocrystalline films exhibited the formation of HCP solid solutions, while in ZnMg alloys the Zn- and Mg-rich films displayed the presence of segregated Zn and Mg, respectively, probably attributed to the lower enthalpy of mixing of Zn-Mg compared to Zn-Zr. Considering the atomic radii of pure crystalline Zn, Zr, and Mg, which are approximately 138, 158, and 160 pm, respectively [42], the difference in atomic radii between Zn and Mg atoms results similar to the Zn and Zr one ($\Delta r_{Zn-Mg} \sim \Delta r_{Zn-Zr}$). Hence, it is expected that the position and shift of the PDP in XRD diffractograms of amorphous compositions is consistent for both systems. However, ZnMg films display the characteristic amorphous PDP with a more asymmetric character and surprisingly higher angles (45-

48°) and this skewness in PDP observed for $Zn_{45}Mg_{55}$, $Zn_{46}Mg_{54}$, and $Zn_{49}Mg_{51}$ might be related to the presence of nanocrystallites. Moreover, the shift in positioning of the PDP of both ZnZr and ZnMg TFMGs is related to a reduction in d_{av} resulting from the introduction of Zn (from 305 to 275 pm and from 290 to 275 pm, respectively). To better understand the physical phenomenon that influences the shortening of d_{av} in ZnZr and ZnMg TFMGs upon Zn addition, the partial pair distribution functions (PPDFs) are investigated (**Fig. 3.25**) highlighting the atomic distance of each bond pairs (Zr-Zr, Mg-Mg, Zr-Zn, Mg-Zn and Zn-Zn) in the first coordination shell and providing valuable information regarding the short-range order.

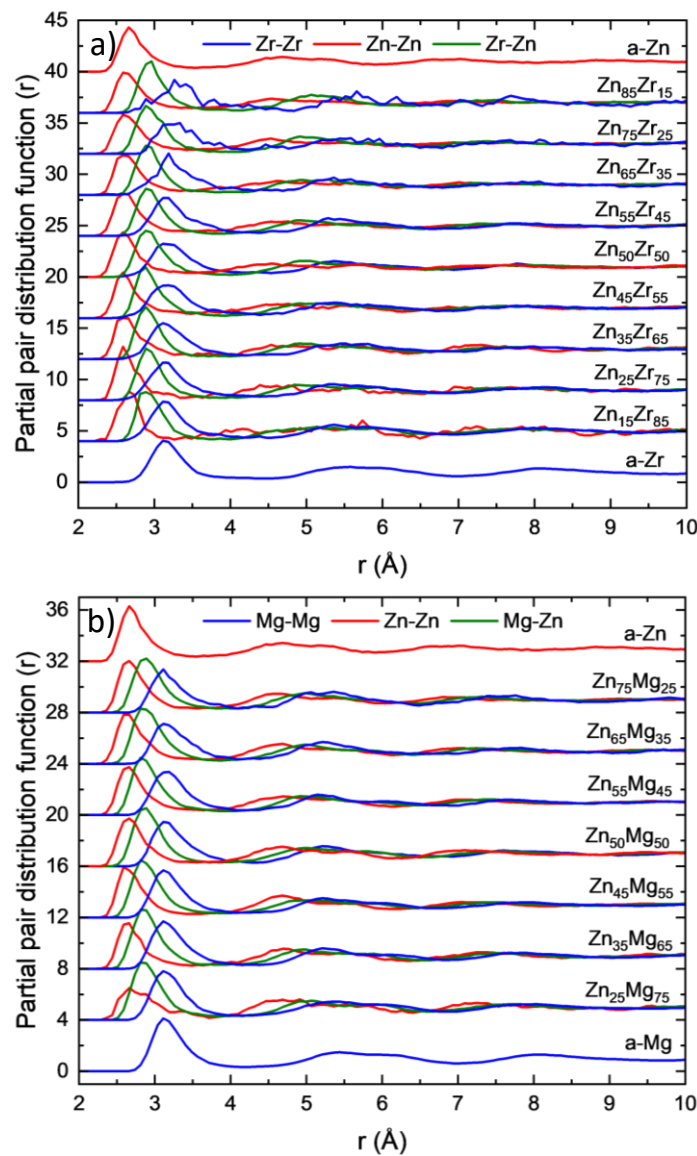


Fig. 3.25 Partial pair distribution functions (PPDFs) of a) ZnZr and b) ZnMg amorphous alloys.

Fig. 3.26 represents each atomic pair distance as function of the Zn content for both ZnZr and ZnMg amorphous alloys. It is visible that ZnZr TFMGs show a nearly constant value of d_{av} (290-295 pm) in the interval of composition between 45% and 65% at. Zn. In this compositional range, the values of d_{av} are in good agreement with the atomic distances of the pair Zn-Zr, suggesting the favored formation of heterometallic bonds (Zn-Zr) compared to the homometallic ones (such as Zr-Zr or Zn-Zn). Moreover, it is evident from **Fig. 3.14** that the choice of atomic radii of the pure elements is crucial for the Zen's law reliability. In particular, it is found that the predicted values by considering Zen's law assuming the atomic radii of fully amorphous pure elements (predicted by *ab initio* methods) lead to better agreement with experimental results than those predicted assuming the atomic radii of crystalline elements. In addition, it was found that the elastic moduli of pure virtual a-Zr can significantly differ from these of its polycrystalline counterpart, as reported for other binary Zr-(Co, Ni, Cu) alloys [37]. Therefore, for the purpose of averaging, such as in the calculation Zen's law, it is worthwhile to consider the atomic radius calculated for amorphous structures instead of crystalline ones.

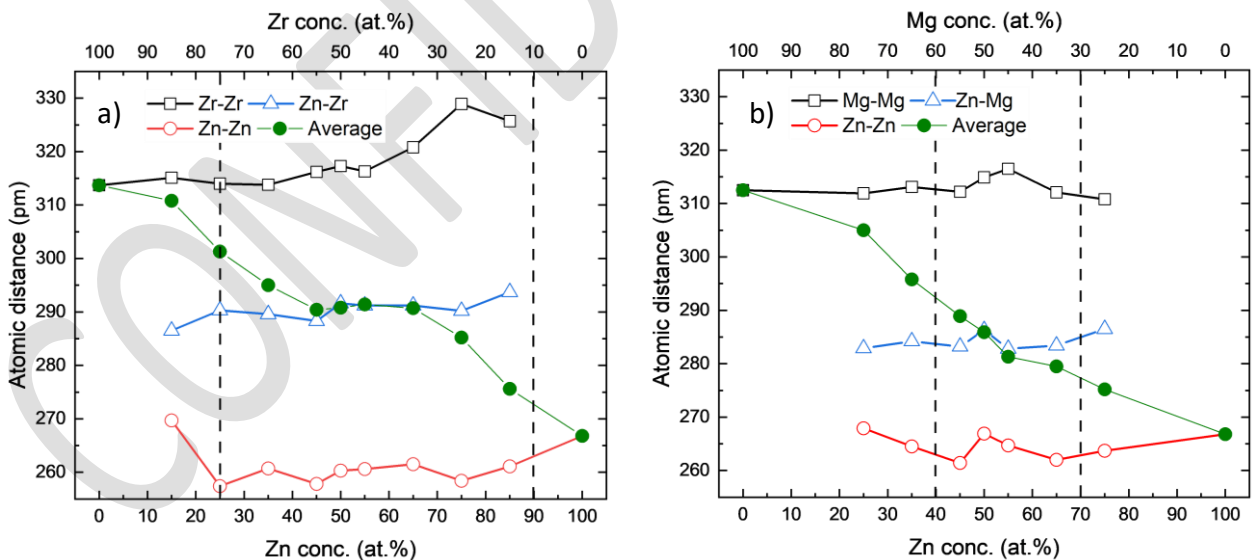


Fig. 3.26 Atomic pairs distances (Zr-Zr, Zn-Zr, Zn-Zn) and average interatomic distances of a) ZnZr and b) ZnMg as function of Zn content calculated by *ab initio* methods.

To quantify the formation of heterometallic bonds (Zn-Zr or Zn-Mg) compared to the formation of homometallic ones (Zn-Zn, Mg-Mg and Zr-Zr), the fraction of the different effective bonds in the structure was estimated analyzing the simulated glassy

structures from AIMD methods. The distributions of bond pair lengths are depicted in **Fig. 3.27**, and they were evaluated using a cutoff parameter of 3.7 Å, corresponding to the distance at the tail of the first peak in the PDF, in order to consider only the atomic pairs within the first coordination.

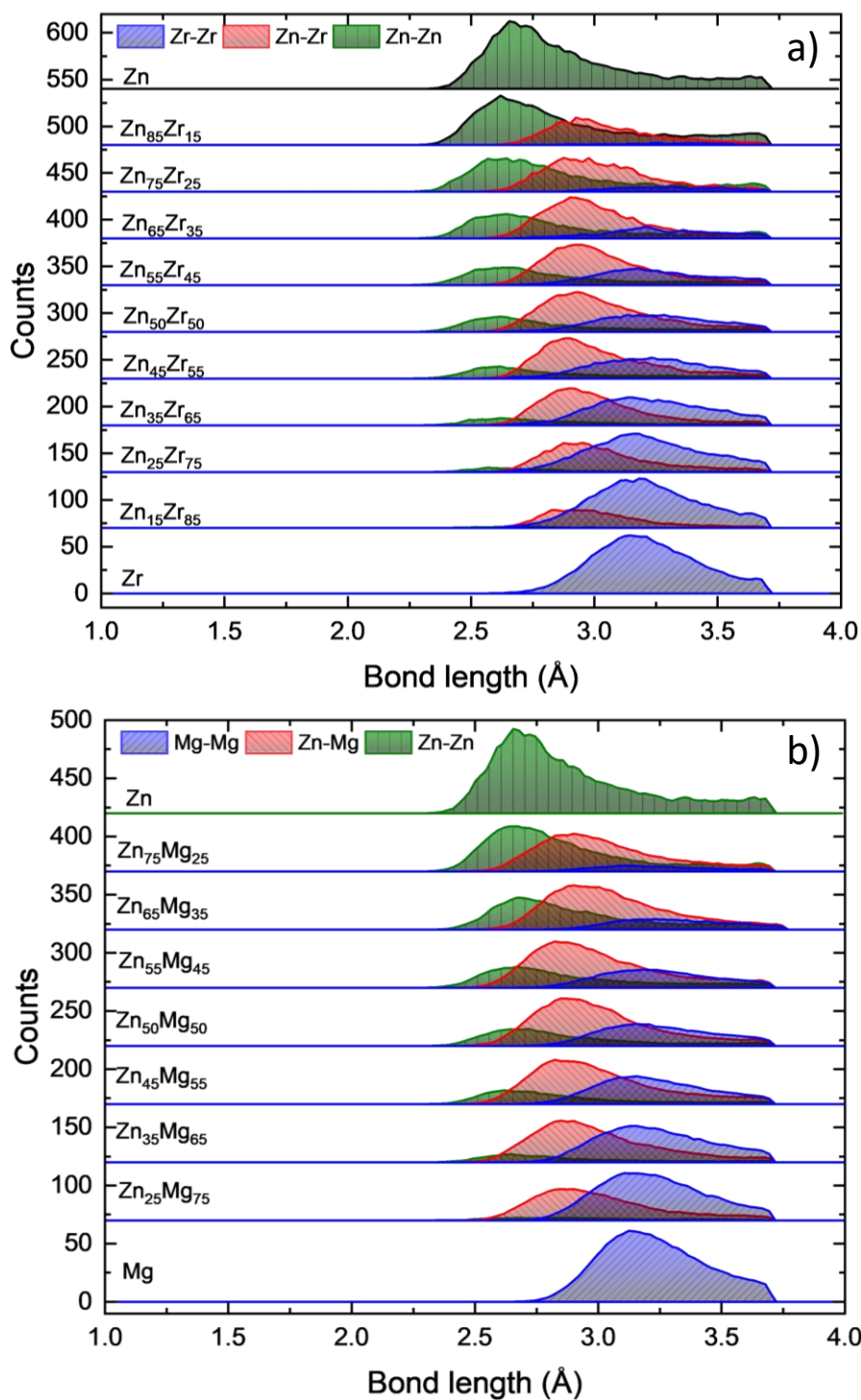


Fig. 3.27 Partial bond pair length for a) ZnZr and b) ZnMg TFMGs calculated by *ab initio* methods.

The resulting bond fractions are shown in **Fig. 3.28** and are consistent with what has been found in ZrCu MGs [43], indicating a maximum in packing efficiency [29, 30] between 50 and 60 at.% Zn for both systems. Considering x_{Zn} as the atomic fraction of Zn and the material made of spheres, the statistical probability to find Zn-Zn, Zr-Zr and Zn-Zr bond pairs in the whole volume (effective and not effective ones) is given by the multiplied probabilities x_{Zn}^2 , $(1 - x_{Zn})^2$ and $2x_{Zn}(1 - x_{Zn})$, respectively. Hence, to analyze the fractions of each effective bond pair in amorphous ZnZr and ZnMg, they were fitted by a second-order polynomial with the two imposed conditions for each pure element (at $x_{Zn}=0$ and $x_{Zn}=1$). The obtained results are as follows:

$$\begin{aligned}
 f_{Zn-Zn}^{(ZnZr)} &= -0.17x_{Zn} + 1.17x_{Zn}^2 \\
 f_{Zn-Zr}^{(ZnZr)} &= 2.07x_{Zn} - 2.07x_{Zn}^2 \\
 f_{Zr-Zr}^{(ZnZr)} &= 1.00 - 1.9x_{Zn} + 0.90x_{Zn}^2 \\
 f_{Zn-Zn}^{(ZnMg)} &= -0.22x_{Zn} + 1.22x_{Zn}^2 \\
 f_{Zn-Mg}^{(ZnMg)} &= 2.15x_{Zn} - 2.15x_{Zn}^2 \\
 f_{Mg-Mg}^{(ZnMg)} &= 1.00 - 1.93x_{Zn} + 0.93x_{Zn}^2
 \end{aligned} \tag{31}$$

The deviations from ideality in the obtained results are due to differences in the local chemical order in the first shell of atomic coordination compared to the whole volume of the material.

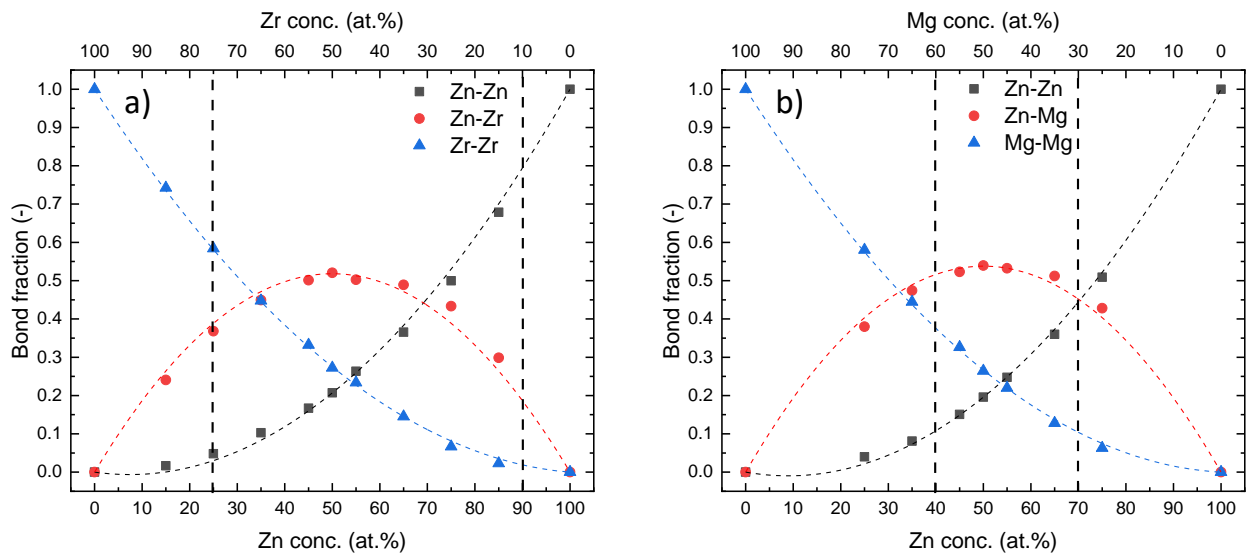


Fig. 3.28 Bond pair fraction of Zn-Zn, Zn-Mg, Zn-Zr, Zr-Zr and Mg-Mg of a) ZnZr and b) ZnMg metallic glasses. The dashed colored lines illustrate the polynomial fits, while the vertical ones represent the border of the amorphous-to-crystalline transition found experimentally. All the AIMD-simulated compositions are amorphous.

Finally, to gain a deeper understanding of the short-range order (SRO) pertaining to atomic packing, Voronoi tessellation analysis was employed. Previous research [30, 44, 45] has established a correlation between the highest occurrence of full-icosahedra $\langle 0\ 0\ 12\ 0\ 0 \rangle$ and the glass-forming ability (GFA) in metallic glasses. Additionally, this unique atomic coordination has also been associated with superior shear resistance [46, 47] and thermal stability [29] in metallic glasses. The absence of Zr-centered full- and *quasi*-icosahedra in ZnZr MGs for Zn content higher than 55 at. %, corresponding to the plateau observed in elastic moduli, can be attributed to a rearrangement of Zr atoms and alterations in their atomic coordination, indicating a transition in the structural and elastic response.

Notably, a recent study conducted on ZrCuAl metallic glasses demonstrated that large packing efficiency lead to improved GFA [48]. Hence, low-volume clusters contribute to enhanced GFA by increasing mass density and stabilizing the amorphous structure. Thus, in the present study, it is anticipated that Zn-centered clusters play a pivotal role in the GFA of ZnZr and ZnMg alloys. The cluster volumes are represented in **Fig. 3.29**. Zn-centered clusters exhibit a consistent volume of approximately 15.5 \AA^3 in both systems. Despite Zr and Mg atoms having similar atomic radii, the volume of Zr-

centered clusters remains compositionally independent and equals 23 \AA^3 , whereas the volume of Mg-centered clusters decreases from 24 to 22 \AA^3 with the addition of Zn. Additionally, this unique atomic coordination of $\langle 001200 \rangle$ icosahedra has also been associated with superior shear resistance [46, 47] and thermal stability [29] in metallic glasses. The absence of Zr-centered full- and *quasi*-icosahedra in ZnZr MGs for Zn content higher than 55 at. %, corresponding to the plateau observed in elastic moduli, can be attributed to a rearrangement of Zr atoms and alterations in their atomic coordination, indicating a transition in the structural and elastic response.

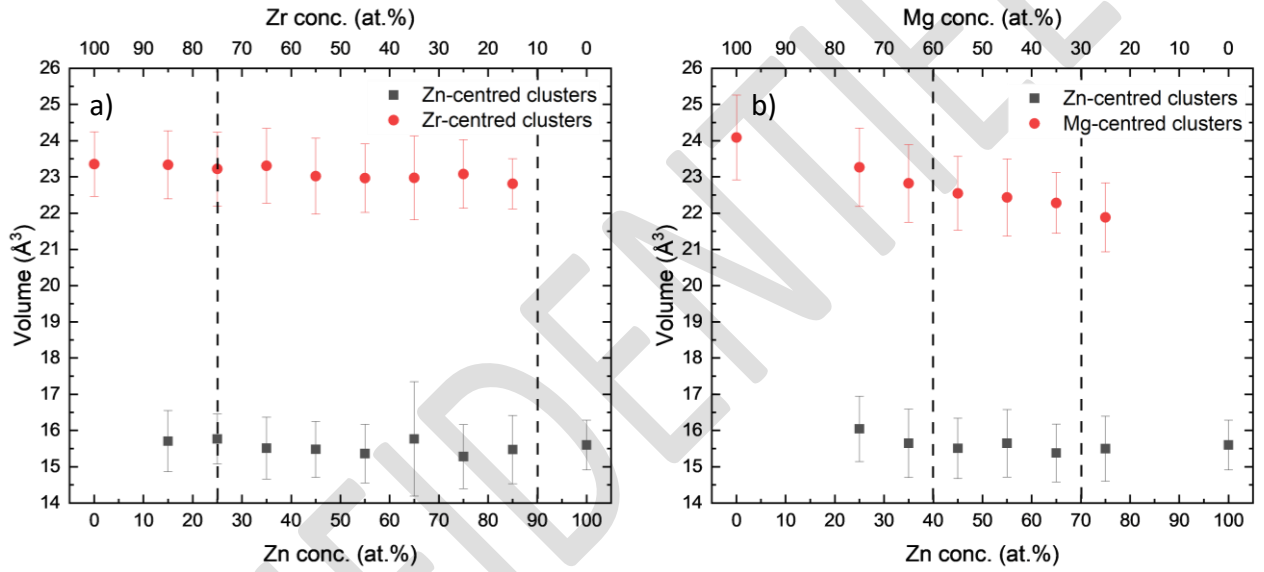


Fig. 3.29 Cluster volume for ZnZr and ZnMg amorphous alloys. The dashed lines represent the border of the amorphous-to-crystalline transition found experimentally. All the AIMD-simulated compositions are amorphous.

3.3.2 Mechanical properties: hardness, yield strength and elastic strain

The dependence on packing factor and atomic diameter allows inferring that ΔS^δ is associated with the local order of the material. Moreover, high values of mismatch entropy can result in a dense random packed structure [49]. Therefore, ΔS^δ is linked to physical properties that are greatly influenced by the local atomic arrangement [41]. For instance, the “bell-shape” trend observed in hardness as function of Zn content in ZnZr and ZnMg TFMGs (**Fig. 3.15**) was also observed in FWHM, crystallization temperature and hardness of ZrCu TFMGs [41, 50, 51] which was related to the maximum of mismatch entropy [41] and packing efficiency [29, 30] caused by the

maximum fraction of heterometallic bonds (**Fig. 3.28**) confirmed by MD approaches [43].

The high crack density observed in tensile test on Kapton® of Zn-rich ZnZr TFMGs could be attributed to lower material toughness or other factors, such as adhesion with the polymeric substrate or stress concentration around existing defects [39]. Nevertheless, the lower hardness was measured for the Zn-richest film. The yield strength (proportional to the hardness) and elastic strain can give an estimation of the Young's modulus through the formula:

$$E = \frac{\sigma_y}{\varepsilon_l} \quad (32)$$

The elastic strain measured by tensile test on Kapton® (assuming a purely linear elastic behavior of metallic glasses) and the Young's modulus values estimated with **Equation (30)** are compared with those measured experimentally by BLS in **Table 3.2**. The measured and estimated elastic modulus values for fully nanocrystalline and fully amorphous films exhibit satisfactory agreement, while the composite film values indicate a significantly higher estimated Young's modulus. This discrepancy could be attributed to the existence of a nanocrystalline phase within the film or inconsistencies at the Kapton® interface, potentially functioning as stress concentration points and leading to diminished elastic deformation, notably in the case of the Zn-richest ZnZr film. Nevertheless, the diffractogram of the Zn₈₁Zr₁₉ film exhibited signs of a nanocomposite structure, such as an asymmetric PDP due to minor peaks in the broad hump and at 85°. These findings suggest that the structure of the Zn₈₄Zr₁₆ film is also likely nanocomposite. Moreover, the asymmetrical, broad, and flat PDP in the diffractograms of ZnMg alloys also implies the presence of nanocrystalline phases.

Table 3.2 Elastic strain values measured by tensile test on Kapton® substrates and estimated by using **Equation (30)** for ZnZr and ZnMg films.

| <i>Composition</i> | <i>Young Modulus (GPa)</i> | |
|--|----------------------------|---|
| | <i>Measured (BLS)</i> | <i>Estimated (σ_y/ϵ_l)</i> |
| Zn ₄ Zr ₉₆ | 94 ± 4 | 76 ± 10 |
| Zn ₁₈ Zr ₈₂ | 79 ± 3 | 93 ± 12 |
| Zn ₅₀ Zr ₅₀ * | 93 ± 4 | 101 ± 15 |
| Zn ₈₄ Zr ₁₆ [†] | 93 ± 4 | 260 ± 23 |
| Zn ₁₅ Mg ₈₅ | 52 ± 2 | 58 ± 9 |
| Zn ₂₇ Mg ₇₃ [†] | 57 ± 2 | 138 ± 18 |
| Zn ₄₉ Mg ₅₁ [†] | 67 ± 3 | 231 ± 22 |
| Zn ₆₇ Mg ₃₃ [†] | 74 ± 3 | 293 ± 26 |
| Zn ₇₉ Mg ₂₁ | 70 ± 3 | 72 ± 9 |

Note: *PDPs in XRD are symmetric; [†]PDPs in XRD are asymmetric or composite amorphous/crystalline material; label-free compositions represent fully nanocrystalline films.

3.3.3 Elastic moduli

Despite the trends of Young's modulus measured by nanoindentation and BLS are in good agreement, a discordance of ~20% in their values is observed, with a stiffer one obtained by nanoindentation, as observed as well in Refs [10, 52, 53]. This observation may be due to several reasons: nanoindentation is a semi-destructive technique and thus there are phenomena occurring during the deformation of the material (pile-up or sink-in) which overestimate the elastic modulus and cause an apparent stiffening [54, 55]. Nevertheless, underestimation of hardness is also not excluded, the existence of a geometric constraint at the nanoscale, like the bonded film interface, may help to suppress shear-band nucleation through the development of hydrostatic pressure in the film [56]. Another possible cause of the overestimation of elastic modulus in nanoindentation could be the existence of internal stresses [57, 58] and a contribution of the substrate within the elastic interaction volume beneath the tip [58], a phenomenon even more important in the case of high-strength films like metallic glasses. For the aforementioned reasons, BLS results are assumed more accurate for later extrapolation of elastic moduli of virtual pure amorphous elements. However, the trends of experimentally measured elastic moduli in the amorphous region are similar

and expected to fall within the two AIMD+DFT calculated bounds, with the unrelaxed and relaxed case, providing the stiffer and softer value, respectively [10].

In nanocrystalline Zr-rich films, the decrease in E and G cannot be predicted using a Vegard's rule which is more applicable to segregated systems. This softening is linked to the lower moduli of the solid solution phase (Zr-Zn HCP), as predicted by SQS+DFT methods, and/or to the mechanical instability of a metastable solid solution that is supersaturated in Zn [37, 59, 60]. In the glass-forming compositional range of ZnZr, the shortening of d_{av} lead to the stiffening of the material which reach a plateau for Zn content larger than 55 at. %, while this behavior was not observed for elastic moduli of ZnMg TFMGs which increase monotonically. To understand the reasons for this different mechanical behavior of the two systems, the trend of elastic moduli has been fitted associating different elastic modulus contributions to each atomic bond pair. For example, in case of Young's modulus E for ZnZr, we named E_{Zn-Zn} , E_{Zr-Zr} the Young's moduli of the two homometallic bonds, and E_{Zn-Zr} the Young's modulus of the heterometallic bond, which can form in the glassy alloy. Hence, averaging the elastic contributions by the fraction of each bond pair ($f_{Zn-Zn}^{(ZnZr)}$, $f_{Zr-Zr}^{(ZnZr)}$ and $f_{Zn-Zr}^{(ZnZr)}$) and following the Voigt-Reuss-Hill homogenization [8, 12, 13], we have the relations:

Voigt:

$$E_{tot}^V = f_{Zn-Zn}^{(ZnZr)} E_{Zn-Zn} + f_{Zr-Zr}^{(ZnZr)} E_{Zr-Zr} + f_{Zn-Zr}^{(ZnZr)} E_{Zn-Zr} \quad (33)$$

Reuss:

$$\frac{1}{E_{tot}^R} = \frac{f_{Zn-Zn}^{(ZnZr)}}{E_{Zn-Zn}} + \frac{f_{Zr-Zr}^{(ZnZr)}}{E_{Zr-Zr}} + \frac{f_{Zn-Zr}^{(ZnZr)}}{E_{Zn-Zr}} \quad (34)$$

This model considers the constant and compositional-independent elastic contributions of the different atomic pairs, which is supported by the nearly-constant atomic pair distances for different compositions represented in **Fig. 3.26**.

The values of the elastic parameters for homogeneous bonds in the glassy state (E_{Zn-Zn} and E_{Zr-Zr}) were evaluated starting from calculated values by DFT ± 10 GPa and from literature for Zr-Zr [37], while for heterogeneous bonds the elastic parameter E_{Zn-Zr} was used as free parameter in the fit and the results are listed in **Table 3.3**.

Table 3.3 Values of elastic parameters E and G obtained by fitting effective elastic moduli with the 3-bonds model of a binary alloys.

| <i>Atomic pair</i> | <i>Voigt</i> | | <i>Reuss</i> | |
|--------------------|--------------|------------|--------------|------------|
| | E (GPa) | G (GPa) | E (GPa) | G (GPa) |
| Zn-Zn | 84 ± 2 | 33 ± 1 | 84 ± 1 | 32 ± 1 |
| Zn-Zr | 123 ± 3 | 43 ± 1 | 147 ± 9 | 50 ± 3 |
| Zr-Zr | 42 ± 4 | 16 ± 2 | 57 ± 2 | 21 ± 1 |
| Zn-Mg | 72 ± 1 | 26 ± 1 | 76 ± 2 | 27 ± 1 |
| Mg-Mg | 40 ± 3 | 16 ± 2 | 47 ± 2 | 18 ± 1 |

The Reuss model was found to better fit E and G of amorphous Zr. The same analysis was carried out for shear modulus (G) of ZnZr and elastic moduli of ZnMg TFMGs. It is visible that the main difference in ZnZr and ZnMg TFMGs is given by the heterometallic bond contribution: for ZnZr this contribution results larger than the homometallic ones, while for ZnMg it falls in the average of the two homometallic bonds. This suggests an intrinsic difference in the heterometallic bond strength due to the different electronic configuration, highlighted by the complete d electronic orbitals in Zn (Ar $3d^{10} 4s^2$), in contrast to the incomplete one of Zr (Kr $4d^2 5s^2$). To assess the intrinsic electronic differences between Zn-Mg and Zn-Zr bonds, we conducted a density of states analysis for $Zn_{50}Zr_{50}$ and $Zn_{50}Mg_{50}$, and the results are presented in **Fig. 3.30**. The analysis revealed a significant hybridization between Zn- p and Zr- d electronic orbitals in the energy range between -2eV to 0eV that still extend beyond the Fermi energy. Moreover, when comparing the Zn- d energetic level of ZnZr with the ZnMg system, a noticeable shift towards lower energy was observed.

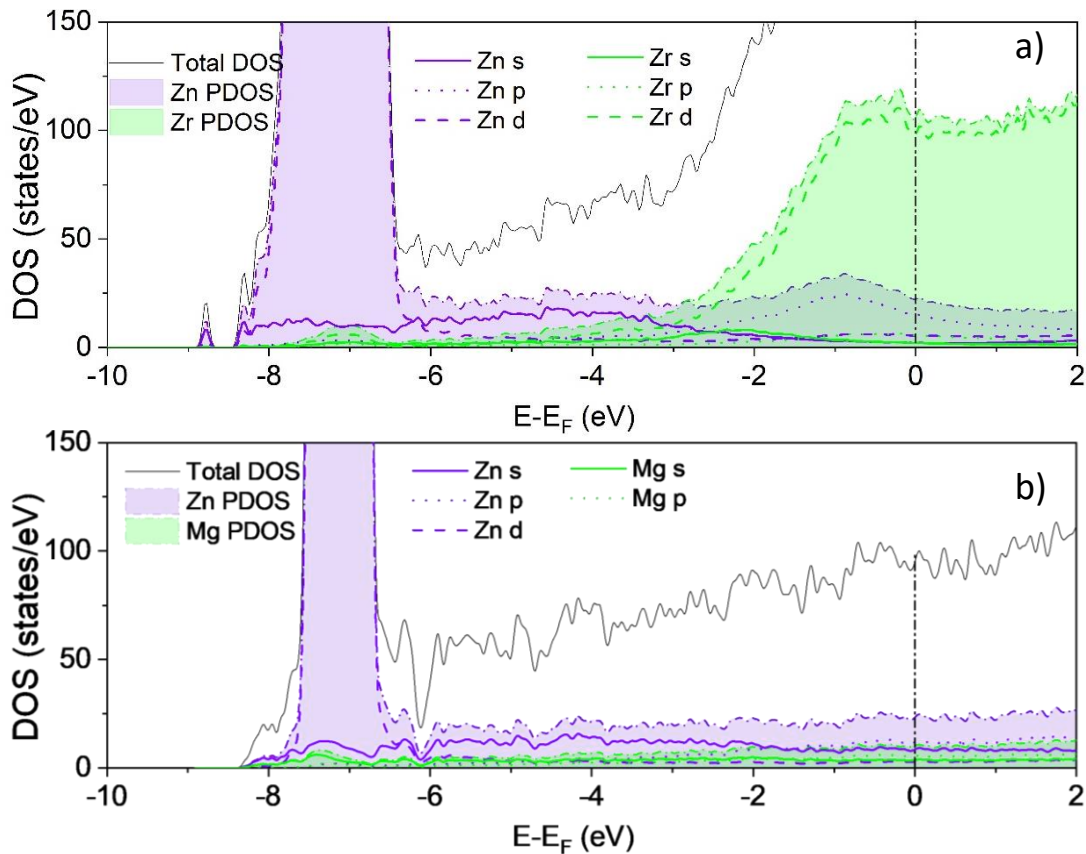


Fig. 3.30 Total (TDOS) and projected (PDOS) density of electronic states of a) $\text{Zn}_{50}\text{Zr}_{50}$ and b) $\text{Zn}_{50}\text{Mg}_{50}$ alloys.

3.3.4 Static immersion test of ZnMg and ZnZr alloys

The preliminary investigation of the biodegradation behaviour of ZnMg and ZnZr alloys was investigated by static immersion test in SBF at 37 °C and SEM-imaging the surface of the sample after static immersion test for 1 and 8 weeks in SBF at 37 °C. **Fig. 3.31** displays the top-view of the typical aspect of few ZnMg and ZnZr films after deposition and after 1 and 8 weeks of immersion in SBF. It is visible that all ZnMg films are more susceptible to corrosion compared to ZnZr films. After one week, the ZnMg films are prematurely cracked and delaminated, revealing the uncovered Si substrate. Furthermore, the film debris have a minimum size around 10-20 μm up to several hundreds of microns. On the other hand, the ZnZr films does not show any phenomenon of cracking and/or delamination and they look still adherent on the surface even after 8 weeks of immersion, with the exception of the Zn-richest film ($\text{Zn}_{84}\text{Zr}_{16}$) which show cracks and corrosion product at the edges of the sample. The

degradation behavior of ZnMg resulted unsatisfactory because of the delamination films occurred after one week with debris size about ~100-200 μm . Similarly to MgZr presented in Section , the samples containing Mg are the most susceptible to corrosion, while the Zr-rich samples resulted the most resistant.

CONFIDENTIEL

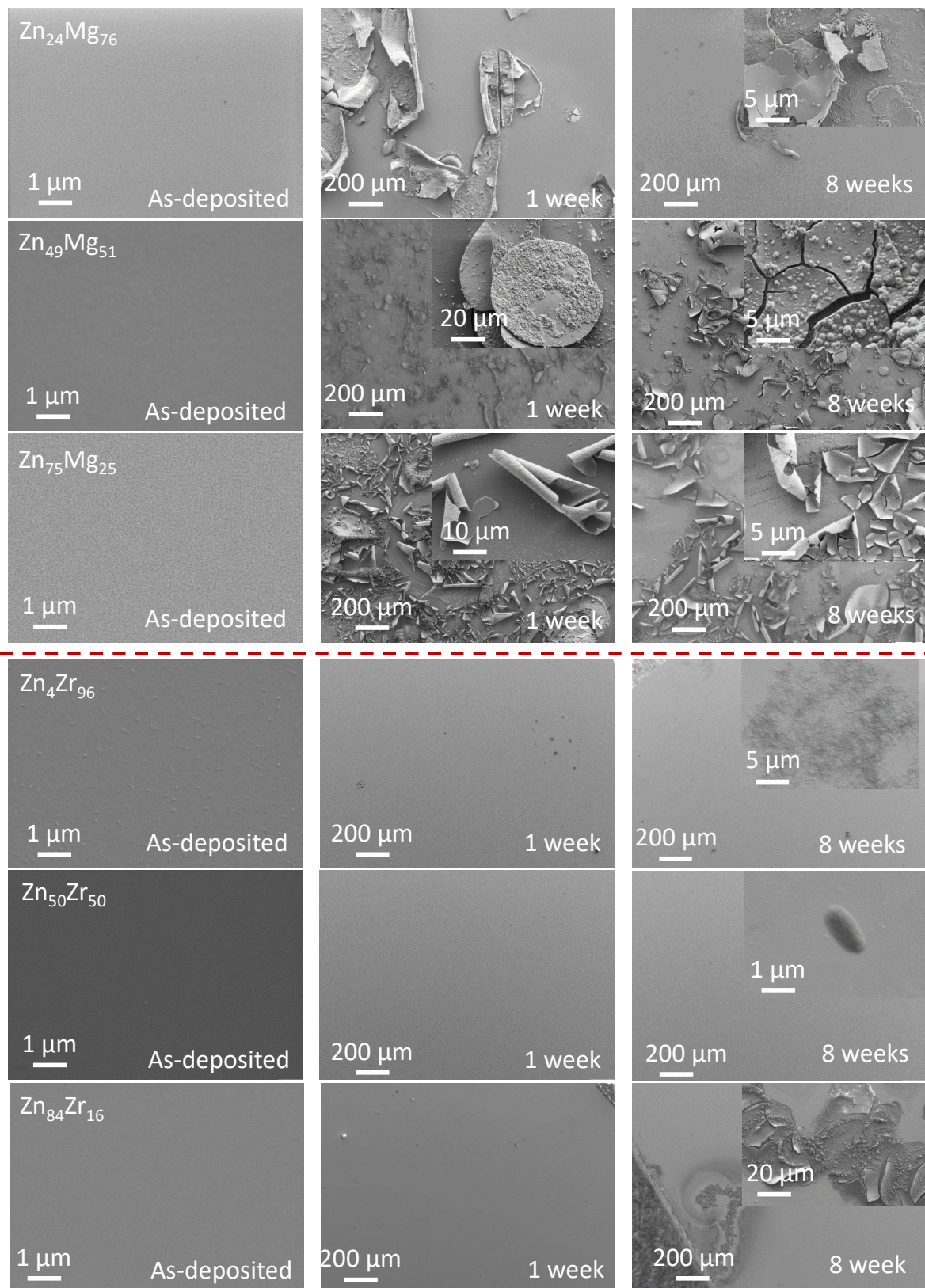


Fig. 3.31 Top-view of ZnMg and ZnZr films as-deposited, after 1 and 8 weeks of immersion in SBF at 37 °C. The red dashed line separates the ZnMg from ZnZr films.

3.3.5 Summary and conclusion

Several compositions of ZnZr and ZnMg films were deposited by magnetron co-sputtering and characterized to investigate the effect of composition on the atomic structure and mechanical properties. Additionally, first principles calculations (AIMD/SQS and DFT) were used to get a deeper insight on atomic position and related elastic properties. It was concluded that:

- Both ZnZr and ZnMg alloys showed different glass-forming compositional ranges. Amorphous films of ZnZr were found for Zn content ranging from 26 to 88 at. %, while ZnMg TFMGs were found for limited composition range within 45 and 67 at. % Zn but with nanocrystallites embedded in the amorphous matrix.
- The addition of Zn is responsible for the decreasing of average interatomic distances from 305 to 275 pm in ZnZr and from 290 to 280 pm in ZnMg TFMGs. Both AIMD and experimental results proved the presence of a plateau in average atomic distances of ZnZr TFMGs at 290 pm for Zn content within 45 and 65 at. % in connection with favored formation of heterometallic ZnZr bonds and corresponding in a rearrangement of Zr-centered clusters, while d_{av} of ZnMg decreased monotonically.
- The hardness of ZnZr and ZnMg films shows the maximum value in the glass-forming compositional range which is related to the maximum of mismatch entropy (and packing efficiency) and maximum fraction of heterometallic bonds.
- The elastic moduli measured experimentally with different techniques were compared with DFT-calculated ones showing satisfactory trends. Elastic moduli of ZnZr TFMGs increase (~30%) by adding Zn from 26 to 45 at. % and for higher Zn content, the elastic modulus become constant at 100 GPa while elastic moduli of ZnMg TFMGs increase monotonically.
- The elastic contribution of heterometallic bonds for ZnZr resulted higher than the homometallic bonds, while the heterometallic bond for ZnMg falls in the average of the two homometallic bonds. The reason of this behavior might be related to the different electronic configuration of atoms, especially to the

presence of incomplete filled *d* orbitals in Zr and complete *d* for Zn which lead to *pd* electronic hybridization in ZnZr and a downward shift in the energy of Zn-*d* levels were observed when compared to ZnMg.

- The tensile tests of TFMGs deposited in polymeric substrates showed the lowest value of crack initiation strain in the amorphous compositional range for both ZnZr and ZnMg, highlighting the reduced damage-tolerance of metallic glasses compared to nanocrystalline phases. The values of crack initiation strain were assumed as elastic limit to estimate the Young's modulus, showing a good agreement for fully amorphous and fully nanocrystalline films. However, sample that were showing an asymmetric PDP or possible composite structure showed an "apparent" lower value, underestimating "the true" of elastic strain by a factor of 2-4. This might be related to stress concentration and cracks initiation at the nanocrystal/amorphous interface.
- The ZnMg films showed delamination after 1 week in SBF with macroscopic debris size, while ZnZr films did not show any delamination after 8 weeks of immersion.

In conclusion, in this chapter a wide range of composition were experimentally and computationally investigated and we provide a comprehensive understanding about the correlation between chemical composition, atomic structure and mechanical properties of both nanocrystalline (MgZr) and amorphous (ZnZr and ZnMg) alloys. In light of the preliminary results from the static immersion test, we assume that the introduction of Zr to ZnMg can effectively inhibit the corrosion, while the addition of Mg to ZnZr may enhance it. Consequently, these findings are necessity for the design of compositionally-tailored ZnMgZr TFMGs, which hold the potential for significant impact in specific biomedical applications.

3.4 References

- [1] H. Okamoto, Mg-Zr (magnesium-zirconium), *Journal of phase equilibria* 23(2) (2002) 198.
- [2] J.A. Thornton, The microstructure of sputter - deposited coatings, *Journal of Vacuum Science & Technology A: Vacuum, Surfaces, and Films* 4(6) (1986) 3059-3065.
- [3] K. Edalati, H. Emami, Y. Ikeda, H. Iwaoka, I. Tanaka, E. Akiba, Z. Horita, New nanostructured phases with reversible hydrogen storage capability in immiscible magnesium–zirconium system produced by high-pressure torsion, *Acta Materialia* 108 (2016) 293-303.
- [4] T. Maimaitiyili, A. Steuwer, J. Blomqvist, C. Bjerken, M.S. Blackmur, O. Zanellato, J. Andrieux, F. Ribeiro, Observation of the δ to ϵ Zr - hydride transition by in - situ synchrotron X - ray diffraction, *Crystal Research and Technology* 51(11) (2016) 663-670.
- [5] M. Latroche, P. Kalisvaart, P. Notten, Crystal structure of MgO. 65ScO. 35Dx deuterides studied by X-ray and neutron powder diffraction, *Journal of Solid State Chemistry* 179(10) (2006) 3024-3032.
- [6] G. Abadias, Stress and preferred orientation in nitride-based PVD coatings, *Surface and Coatings Technology* 202(11) (2008) 2223-2235.
- [7] P. Vermeulen, R. Niessen, D. Borsa, B. Dam, R. Griessen, P. Notten, Effect of the Deposition Technique on the Metallurgy and Hydrogen Storage Characteristics of Metastable Mg y Ti (1- y) Thin Films, *Electrochemical and solid-state letters* 9(11) (2006) A520.
- [8] P.F. Weck, E. Kim, V. Tikare, J.A. Mitchell, Mechanical properties of zirconium alloys and zirconium hydrides predicted from density functional perturbation theory, *Dalton Transactions* 44(43) (2015) 18769-18779.
- [9] S. Ganeshan, S. Shang, Y. Wang, Z.-K. Liu, Effect of alloying elements on the elastic properties of Mg from first-principles calculations, *Acta Materialia* 57(13) (2009) 3876-3884.
- [10] C. Poltronieri, A. Brognara, F. Bignoli, S. Evertz, P. Djemia, D. Faurie, F. Challali, C. Li, L. Belliard, G. Dehm, Mechanical properties and thermal stability of ZrCuAl_x thin film metallic glasses: Experiments and first-principle calculations, *Acta Materialia* 258 (2023) 119226.

- [11] C.H. Li, C. Poltronieri, G. Abadias, P. Djemia, Computational approach to identify structural and elastic relationship in metastable crystalline and amorphous alloy thin films: Mo_{1-x}Nix and Mo_{1-x}Six case studies, *Surface and Coatings Technology* (2023) 130168.
- [12] R. Hill, The elastic behaviour of a crystalline aggregate, *Proceedings of the Physical Society. Section A* 65(5) (1952) 349.
- [13] A.B. Behboud, A. Motallebzadeh, S. Özeriç, Nanoheterogeneous ZrTa metallic glass thin films with high strength and toughness, *Journal of Alloys and Compounds* 901 (2022).
- [14] S.N. Naik, S.M. Walley, The Hall–Petch and inverse Hall–Petch relations and the hardness of nanocrystalline metals, *Journal of Materials Science* 55(7) (2020) 2661-2681.
- [15] A.B. Behboud, A. Motallebzadeh, S. Özeriç, Nanoheterogeneous ZrTa metallic glass thin films with high strength and toughness, *Journal of Alloys and Compounds* 901 (2022) 163578.
- [16] T. Sawa, Correlation between nanoindentation test result and vickers hardness, *Proceedings of the IMEKO*, 2010, pp. 171-174.
- [17] P. Zhang, S.X. Li, Z.F. Zhang, General relationship between strength and hardness, *Materials Science and Engineering: A* 529 (2011) 62-73.
- [18] D. Tabor, *The hardness of metals*, Oxford university press 2000.
- [19] P. Djemia, F. Ganot, P. Moch, V. Branger, P. Goudeau, Brillouin scattering investigation of elastic properties of Cu–Mo solid solution thin films, *Journal of Applied Physics* 90(2) (2001) 756-762.
- [20] M. Apreutesei, P. Steyer, L. Joly-Pottuz, A. Billard, J. Qiao, S. Cardinal, F. Sanchette, J.M. Pelletier, C. Esnouf, Microstructural, thermal and mechanical behavior of co-sputtered binary Zr–Cu thin film metallic glasses, *Thin Solid Films* 561 (2014) 53-59.
- [21] P. Coddet, F. Sanchette, J.C. Rousset, O. Rapaud, C. Coddet, On the elastic modulus and hardness of co-sputtered Zr–Cu–(N) thin metal glass films, *Surface and Coatings Technology* 206(17) (2012) 3567-3571.
- [22] H. Okamoto, Zn-Zr (zinc-zirconium), *Journal of Phase Equilibria and Diffusion* 28 (2007) 236-237.
- [23] P. Jiang, C. Blawert, M.L. Zheludkevich, The corrosion performance and mechanical properties of Mg-Zn based alloys—a review, *Corrosion and Materials Degradation* 1(1) (2020) 7.

- [24] J.M. Lopez, J.A. Alonso, L.J. Gallego, Determination of the glass-forming concentration range in binary alloys from a semiempirical theory: Application to Zr-based alloys, *Phys Rev B Condens Matter* 36(7) (1987) 3716-3722.
- [25] A. Guinier, *Théorie et technique de la radiocristallographie*, Dunod, 1964.
- [26] A.R. Yavari, A.L. Moulec, A. Inoue, N. Nishiyama, N. Lupu, E. Matsubara, W.J. Botta, G. Vaughan, M.D. Michiel, Å. Kvick, Excess free volume in metallic glasses measured by X-ray diffraction, *Acta Materialia* 53(6) (2005) 1611-1619.
- [27] E.-a. Zen, *Validity of "vegard's law"*, Mineralogical Society of America, 1956.
- [28] J. Bednarcik, S. Michalik, M. Sikorski, C. Curfs, X.D. Wang, J.Z. Jiang, H. Franz, Thermal expansion of a La-based bulk metallic glass: insight from high-energy x-ray diffraction, *Journal of Physics: Condensed Matter* 23(25) (2011).
- [29] K.-W. Park, J.-i. Jang, M. Wakeda, Y. Shibutani, J.-C. Lee, Atomic packing density and its influence on the properties of Cu-Zr amorphous alloys, *Scripta Materialia* 57(9) (2007) 805-808.
- [30] H.L. Peng, M.Z. Li, W.H. Wang, C.Z. Wang, K.M. Ho, Effect of local structures and atomic packing on glass forming ability in Cu_xZr_{100-x} metallic glasses, *Applied Physics Letters* 96(2) (2010).
- [31] G.A. Mansoori, N.F. Carnahan, K.E. Starling, T.W. Leland, Equilibrium Thermodynamic Properties of the Mixture of Hard Spheres, *The Journal of Chemical Physics* 54(4) (1971) 1523-1525.
- [32] J.L. Lebowitz, Exact Solution of Generalized Percus-Yevick Equation for a Mixture of Hard Spheres, *Physical Review* 133(4A) (1964) A895-A899.
- [33] P. Čapková, J. Šedivý, X - ray Debye characteristic temperatures of magnesium and α - titanium, *physica status solidi (a)* 42(2) (1977) 681-686.
- [34] U. Mizutani, Low Temperature Specific Heats of Pure Zinc, *Japanese Journal of Applied Physics* 10(3) (1971) 367.
- [35] S. Yamanaka, K. Yoshioka, M. Uno, M. Katsura, H. Anada, T. Matsuda, S. Kobayashi, Thermal and mechanical properties of zirconium hydride, *Journal of Alloys and Compounds* 293 (1999) 23-29.
- [36] H. Ledbetter, Elastic properties of zinc: A compilation and a review, *Journal of Physical and Chemical Reference Data* 6(4) (1977) 1181-1203.

- [37] M. Apreutesei, P. Djemia, L. Belliard, G. Abadias, C. Esnouf, A. Billard, P. Steyer, Structural-elastic relationships of Zr-TL (TL= Cu, Co, Ni) thin films metallic glasses, *Journal of Alloys and Compounds* 707 (2017) 126-131.
- [38] G. Guo, Quasi-icosahedral clusters in Zr-based metallic glasses, *Metals* 10(9) (2020) 1135.
- [39] C.H. Li, R. Dedoncker, L.W. Li, F. Sedghgooya, F. Zighem, V. Ji, D. Depla, P. Djemia, D. Faurie, Mechanical properties of CoCrCuFeNi multi-principal element alloy thin films on Kapton substrates, *Surface and Coatings Technology* 402 (2020) 126474.
- [40] S. Frank, U.A. Handge, S. Olliges, R. Spolenak, The relationship between thin film fragmentation and buckle formation: Synchrotron-based in situ studies and two-dimensional stress analysis, *Acta Materialia* 57(5) (2009) 1442-1453.
- [41] B. Braeckman, Sputter deposition of complex alloy thin films, Ghent University, 2016.
- [42] T. Egami, Y. Waseda, Atomic size effect on the formability of metallic glasses, *Journal of non-crystalline solids* 64(1-2) (1984) 113-134.
- [43] J. Houska, P. Machanova, M. Zitek, P. Zeman, Molecular dynamics and experimental study of the growth, structure and properties of Zr-Cu films, *Journal of Alloys and Compounds* 828 (2020).
- [44] Z.D. Sha, Y.P. Feng, Y. Li, Statistical composition-structure-property correlation and glass-forming ability based on the full icosahedra in Cu-Zr metallic glasses, *Applied Physics Letters* 96(6) (2010).
- [45] T.-Y. Chang, Z. Wang, D. Xu, Icosahedral clusters in $\text{Cu}_{100-x}\text{Zr}_x$ ($x=32,34,36,38.2,40$ at.%) metallic glasses near the peak of glass-forming ability ($x=36$): A balance between population and encaging strength, *Journal of Physics and Chemistry of Solids* 154 (2021).
- [46] B. Arman, S.-N. Luo, T.C. Germann, T. Çağın, Dynamic response of $\text{Cu}_{46}\text{Zr}_{54}$ metallic glass to high-strain-rate shock loading: Plasticity, spall, and atomic-level structures, *Physical Review B* 81(14) (2010).
- [47] K.-W. Park, Effect of the Atomic Packing Density on the Structural Change Rate of Amorphous Alloys under Elastostatic Stress, *Metals and Materials International* 14(2) (2008) 159-163.
- [48] M.H. Abbasi, S.G. Shabestari, R. Tavakoli, On the glass-forming ability of $(\text{Zr}_{0.5}\text{Cu}_{0.5})_{100-x}\text{Al}_x$ ternary alloys: A molecular dynamics study, *Materials Today Communications* 31 (2022).

- [49] Y. Prabhu, S. Vincent, A. Nair, W. Kim, E.S. Park, J. Bhatt, Composition Design and Nanoindentation Studies on Mg-Ca-Zn Metallic Glass, *Metallurgical and Materials Transactions A* 53(4) (2022) 1419-1429.
- [50] M. Apreutesei, P. Steyer, A. Billard, L. Joly-Pottuz, C. Esnouf, Zr-Cu thin film metallic glasses: An assessment of the thermal stability and phases' transformation mechanisms, *Journal of Alloys and Compounds* 619 (2015) 284-292.
- [51] N. Mattern, A. Schöps, U. Kühn, J. Acker, O. Khvostikova, J. Eckert, Structural behavior of Cu_xZr_{100-x} metallic glass ($x=35-70$), *Journal of Non-Crystalline Solids* 354(10-11) (2008) 1054-1060.
- [52] A. Brognara, J.P. Best, P. Djemia, D. Faurie, G. Dehm, M. Ghidelli, Effect of composition and nanostructure on the mechanical properties and thermal stability of $Zr_{100-x}Cu_x$ thin film metallic glasses, *Materials & design* 219 (2022) 110752.
- [53] C. Pallier, P. Djemia, D. Fournier, L. Belliard, J. Lu, F. Eriksson, P. Eklund, G. Greczynski, A. Le Febvrier, Thermal, electrical, and mechanical properties of hard nitrogen-alloyed Cr thin films deposited by magnetron sputtering, *Surface and Coatings Technology* 441 (2022) 128575.
- [54] M. Hardiman, T.J. Vaughan, C.T. McCarthy, The effects of pile-up, viscoelasticity and hydrostatic stress on polymer matrix nanoindentation, *Polymer Testing* 52 (2016) 157-166.
- [55] K.P. Marimuthu, K. Lee, J. Han, F. Rickhey, H. Lee, Nanoindentation of zirconium based bulk metallic glass and its nanomechanical properties, *Journal of Materials Research and Technology* 9(1) (2020) 104-114.
- [56] J.C. Ye, J.P. Chu, Y.C. Chen, Q. Wang, Y. Yang, Hardness, yield strength, and plastic flow in thin film metallic-glass, *Journal of Applied Physics* 112(5) (2012) 053516.
- [57] M. Bai, K. Kato, N. Umehara, Y. Miyake, Nanoindentation and FEM study of the effect of internal stress on micro/nano mechanical property of thin CN_x films, *Thin Solid Films* 377 (2000) 138-147.
- [58] G.M. Pharr, W.C. Oliver, Measurement of Thin Film Mechanical Properties Using Nanoindentation, *MRS Bulletin* 17(7) (2013) 28-33.
- [59] G. Abadias, C. Jaouen, F. Martin, J. Pacaud, P. Djemia, F. Ganot, Experimental evidence for the role of supersaturated interfacial alloys on the shear elastic softening of Ni/Mo superlattices, *Physical Review B* 65(21) (2002) 212105.
- [60] CH. Li, C. Poltronieri, G. Abadias, P. Djemia, Computational approach to identify structural and elastic relationship in metastable crystalline and amorphous alloy thin

films: Mo_{1-x}Ni_x and Mo_{1-x}Si_x case studies, Surface and Coating Technology, to be published (2023).

CHAPTER 4: FROM BINARY TO TERNARY ZNMgZR ALLOYS

Several studies investigated the feasibility to use ternary Zr-, Ti-, Fe- and Mg-based TFMGs as promising candidates for implant and surgical tools [1-3]. For example in a recent work, ternary ZrCu(Ca, Mg, Mo, Si, Sr) TFMGs were deposited on stainless steel and Ti-based alloys and the authors exploited these systems for developing novel coatings for permanent bioimplants [4]. Regarding TFMGs for biodegradable applications, there is an intense investigation on MgZnCa TFMGs [5-7] but other systems remain unexplored.

In this context, the investigation of ternary ZnMgZr with biomedical purposes has never been addressed in literature and this chapter discusses the synthesis, structure and mechanical properties of these novel ZnMgZr films. Under the light of the results of the previous chapter, the ternary system ZnMgZr was fabricated based on the thermodynamic evaluation of glass-forming ability and experimental result of binary alloys. Subsequently, the structural and mechanical properties of these films have been investigated by experiments and simulations. Finally, an assessment of biodegradation, corrosion behavior and cytotoxicity of these materials is presented.

4.1 Glass-forming ability and deposition

The glass-forming ability of ZnMgZr alloy was assessed using the analytical thermodynamic model described in the Section 2.1.1 in **Chapter2: Material and Methods**. **Fig. 1** represents the resulting difference between free energies of mixing of the amorphous and crystalline phases ($\Delta G_{am} - \Delta G_{cryst}$) calculated at 300 K. The glass-forming compositional borders are highlighted by the grid region identified for the compositions where $\Delta G_{am} - \Delta G_{cryst} < 0$. For ZnMg alloy, the Miedema model

predicted a glass-forming compositional range between 20 to 90 at.% Zn, while the glass-forming compositional range for ZnZr resulted 24 and 95 at.% Zn.

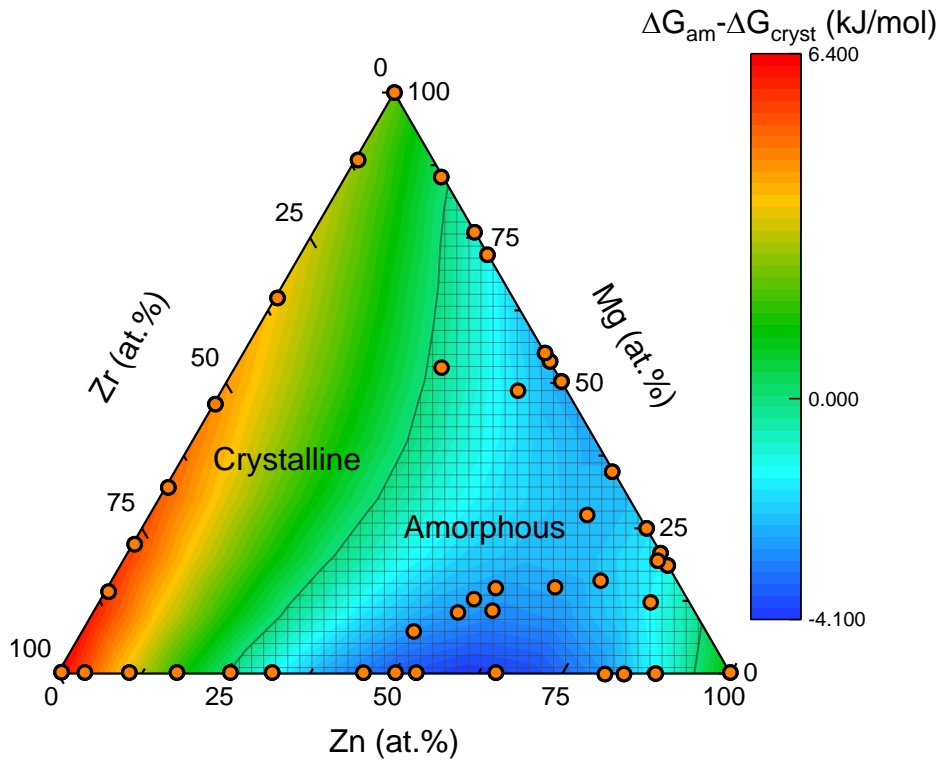


Fig. 4.1 Free energy of formation of amorphous and crystalline phases calculated at 300 K with the thermodynamical model [8] for ZnMgZr alloys. The grid region represents the compositional amorphization range and the dots are the investigated binary and ternary compositions.

On the basis of these results, we selected the deposition parameters (refer to **Table 2.2**) in order to deposit 12 alloys with thermodynamically-expected amorphous compositions.

The mass density and the related atomic volume, measured by weighting the substrates before and after the deposition process, are compared with those calculated by AIMD in **Fig. 4.2**. The grids in experimental results represent the expected range of amorphization, while all the compositions fabricated by AIMD methods are amorphous. The experimental and calculated results show an overall well-agreement.

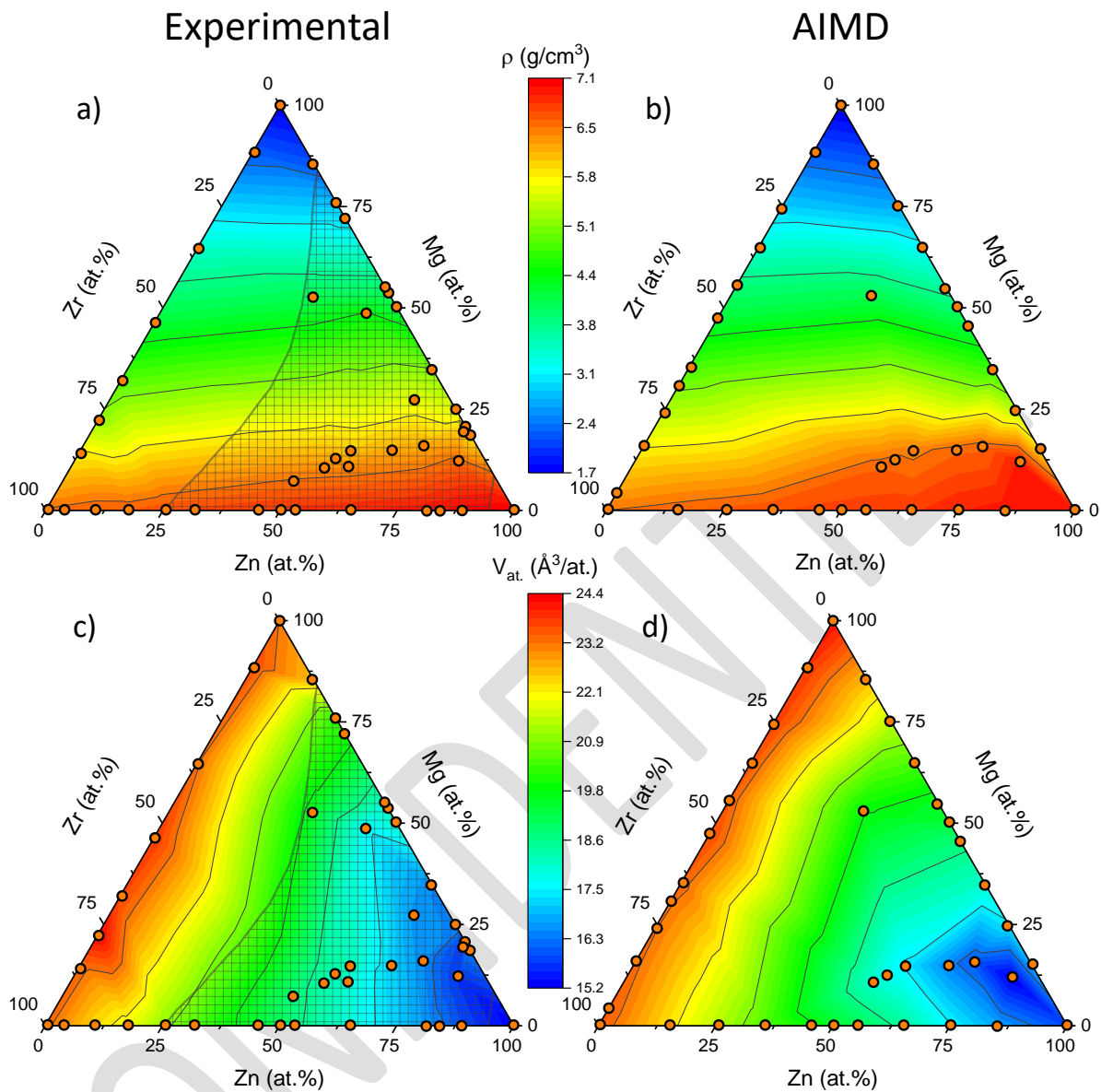


Fig. 4.2 Mass density ρ and atomic volume V_{at} . measured a-c) experimentally and b-d) by AIMD of ZnMgZr alloys. The orange dots represent the investigated compositions.

4.2 Amorphous structure

Based on the thermodynamic calculation of free-energy of formation of amorphous and crystalline phases, several ZnMgZr alloys were deposited with chemical composition falling in the amorphization range. The diffractograms of the deposited ZnMgZr TFMGs are illustrated in **Fig. 4.3**. The amorphous structure is confirmed by the presence of the principal diffraction peak (PDP) at 42-46°. Moreover, all the ternary

compositions were selected to promote the formation of an amorphous phase with good success. However, the skewness of the PDP (visible in $\text{Zn}_{79}\text{Mg}_{20}\text{Zr}_1$ and $\text{Zn}_{82}\text{Mg}_{12}\text{Zr}_6$) and the presence of a further broad peak at $53\text{-}54^\circ$ (in $\text{Zn}_{44}\text{Mg}_{49}\text{Zr}_7$, $\text{Zn}_{49}\text{Mg}_7\text{Zr}_{44}$, $\text{Zn}_{60}\text{Mg}_{10}\text{Zr}_{30}$ and $\text{Zn}_{65}\text{Mg}_{27}\text{Zr}_{32}$) suggest the presence of nanocrystallites in the amorphous matrix. Overall, the shift towards higher angles of the position of the PDP is visible when enriching the glassy material with Zn. The PDP was fitted with two Voigt functions in order to decouple the diffraction due to the first shell coordination atoms of amorphous material from the nanocrystalline contribution.

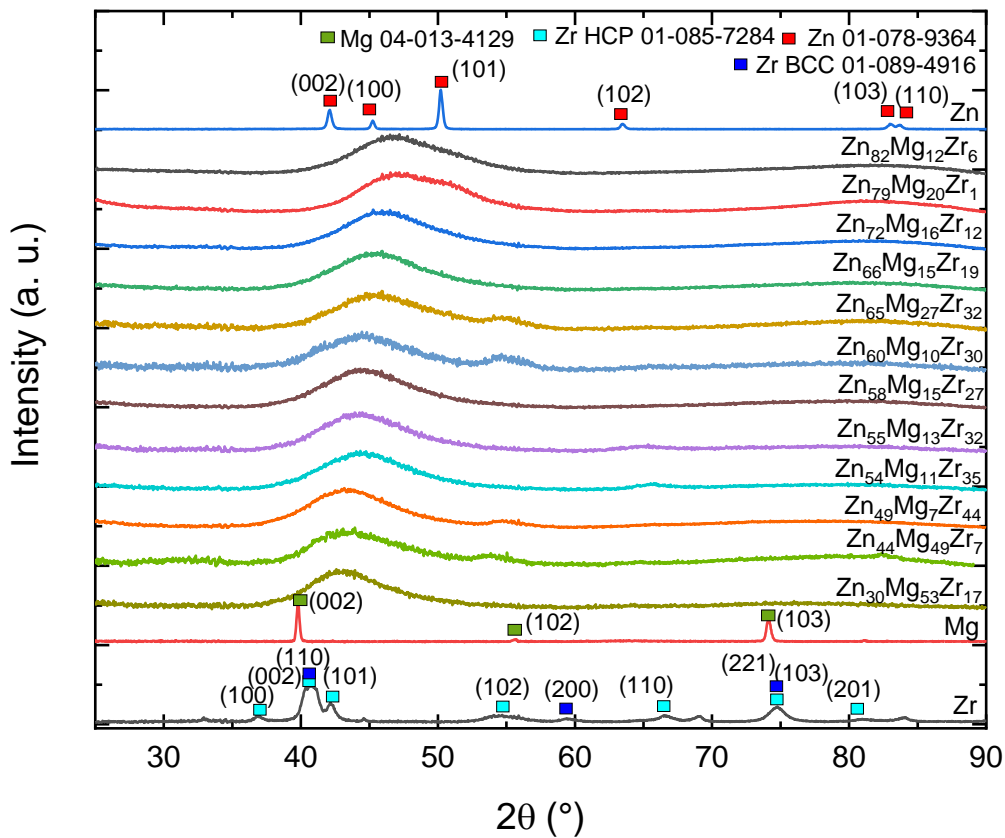


Fig. 4.3 XRD diffractograms of ZnMgZr films. The large hump present at $42\text{-}46^\circ$ is related to the amorphous phase.

The shift of the PDP is well known to be related to the shortening of average interatomic distances (d_{av}) through the Ehrenfest equation. The results of d_{av} of ZnMgZr TFMGs are illustrated and compared to those calculated by AIMD at 300K in **Fig. 3**. It was found that d_{av} was only Zn-dependent and specifically, when increasing the Zn content from 27 to 84 at.%, a shortening of d_{av} from 310 to 270 pm was

observed. The observed shortening in d_{av} is due to the formation of shorter Zn-Mg, Zn-Zr and Zn-Zn chemical bonds. Since the Zr and Mg have similar atomic radii, the average interatomic distances resulted nearly independent from their amount in the alloy and only Zn-dependent. A good correlation between measured and calculated values of d_{av} was observed in the amorphous compositional range. Moreover, a difference in d_{av} about ~ 10 pm is observed between crystalline and amorphous structures with the same compositions.

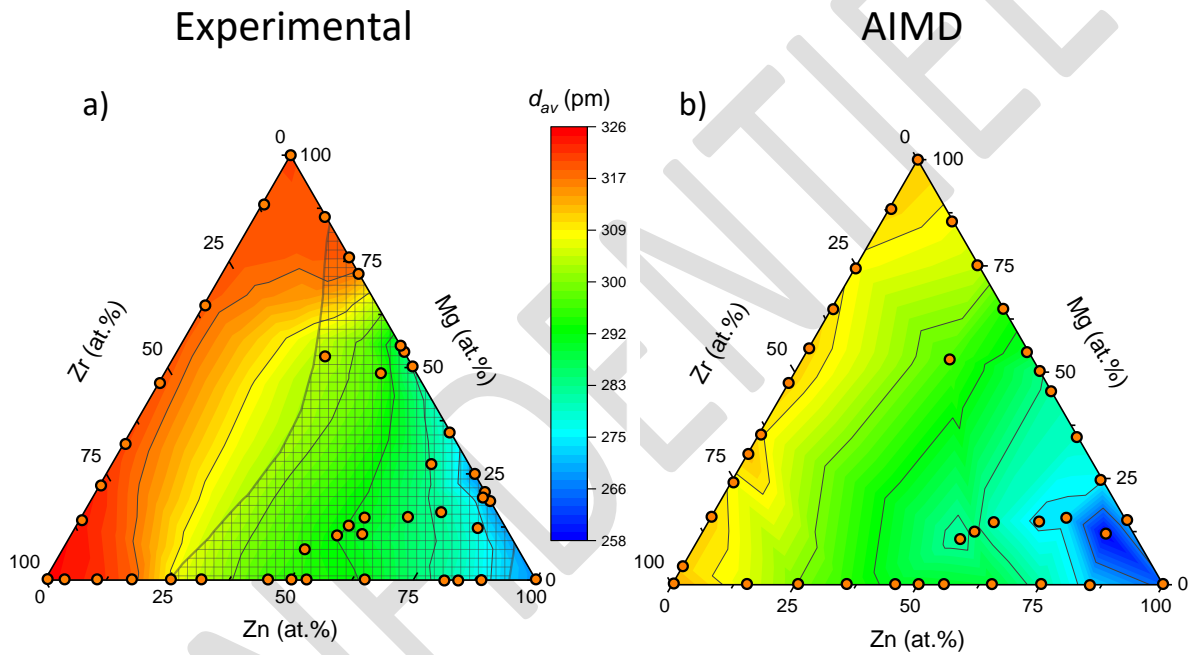


Fig. 4.4 Average interatomic distances a) measured with Erhenfest equation [9] for amorphous composition and with Bragg equation for crystalline composition and b) AIMD-calculated average interatomic distances of only amorphous ZnMgZr alloys.

4.3 Mechanical properties

The shortening of average interatomic distances of the amorphous materials is reflected on the increase in elastic moduli. The shear (G) and Young (E) moduli measured by BLS and compared with those calculated from AIMD-simulated structures are illustrated in **Fig. 4.5**, showing overall the same trends with values ranging from 20 and 45 GPa for crystalline Mg-rich films up to 36 and 100 GPa for crystalline Zr-rich films and ZnZr TFGMs, respectively.

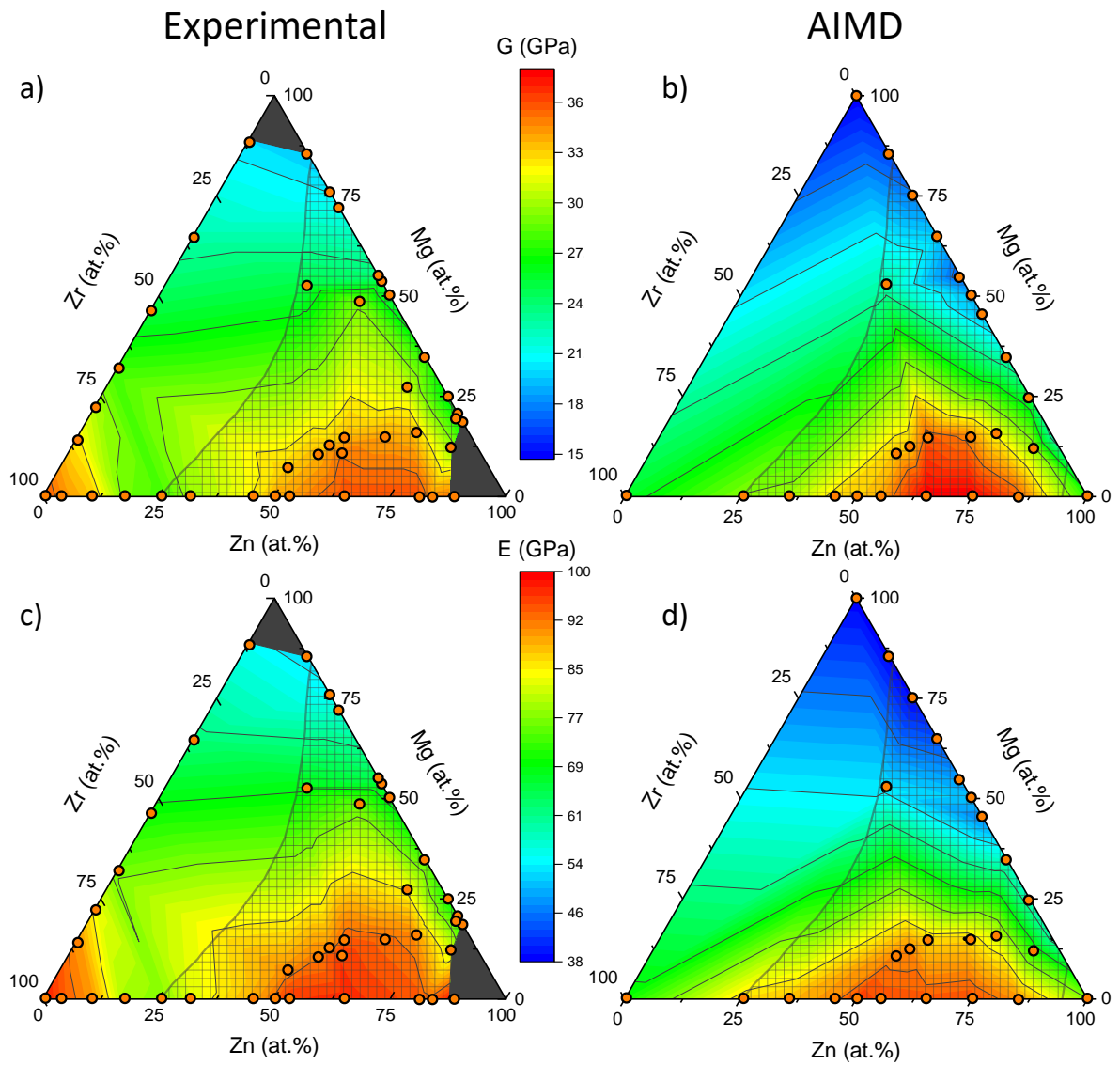


Fig. 4.5 Shear (G) and Young's (E) moduli a-c) measured using BLS and b-d) calculated from AIMD-simulated structures. To notice that the surface of pure Mg and pure Zn was too rough and did not give BLS signal.

Fig. 4.6 illustrates the nanoindentation hardness of ZnMgZr films with values ranging from 1 to 8 GPa. The hardness is related to yield strength of the material through the equation:

$$\sigma_y = \frac{H_v}{3} = \frac{H}{1.25 \cdot 3} \quad (35)$$

Where σ_y is the yield strength of the material, H_v is the Vickers hardness and H is the hardness measured by nanoindentation [10-12]. The resulted yield strength ranges from 0.3 GPa for Mg-rich films (in good agreement with bulk Mg) up to 2.1 GPa for pure Zr and ZnZr TFMGs. In amorphous alloys, the hardness of the material is related to the packing efficiency of the atoms and Mansori *et al.* [13] related the maximum of packing efficiency to the maximum in mismatch entropy (**Fig. 4.6b**) calculated as in Section 3.2.3 for ZnZr and ZnMg TFMGs. Overall, the trend of mismatch entropy reproduce satisfactorily the trend of yield strength (and hardness) of amorphous alloys.

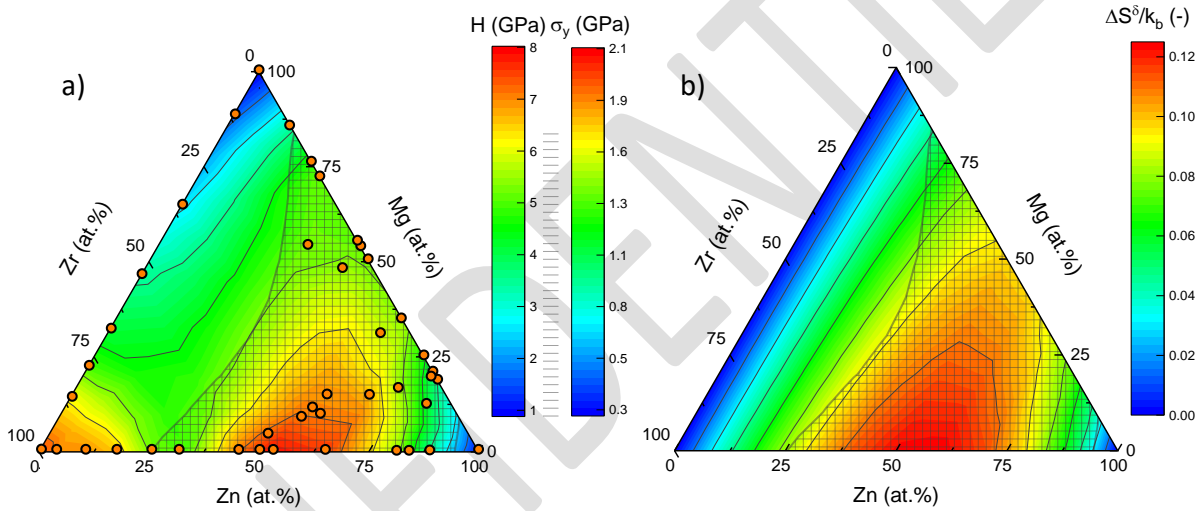


Fig. 4.6 a) Hardness (and related yield strength) and b) mismatch entropy for ZnMgZr alloys.

4.4 Tensile test on Kapton®

The values of crack initiation strain measured by tensile tests on Kapton® substrate are represented in **Fig. 4.7**. The ternary ZnMgZr films showed the lower value of crack initiation strain close to 0.4%, while the largest values were recorder for crystalline Zn_4Zr_{96} and amorphous $Zn_{50}Zr_{50}$ around 2.5%. However, these binary alloys were also thinner (about 450 nm) compared to ternary films (thicker than 800 nm) and this difference in crack initiation strain is mainly related to thickness differences as reported in Ref [14].

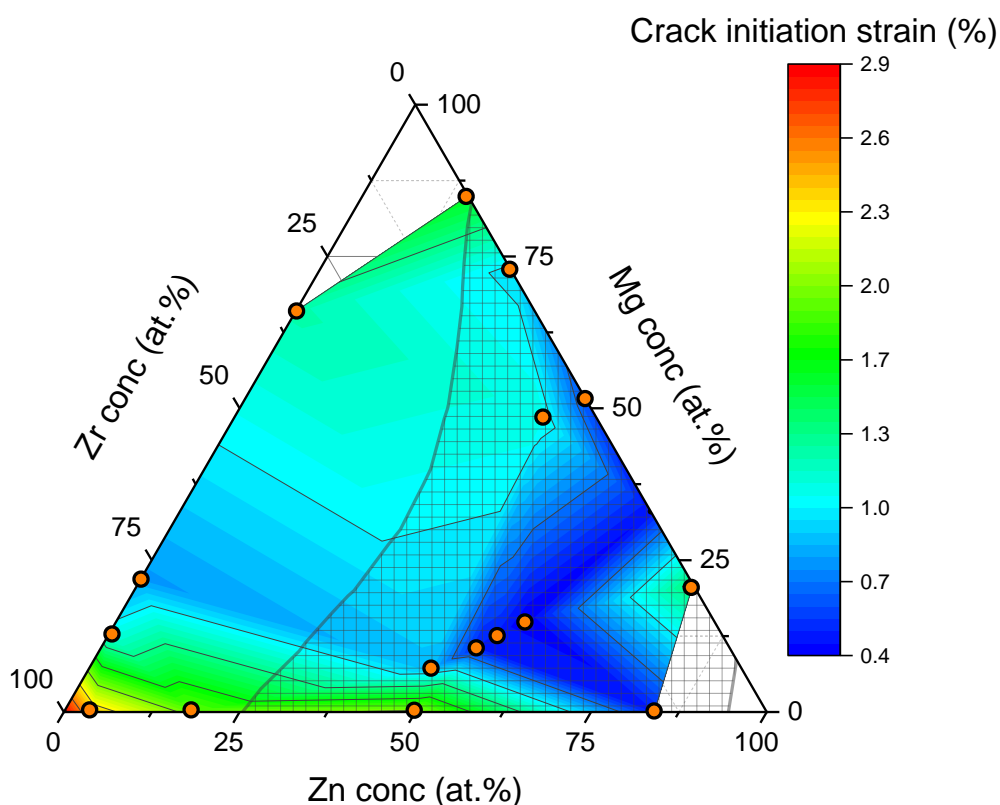


Fig. 4.7 Crack initiation strain of ZnMgZr thin films.

4.5 Biodegradability ternary ZnMgZr thin film alloys

Starting from the observations illustrated in Section 3.3.4 regarding the biodegradability behavior of ZnMg and ZnMg alloys, the synthesis of ternary ZnMgZr was aimed to develop novel coatings with tuned biodegradability rates. The results of the immersion test of ZnMgZr TFMGs that resisted 8 weeks in SBF are illustrated in **Fig. 4.8**. Top- and cross sectional- views show the structure of the as-deposited and 8-week-immersed films. The differences in thickness between the as-deposited and immersed films are probably due to error bar during the thickness measurements and it should not be taken as quantitative measurements.

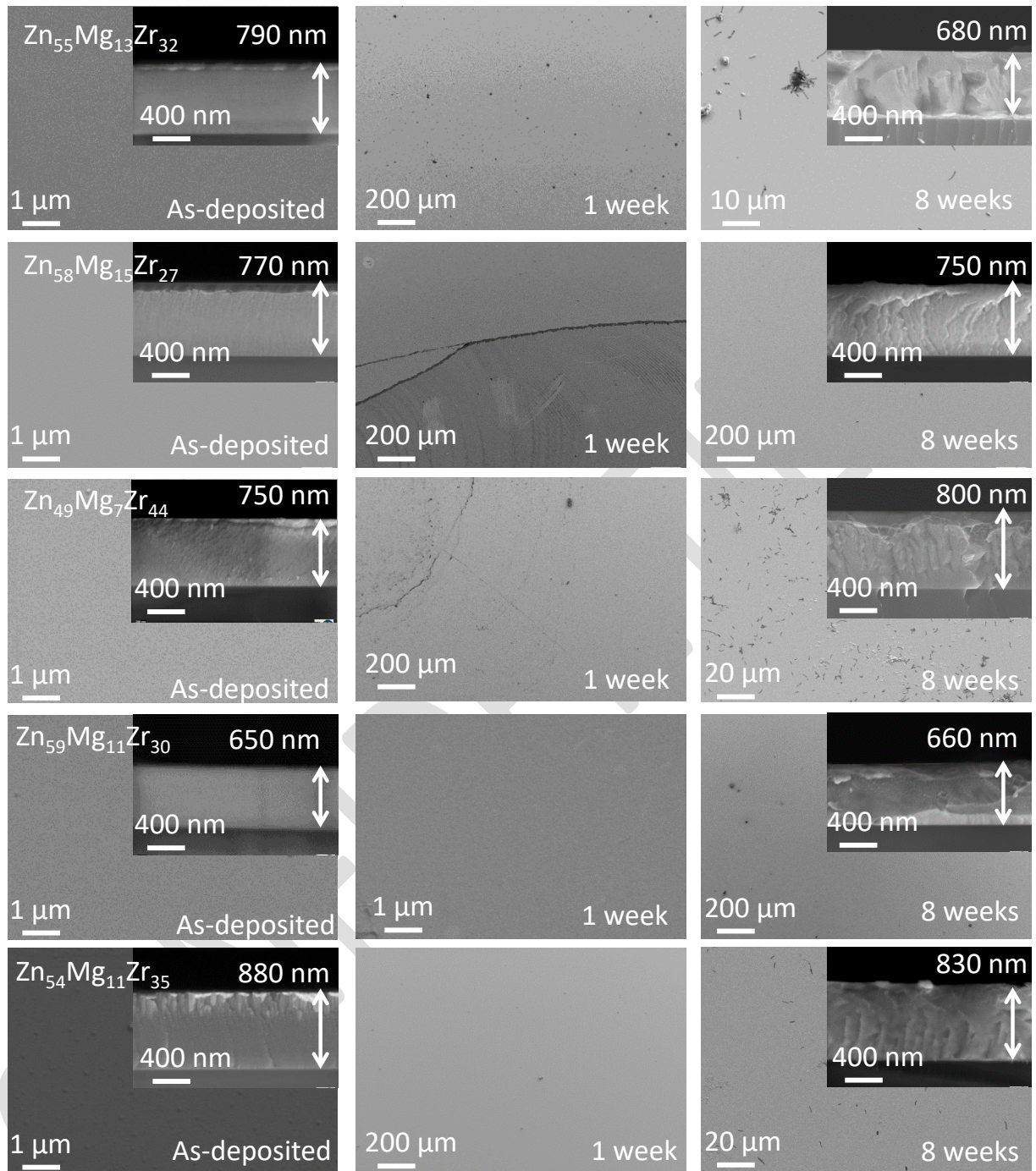


Fig. 4.8 Top-view of ZnMgZr films as-deposited, after 1 and 8 weeks of immersion in SBF at 37 °C. The inserts represent the cross-sectional view.

4.6 Corrosion investigation

In order to have a better estimation of the corrosion rate than the immersion tests, electrochemical investigation of corrosion rate and corrosion behavior was assessed in

Nov. 2023 by Mr. Vinicius De Oliveira Fidelis Sales in collaboration with a Laboratory for Biomaterials and Bioengineering in Quebec. The technique is described in the Refs. [15, 16]. The results of potentiodynamic polarization curves of one binary and three ternary alloys (repeated three times) are shown in **Fig. 4.9a**. Both the currents and potentials of corrosion resulted dependent on the chemical composition. In particular, the Zr-richest film resulted the most resistant to corrosion, while the corrosion potential becomes more negative with the addition of Mg in ternary ZnMgZr films and with the addition of Zn in binary ZnZr films. Similarly, the addition of Mg in ternary alloys and the addition of Zn in binary ZnZr films caused an increase in corrosion currents about one order of magnitude. For this reason, the Mg-richest ternary sample was delaminated after 1 week of immersion and was not shown in **Fig. 4.8**. In addition, the electrochemical measurements demonstrated all the films have a passive-corrosion behavior and binary $Zn_{84}Zr_{16}$ film shows the presence of a passivation potential at which the passive layer is not protective anymore at -600 mV Vs SCE. The passivation potential of ZnMg alloys in SBF has been also reported in literature for ZnMgCa TFMGs with at least 30 at.% of Zn [6, 17, 18]. **Fig. 4.9b** shows the results of electrochemical impedance spectroscopy of the same films. As for the potentiodynamic polarization, the most corrosion-resistant sample is the richest in Zr, indicated by the largest capacitive loop in the Nyquist plot, while the addition of Mg (and Zn) resulted in a decrease in the corrosion resistance of the material. The resulting corrosion rates are shown in **Table 4.1**.

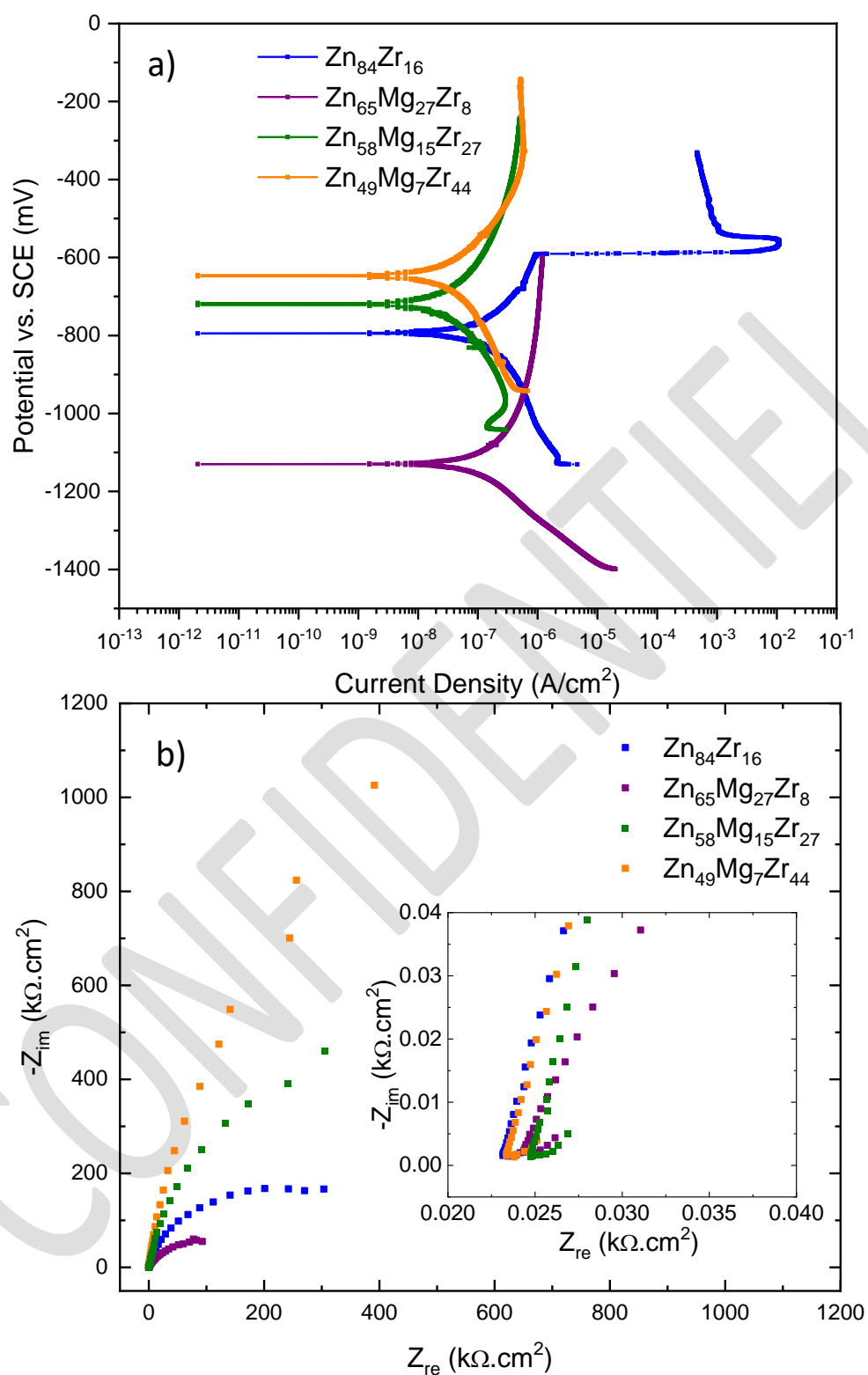


Fig. 4.9 a) Potentiodynamic polarization curves and b) electrochemical impedance data of binary ZnZr and ternary ZnMgZr TFMGs. The insert in b) shows the impedance values measured in the high-frequency range.

Table 4.1 Corrosion rates of binary and ternary investigated alloys.

| <i>Sample</i> | <i>Corrosion rate ($\mu\text{m}/\text{year}$)</i> |
|---|--|
| Zn ₈₄ Zr ₁₆ | 1.28 ± 0.3 |
| Zn ₆₅ Mg ₂₇ Zr ₈ | 1.87 ± 0.14 |
| Zn ₅₈ Mg ₁₅ Zr | 0.18 ± 0.08 |
| Zn ₄₉ Mg ₇ Zr ₄₄ | 0.19 ± 0.03 |

4.7 Cytotoxicity and viability study

The cytotoxicity of some of the ternary ZnMgZr and binary ZnZr that resisted to 8 weeks of immersion in SBF were assessed by LDH assay in collaboration with the laboratory of vascular transitional science (LVTS) by Dr. Teresa Yarza-Simon in Paris. The results demonstrated lack of toxicity of the materials after 48 h in contact with endothelial cells. **Fig. 4.10** illustrates the cell morphology and cell mortality after 48h in contact with the material in exam compared to the control group. In all the examined samples the cell mortality remained in below 10 %, confirming the non-cytotoxic behavior. In all cases the cells adhered on the substrates and presented the morphology typical of endothelial cells at the proliferative stage. The confocal image of the endothelial cells adhered on Zn₅₀Zr₅₀ (right) seemed to promote increased cell proliferation but analysis remained qualitative. In addition, the smaller cell mortality of Zn₈₄Zr₁₆ compared to Zn₅₀Zr₅₀ is coherent with the other studies present in literature [19]. Globally considered, these results match those observed with LDH viability assay, supporting the lack of toxicity of the materials and adhesive properties for endothelial cells.

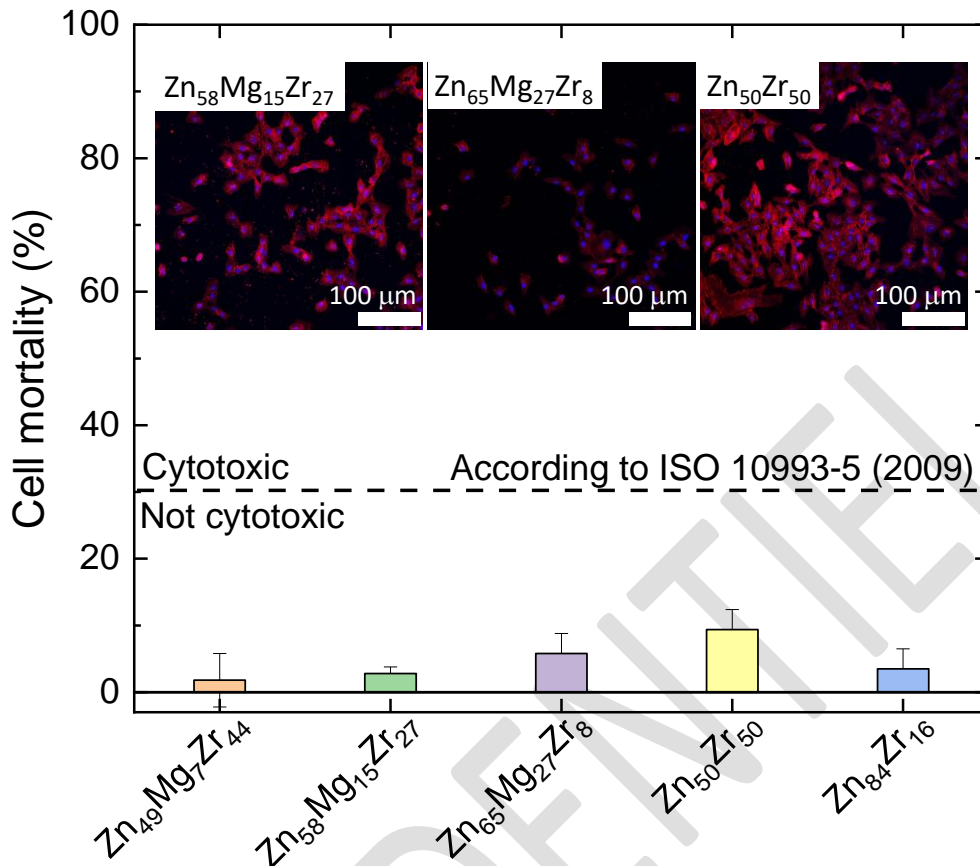


Fig. 4.10 Cell mortality of different ZnMgZr and ZnZr TFMGs. The dashed line at 30% represents the upper limit to define the material as not-cytotoxic according to ISO 10993-5 (2009). The inserts display the confocal images of the endothelial cells adhered on the materials after 48 h.

4.8 Conclusions

In this work, ZnMgZr thin film were synthesized by magnetron co-sputtering from Zn, Zr and Mg pure metallic targets and their structural, mechanical and biodegradation properties were investigated. It was found that:

- The films showed a broad diffraction peak at 42-46° typical of amorphous materials. However the skewness and the presence of other brad peaks for some compositions suggested the presence of nanocystallites.

- The shifting of the PDP was related to the formation of shorter Zn-Mg, Zn-Zr and Zn-Zn chemical bonds, decreasing the average interatomic distances from 310 for 30 at.% Zn down to 270 pm adding Zn up to 82 at.% Zn.
- The shortening of average interatomic distances were linked to the increase in elastic moduli G and E which increased from 27 and 75 GPa up to 35 and 95 GPa, respectively by adding Zn.
- The maximum in nanoindentation hardness (8 GPa) of the ZnMgZr films was recorded in the compositional region around the binary Zn₆₀Zr₄₀ TFMG and it has been related to the maximum in packing efficiency of the material and by consequence, to the maximum of mismatch entropy.
- The ZnMg films showed delamination after 1 week in SBF with macroscopic debris size, while ZnZr films did not show any delamination after 8 weeks of immersion. The addition of Mg to the ZnZr TFMGs demonstrated the ability to improve the corrosion currents (i.e. corrosion rates) in potentiodynamic polarization curves.
- Cytotoxicity tests were carried out on the samples that did not show any evident sign of delamination (ZnMgZr and ZnZr). All the investigated alloys resulted not toxic in accordance to ISO 10993-5 (2009).

In conclusion, in this work a wide range of composition of ZnMgZr films were synthesized, mainly in the amorphous zone, and structurally and mechanically investigated. In addition, the biodegradation behavior and cytotoxicity test proved the biocompatibility and the absence of macroscopic debris in ZnZr and ZnMgZr alloys. Overall, these findings pave the way to the design of compositional-tuned ZnMgZr films with tailored structural and mechanical properties to match the specific requirements for any targeted biomedical application.

4.9 References

- [1] S.T. Rajan, A. Arockiarajan, Thin film metallic glasses for bioimplants and surgical tools: A review, *Journal of Alloys and Compounds* 876 (2021) 159939.
- [2] P.-H. Tsai, C.-I. Lee, S.-M. Song, Y.-C. Liao, T.-H. Li, J.S.-C. Jang, J.P. Chu, Improved Mechanical Properties and Corrosion Resistance of Mg-Based Bulk Metallic Glass Composite by Coating with Zr-Based Metallic Glass Thin Film, *Coatings* 10(12) (2020) 1212.
- [3] B. Subramanian, S. Maruthamuthu, S.T. Rajan, Biocompatibility evaluation of sputtered zirconium-based thin film metallic glass-coated steels, *International Journal of Nanomedicine* 10(sup2) (2015) 17-29.
- [4] A.C. Parau, G.A. Juravlea, J. Raczowska, C. Vitelaru, M. Dinu, K. Awsyuk, D.M. Vranceanu, E. Ungureanu, C.M. Cotrut, A. Vladescu, Comparison of 316L and Ti6Al4V biomaterial coated by ZrCu-based thin films metallic glasses: Structure, morphology, wettability, protein adsorption, corrosion resistance, biomineralization, *Applied Surface Science* 612 (2023) 155800.
- [5] L. Zhang, L. Zhang, Z. Liang, J. Yang, Z. Qi, L. Xu, S. Li, Q. Zhai, Y. Gao, B. Zhao, Crystallization discrepancies in Mg₆₅Zn₃₀Ca₅ metallic glass ribbon and thin film revealed by nanocalorimetry, *Thermochimica Acta* 724 (2023) 179517.
- [6] T.O. Olugbade, T.E. Abioye, P.K. Farayibi, N.G. Olaiya, B.O. Omiyale, T.I. Ogedengbe, Electrochemical properties of MgZnCa-based thin film metallic glasses fabricated by magnetron sputtering deposition coated on a stainless steel substrate, *Analytical Letters* 54(10) (2020) 1588-1602.
- [7] C. Liu, Q. Wang, B. Han, J. Luan, J.-J. Kai, C.-T. Liu, G. Wu, J. Lu, Second phase effect on corrosion of nanostructured Mg-Zn-Ca dual-phase metallic glasses, *Journal of magnesium and alloys* 9(5) (2021) 1546-1555.
- [8] G. Van der Kolk, A. Miedema, A. Niessen, On the composition range of amorphous binary transition metal alloys, *Journal of the Less Common Metals* 145 (1988) 1-17.
- [9] A.R. Yavari, A. Le Moulec, A. Inoue, N. Nishiyama, N. Lupu, E. Matsubara, W.J. Botta, G. Vaughan, M. Di Michiel, Å. Kvick, Excess free volume in metallic glasses measured by X-ray diffraction, *Acta Materialia* 53(6) (2005) 1611-1619.
- [10] T. Sawa, Correlation between nanoindentation test result and vickers hardness, *Proceedings of the IMEKO*, 2010, pp. 171-174.
- [11] P. Zhang, S.X. Li, Z.F. Zhang, General relationship between strength and hardness, *Materials Science and Engineering: A* 529 (2011) 62-73.
- [12] D. Tabor, *The hardness of metals*, Oxford university press 2000.
- [13] G. Mansoori, N.F. Carnahan, K. Starling, T. Leland Jr, Equilibrium thermodynamic properties of the mixture of hard spheres, *The Journal of Chemical Physics* 54(4) (1971) 1523-1525.

- [14] C. Li, R. Dedoncker, L. Li, F. Sedghgooya, F. Zighem, V. Ji, D. Depla, P. Djemia, D. Faurie, Mechanical properties of CoCrCuFeNi multi-principal element alloy thin films on Kapton substrates, *Surface and Coatings Technology* 402 (2020) 126474.
- [15] S. Ravanbakhsh, C. Paternoster, P. Mengucci, P. Chevallier, S. Gambaro, T. Lescot, C. Paoletti, V. Sales, M. Cabibbo, M.-A. Fortin, The impact of structure and temperature on the mechanical properties and radiopacity of Ta-W coatings for tiny endovascular medical implants, *Materials Chemistry and Physics* 297 (2023) 127342.
- [16] S. Gambaro, M.L. Nascimento, M. Shekargoftar, S. Ravanbakhsh, V. Sales, C. Paternoster, M. Bartosch, F. Witte, D. Mantovani, Characterization of a magnesium fluoride conversion coating on Mg-2Y-1Mn-1Zn screws for biomedical applications, *Materials* 15(22) (2022) 8245.
- [17] R. Nowosielski, K. Cesarz-Andraczke, Impact of Zn and Ca on dissolution rate, mechanical properties and GFA of resorbable Mg-Zn-Ca metallic glasses, *Archives of Civil and Mechanical Engineering* 18 (2018) 1-11.
- [18] D. Miskovic, K. Pohl, N. Birbilis, K. Laws, M. Ferry, Examining the elemental contribution towards the biodegradation of Mg-Zn-Ca ternary metallic glasses, *Journal of Materials Chemistry B* 4(15) (2016) 2679-2690.
- [19] N. Annonay, F. Challali, M.-N. Labour, V. Bockelée, A. Garcia-Sanchez, F. Tetard, M.-P. Besland, P. Djemia, F. Chaubet, Thin films of binary amorphous Zn-Zr alloys developed by magnetron co-sputtering for the production of degradable coronary stents: A preliminary study, *Bioactive materials* 3(4) (2018) 385.

CONCLUSIONS AND PERSPECTIVES

In this thesis we explored the synthesis and characterization of structural, mechanical and biodegradation properties of novel Zn-based thin films as promising coating for biodegradable implants.

It was concluded that:

- Binary ZnMg, ZnZr and ZrMg and ternary ZnMgZr films were fabricated by magnetron co-sputtering across the entire chemical range and the crystalline/amorphous forming compositional range has been identified both theoretically and experimentally.
- The structure of the deposited films was investigated through thermodynamical prediction of crystalline and amorphous phase formation and compared to experimental findings by XRD diffractograms showing an overall good agreement with MgZr, ZnZr and ZnMgZr, while the thermodynamical model resulted inaccurate to describe the glass forming ability of ZnMg. The structure of the deposited binary and ternary system was also simulated using *ab initio* molecular dynamics and this allowed the comparison with some quantity, such as mass density and atomic volume, to analyze if the calculations well-reproduce the amorphous nature of the deposited films.
- The structural features obtained by both experiments and simulations were related to the mechanical properties of the material such as elasticity, hardness, yield strength and elastic limit through a delicate experimental and simulation campaign. The average interatomic distances of the alloys played a crucial role on the elastic behavior of amorphous materials. Moreover, the fraction of hetero- and homometallic bonds at the short range order is critically playing a role on both average interatomic distances and packing fraction

which is directly related to some physical properties as it was shown for the hardness of the films. Overall, the elastic properties of the films satisfy the mechanical (elastic) requirements listed in **Chapter 1: State-of-the-art**.

- Dedicated experiments were carried out to investigate the biodegradation and biocompatibility behavior of these materials, in order to explore their potential as coating able to enhance the properties of already-existing biodegradable implants. These experiments include the investigation of degradation behavior through starting immersion test and electrochemical experiments as well as cytotoxicity assessment. Immersion test of few ternary and binary ZnZr films didn't show delamination of the films even after 8 weeks of immersion with some non-quantitative variations in thickness. In order to better evaluate the corrosion rate of these material, potentiodynamic polarization curves and electrochemical impedance spectroscopy showed that the corrosion rate can be tuned tailoring the chemical composition. In addition, all the investigated alloys resulted biocompatible according to ISO 10993-5 (2009).
- Tensile tests on Kapton highlighted the main drawback of these films which lies in their limited plasticity (deformation < 1%) with brittle failure.

Overall, this thesis work acts as pioneer research of novel ZnMgZr films as promising biomaterial coating paving the way to the development of novel and compositional-tailored films to satisfy the requirements needed for challenging biomedical applications. The mechanical properties, corrosion rates and biocompatibility make these materials promising candidates for future applications, however, some challenges need to be faced, such as the limited plasticity of TFMGs.

This aspect is one of the greatest challenges of metallic glasses and it has been intensively investigated for various decades. During my PhD thesis, we explored several strategies to improve the plasticity of ZrCu-based TFMGs within the framework of international projects in collaboration with the Max Planck Institut für Eisenforschung (MPIE) in Düsseldorf. In particular, we investigated the effect of Al addition on the mechanical properties of ZrCu-based TFMGs. In this study the effect of

Al demonstrated a pivotal role on both elasticity and cracking behavior of ZrCu-based TFMGs (refer to **Annex**). For this reason, the investigation of the effect of Al on the plasticity of biocompatible TFMGs can be investigated as promising strategy to increase their plasticity.

Moreover, as well as for the composition, multilayered structure also showed to influence the mechanical properties of the films. **Fig. 5.1a** shows the micropillar compression of monolithic ZrCu and ZrCuAl TFMGs showing a brittle failure, while in case of multilayer stacking (displayed in **Fig. 5.1b** and **Fig. 5.1c**) with bilayer period larger than 50 nm, the stress-strain curves show an “apparent” plasticity due to the inhibited propagation of shear bands. This phenomenon is still under investigation and **Fig. 5.1d** shows the atom probe tomography of the first 275 nm on the top of a compressed pillar of multilayered ZrCu/ZrCuAl with bilayer period of 200 nm showing the chemistry of a shear band that cause diffusion of Al into ZrCu layer and giving important insights on how the mechanical deformation might influence the local chemistry and enhance the plasticity of these films through the development of nanoarchitectures.

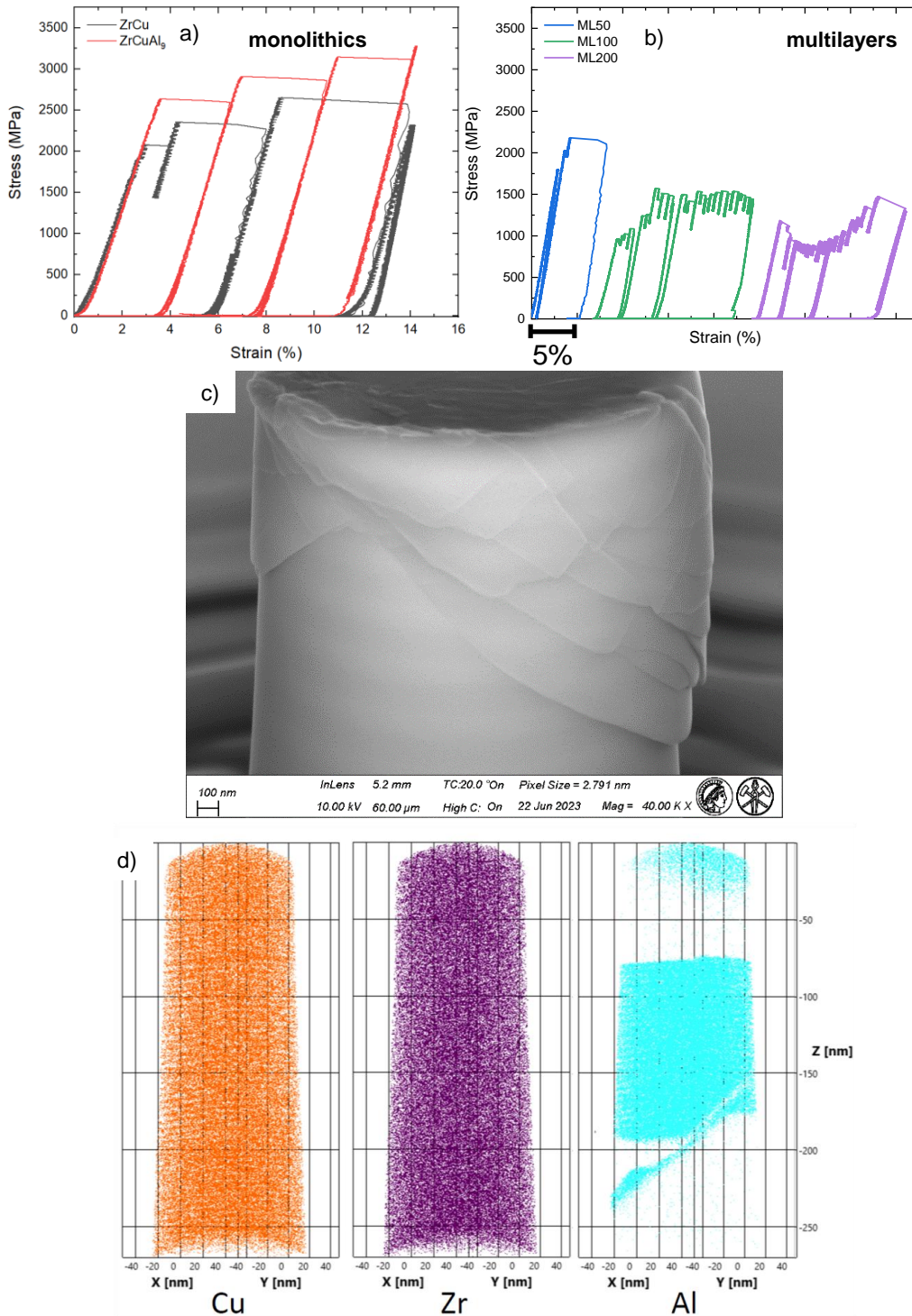


Fig. 5.1 Stress-strain curves of a) monolithic and b) multilayered ZrCu/ZrCuAl TFMGs. c) SEM-image and d) atom probe tomography of *post-mortem* multilayered pillar with bilayer period of 200 nm after compression.

Similar strategies were employed for ZnMgZr TFMGS in the framework of SALTO project, always in collaboration with MPIE, in which nanocomposite ZnMgZr films were fabricated and mechanically tested to investigate the effect of devitrification that might be caused intentionally or not and its effect on the structural-mechanical properties of these materials. Some preliminary results are illustrated in this section. **Fig. 5.2a** represents the XRD diagrams of as-deposited and annealed ZnMgZr TFMG. The shift of first and second diffraction hump is visible, presenting a modification of short and medium range order during annealing. Furthermore, the sample annealed for 5h also present a composite amorphous matrix with crystalline ZnZr phases which EBSD is represented in **Fig. 5.2b**.

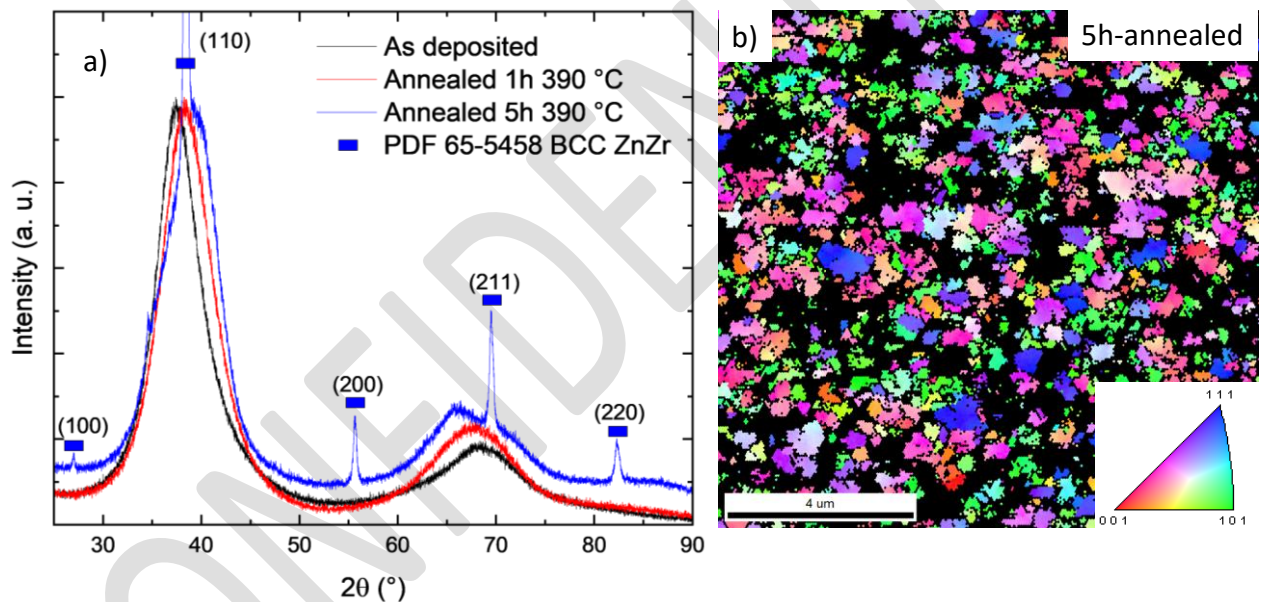


Fig. 5.2 a) XRD diffractograms of as-deposited and annealed ZnMgZr TFMGs. b) EBSD image of 5h annealed ZnMgZr TFMG, black areas represent amorphous regions.

The mechanical properties of the annealed sample was assessed by nanoindentation and the results are shown in **Fig. 5.3** showing the increase in Young modulus and hardness during annealing.

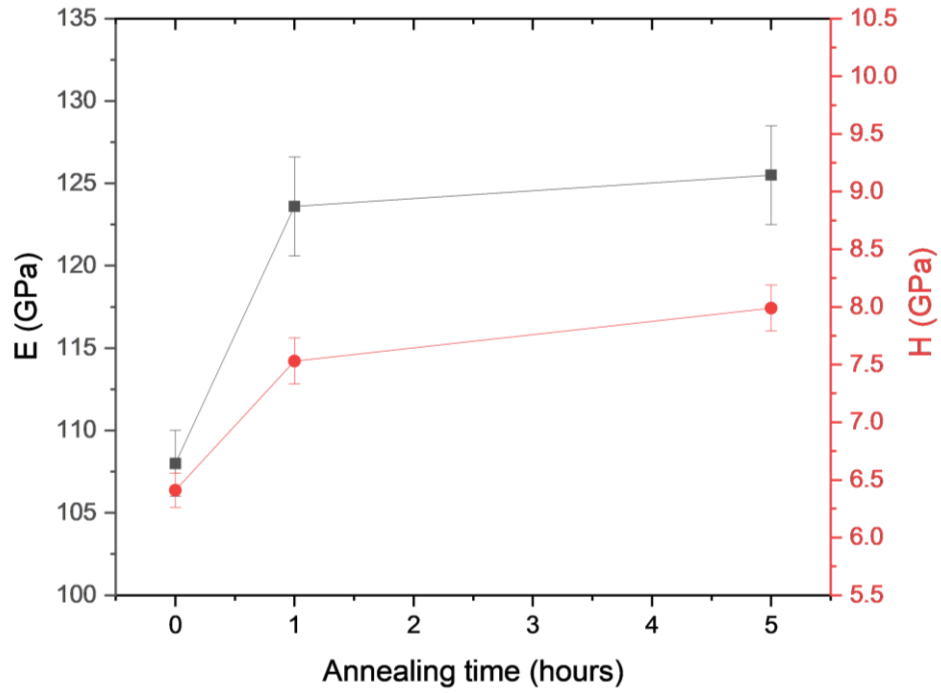


Fig. 5.3 Young's modulus and hardness measured by nanoindentation of as-deposited and annealed ZnMgZr films.

Furthermore, the SEM imaging of the nanoindenters is shown in **Fig. 5.4**. The devitrification phenomena caused a clear embrittlement visible from the cracks formed at the corner of the Berckovitch print and on the surface of the samples.

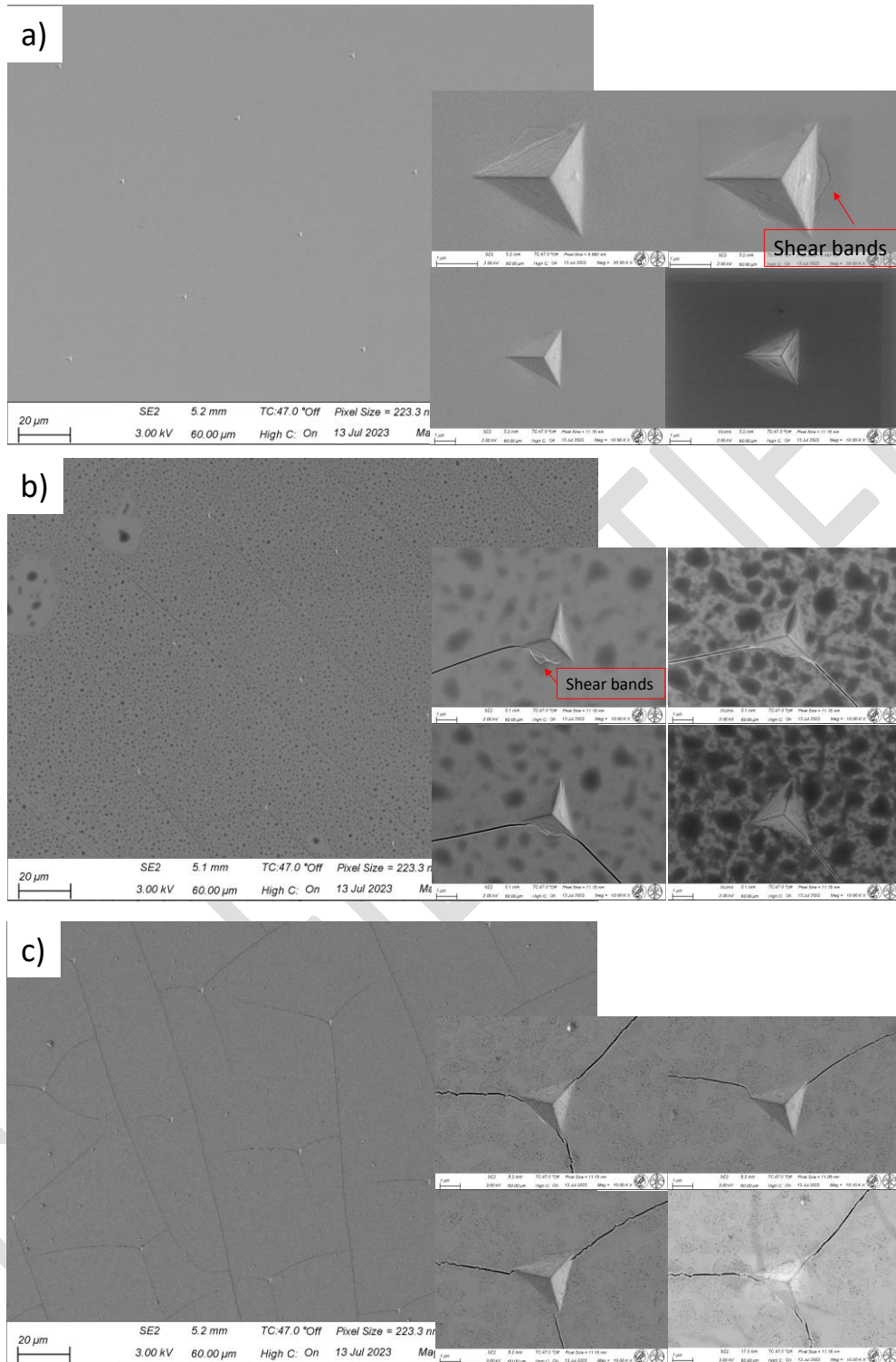


Fig. 5.4 SEM-images of nanoindentations of a) as-deposited and b-c) annealed ZnMgZr film after 1 and 5h, respectively.

Further investigations of these phenomena are in progress through synchrotron source XRD *in situ* heating (@ SOLEIL in Nov. 2023) and *ex situ* micropillar compression of as-

deposited and annealed samples have been carried out (preliminary results are illustrated in **Fig. 5.5**) and the results are under investigation.

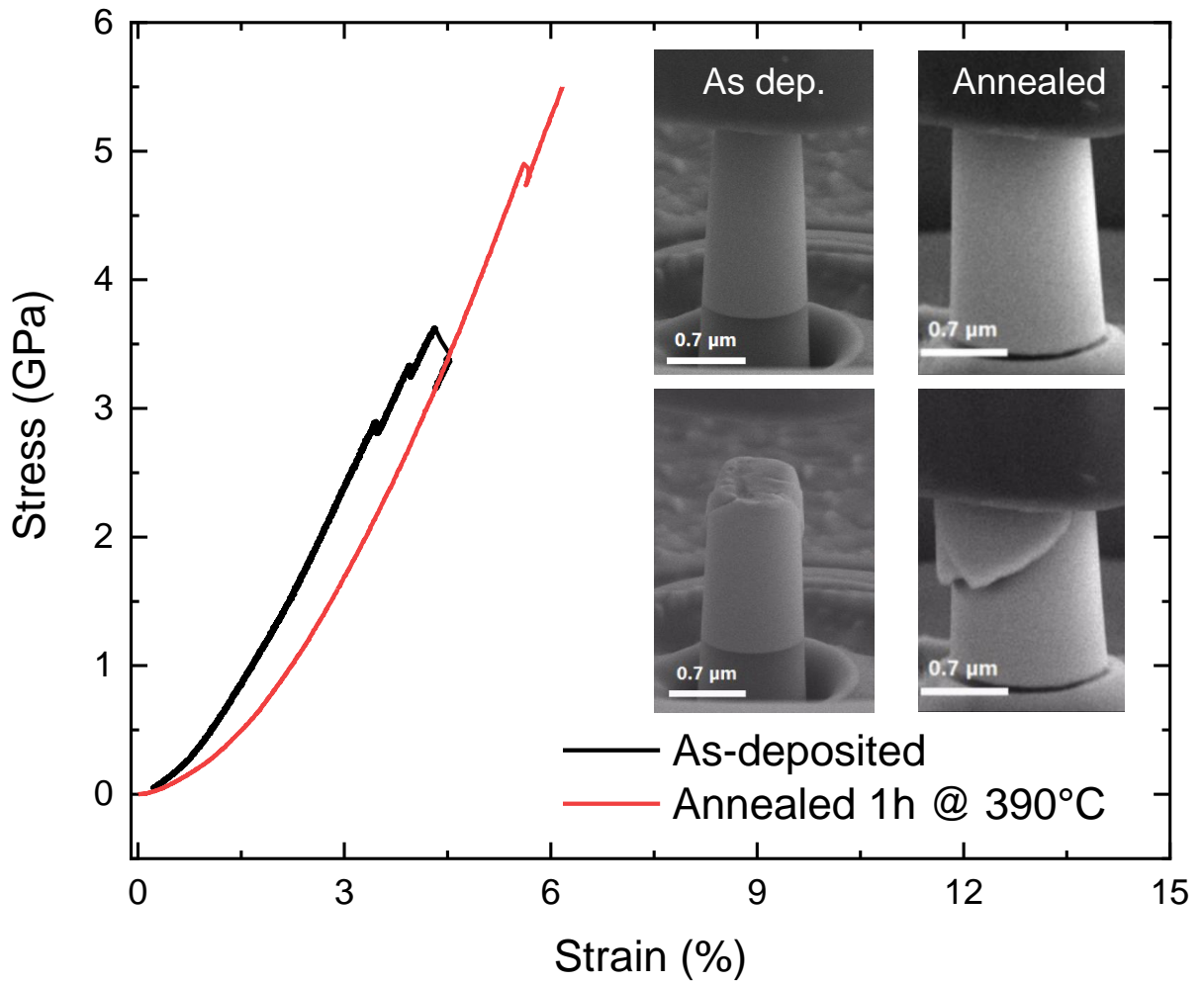


Fig. 5.5 Micropillar compression of as-deposited (black line) and 1h-annealed (red line) ZnMgZr TFMG. The inserts represent the micropillars before and after compression.

ANNEX

Refer to C. Poltronieri, A. Brognara, F. Bignoli, S. Evertz, P. Djemia, D. Faurie, F. Challali, C. Li, L. Belliard, G. Dehm, Mechanical properties and thermal stability of ZrCuAl_x thin film metallic glasses: Experiments and first-principle calculations, Acta Materialia 258 (2023) 119226.

CONFIDENTIEL

Abstract

Traditional biomaterials are designed to provide permanent support for damaged bodily apparatus, becoming indispensable devices in modern society, serving various critical applications. However, while permanent devices have undoubtedly revolutionized the field of medical device technology, they are susceptible to wear, corrosion, and mechanical failures, which may lead to invasive revision surgeries. For these reasons, the development of biodegradable materials that possess the balance between structural integrity, subjected to a homogenous degradation and the predictable degradation kinetics presents a multifaceted challenge and requires rigorous scientific investigations. In this context, this PhD thesis aims to shed light on the potential of Zn-based thin films as materials for biodegradable implants. The films were synthesized by RF-magnetron co-sputtering and then, a delicate campaign of experiments and calculations was carried out to investigate the properties of the films. Among the involved characterization techniques, X-ray diffraction (XRD) and scanning electron microscopy (SEM) were used to investigate the structure of the deposited films. The mechanical properties of the materials were investigated through Brillouin light scattering, nanoindentation and tensile tests on Kapton®. In addition molecular dynamic calculations were used to simulate the structure of the materials and to investigate the elastic properties of the materials. The film biocompatibility was assessed by cytotoxicity test and its behavior in physiological environment was investigated by electrochemical and static immersion tests in simulated body fluid solution

L'étude des films de métaux amorphes reçoit de plus en plus d'attention en raison des excellentes propriétés mécaniques : une limite à rupture proche de la théorie, une dureté et une déformation élastique élevées. Leur structure atomique désordonnée est à l'origine de propriétés physiques uniques et différentes de leurs homologues cristallins. Ces propriétés font de ces alliages métalliques amorphes des matériaux prometteurs pour des applications de revêtement résistant à l'usure, à la corrosion et des matériaux biorésorbables, mécaniquement satisfaisant et biocompatibles. Dans cette thèse, nous avons étudiés les propriétés de films minces d'alliages binaires et ternaires à base de Zinc dans une large gamme de composition. Tous les films ont été déposés par pulvérisation magnétron à partir de cibles pures sur deux types de substrats dur (silicium) et flexible (Kapton®). Les analyses physico-chimiques (EDX, MEB et DRX) ont permis de mettre en évidence une large gamme de structures amorphes pour les différents systèmes. Les propriétés mécaniques des films ont ensuite été étudiées, en combinant plusieurs techniques expérimentales : diffusion Brillouin de la lumière, la nanoindentation et les essais de micro-traction de films sur substrats de Kapton®. Des calculs de dynamique moléculaire ont été utilisés pour simuler la structure des matériaux et étudier leurs propriétés élastiques. La dégradation des films déposés a été étudiée sur des échantillons immergés dans du SBF à 37°C pendant plusieurs semaines (de 1 à 8). La cytotoxicité et la corrosion in vitro des couches minces ont été également évaluées sur les compositions prometteuses.